Title

Computational Methods Based on the Linearized Landau-Lifshitz-Gilbert Equation for Linear and Non-linear Micromagnetic Modeling

Permalink

Author

Lin, Zhuonan

Publication Date

2022

Peer reviewed|Thesis/dissertation

UNIVERSITY OF CALIFORNIA SAN DIEGO

Computational Methods Based on the Linearized Landau-Lifshitz-Gilbert Equation for Linear and Non-linear Micromagnetic Modeling

A Dissertation submitted in partial satisfaction of the requirements
for the degree Doctor of Philosophy

in

Materials Science and Engineering

by

Zhuonan Lin

Committee in charge:

      Professor Vitaliy Lomakin, Chair
      Professor Yeshaiahu Fainman
      Professor Zhaowei Liu
      Professor Yu Qiao
      Professor Kesong Yang

2022

The Dissertation of Zhuonan Lin is approved, and it is acceptable in quality and form for publication on microfilm and electronically.

University of California San Diego

2022

DEDICATION

To my family.

TABLE OF CONTENTS

LIST OF FIGURES

LIST OF TABLES

ACKNOWLEDGEMENTS

I would like to acknowledge my advisor, Professor Vitaliy Lomakin, for his guidance and advice during my years at UCSD. This work would not have been possible without his mentorship and help. His deep knowledge and great support are the key to my success during my doctoral studies. I would like to thank my labmates from Professor Lomakin's group. I would like to thank Dr. Marko Lubarda who introduced me to the micromagnetic field. I would like to thank Dr. Iana Volvach for the help on MRAM modeling and the collaboration with me. I would like to thank Xueyang Wang for the help on the development of the FastMag solver. I would also like to thank Dr. Majd Kuteifan, Dr. Marco Menarini, Fangzhou Ai and Jiawei Duan for their daily help during my doctoral studies. I thank all the members of my thesis committee for reading this dissertation and providing valuable feedback.

Chapter 3, in full, is a reprint of the material as it appears in Z. Lin, I. Volvach, X. Wang and V. Lomakin, "Eigenvalue-based micromagnetic analysis of switching in spin-torque-driven structures", Phys. Rev. Appl., **17**, 034016 (2022). The dissertation author was the primary investigator and author of this paper.

Chapter 4, in full, is a reprint of the material as it appears in Z. Lin, I. Volvach and V. Lomakin, "Switching Current Reduction in Magnetic Random Access Memories", which is currently in submission. The dissertation author was the primary researcher and author of this paper.

Chapter 5, in full, is currently being prepared for submission for publication of the material, Z. Lin, I. Volvach and V. Lomakin, "Fokker-Planck approach based on normal modes for computing write error rates in magnetic random access memories". The dissertation author was the primary researcher and author of this material.

Chapter 6, in full, is a reprint of the material as it appears in Zhuonan Lin, and Vitaliy Lomakin, "Linearized frequency domain Landau-Lifshitz-Gilbert equation formulation", which is accepted for publication by AIP Advances. The dissertation author was the primary researcher and author of this material.

Chapter 7, in full, is currently being prepared for submission for publication of the material Z. Lin, and V. Lomakin, "Harmonic balance solver for the Landau-Lifshitz-Gilbert equation". The dissertation author was the primary author of this chapter.

Finally, I would like to thank my family for their love and support.

VITA

2015   Bachelor of Science in Physics, University of Science and Technology of China

2017   Master of Science in Materials Science and Engineering, University of California San Diego

2022   Doctor of Philosophy in Materials Science and Engineering, University of California San Diego

PUBLICATIONS

Z. Lin and V. Lomakin, "Harmonic balance solver for the Landau-Lifshitz-Gilbert equation", in preparation.

Z. Lin, I. Volvach and V. Lomakin, "Fokker-Planck approach based on normal modes for computing write error rates in magnetic random access memories", in preparation.

Z. Lin and V. Lomakin, "Linearized frequency domain Landau-Lifshitz-Gilbert equation formulation", *AIP Advances,* forthcoming.

Z. Lin, I. Volvach and V. Lomakin, "Switching Current Reduction in Magnetic Random Access Memories", in submission.

Z. Lin, I. Volvach, X. Wang and V. Lomakin, "Eigenvalue-based micromagnetic analysis of switching in spin-torque-driven structures", *Phys. Rev. Appl.,* **17**, 034016 (2022)

I. Volvach, Z. Lin and V. Lomakin, "Perpendicular magnetic tunnel junction with edge and surface roughness," *J. Magn. Magn. Mater.*, forthcoming.

CONFERENCE PRESENTATIONS

Z. Lin, I. Volvach and V. Lomakin, "Switching optimization in magnetoresistive random access memories", *67th Annual Conference on Magnetism and Magnetic Materials*, Minneapolis, MN, USA, Oct. 31 – Nov. 4, 2022.

Z. Lin and V. Lomakin, "Finite Element Solver for Harmonic Linearized Landau-Lifshitz-Gilbert Equation", *67th Annual Conference on Magnetism and Magnetic Materials*, Minneapolis, MN, USA, Oct. 31 – Nov. 4, 2022.

Z. Lin and V. Lomakin, "Fokker-Planck equation based on normal modes for computing write error rates in magnetic random access memories", *15th Joint Magnetism and Magnetic Materials Intermag Conference*, New Orleans, LA, USA, Jan. 10 – Jan. 14, 2022.

Z. Lin, I. Volvach and V. Lomakin, "An eigenvalue-based framework for the magnetization switching by spin torque", *65th Annual Conference on Magnetism and Magnetic Materials*, Virtual Conference, Nov. 2 – Nov. 6, 2020.

Z. Lin, I. Volvach and V. Lomakin, "Computing resonant modes and excitation states in micromagnetic systems with finite element based solvers", *64th Annual Conference on Magnetism and Magnetic Materials*, Las Vegas, NV, USA, Nov. 4 – Nov. 8, 2019.

Z. Lin, X. Wang and V. Lomakin, "Computing resonant modes and excitation states in micromagnetic systems with a finite-element based frequency domain solver", *14th Joint Magnetism and Magnetic Materials Intermag Conference*, Washington, D. C., USA, Jan. 14 – Jan. 18, 2019.

ABSTRACT OF THE DISSERTATION

Computational Methods Based on the Linearized Landau-Lifshitz-Gilbert Equation for
Linear and Non-linear Micromagnetic Modeling

by

Zhuonan Lin

Doctor of Philosophy in Materials Science and Engineering

University of California San Diego, 2022

Professor Vitaliy Lomakin, Chair

Nanoscale magnetic materials and devices are at the heart of memory and recording
technologies ranging from magnetic hard drives to spintronic devices, such as magnetic random
access memory (MRAM) and spin transfer torque oscillators. Advanced development of these
technologies requires comprehensive computational tools. This dissertation presents a
theoretical and micromagnetic study of challenges faced when considering interactions between

applied fields and spin-polarized currents with nanomagnetic materials. The study is about solving the generally non-linear Landau-Lifshitz-Gilbert (LLG) equation using its linearized version. The approaches include using a linearized eigenvalue framework, solving a source-excited linearized LLG equation, and using a harmonic balance approach for the study of the higher-harmonic generation in weakly-nonlinear magnetization dynamics problems. The dissertation starts with an introduction to micromagnetics and modeling of spin-torque-driven devices. The following chapters present the eigenvalue based micromagnetic framework for spin-torque-driven devices. It presents an analysis related to the MRAM switching properties, including the critical current, switching time, and magnetization time evolution. It also introduces an optimization approach based on the eigenvalue analysis to reduce the critical current in MRAM. It then extends the eigenvalue analysis to the Fokker-Planck equation framework to study of non-switching probability, namely write error rate, under finite temperature. Next, the dissertation presents a solver for the linearized LLG equation with under time-harmonic applied fields, describing its formulation, numerical implementation, results, and analysis. The linearized LLG equation solver is finally extended to create a harmonic balance solver, which represents the solution as a set of multiple frequency components with an iterative process, which allows computing the excitation coefficients of these components. All the codes are developed in the finite element method framework, which is flexible in handling complex materials and devices, and it is integrated with the high-performance micromagnetic FastMag framework.

INTRODUCTION

Technologies based on magnetic materials are used in various aspects of our daily life. Applications such as magnetic hard drives play an essential role in modern computer and other electronic devices. Over the past decades, the demand for storage capacity is constantly increasing, e.g., for the modern large data consumption and cloud services. Microelectronics is confronting the stagnation of their computational power scaling, which is a major threat to the future growth. Spintronic devices are envisioned as the next-generation technology to revolutionize the electronics industry. Unlike the electronic devices which employ circuits that uses the electric charge to represent information, spintronic technology manipulates the electron spins, and it usually requires less energy and provides the non-volatility. These properties are important for many modern applications, such as the energy-constrained cases for Internet-of Things (IoT), fast non-volatile memories for next generation database system designs. The field of spintronics was born in 1988 with the discovery of Giant Magnetoresistance (GMR), and extensive research has been done over the years. Recent progress suggests that magnetic random access memory (MRAM) devices are the major candidate for future memory technologies. Among MRAM devices, the spin-transfer-torque (STT) MRAM prototypes use perpendicular magnetic anisotropy (PMA) magnetic tunnel junctions (MTJ) as the storage elements. Spin polarized currents are injected to the MTJ and transfer the spin-torque to the free layer for operation. The spin-orbit-torque (SOT) MRAM uses PMA-MTJ with a layer of heavy metal. The in-plane charge current is injected into the heavy metal layer, and the spin Hall effect generates a spin current, which imposes a torque on the free layer of the MTJ for operation. These spin-torque-driven MRAMs have high sensitivity, low power consumption, non-volatility, fast read and write operation, and high

endurance. These properties provide several advantages over the currently used static RAM for high-speed applications, flash for non-volatility, and dynamic RAM for low energy consumption.

This dissertation presents mathematical formulations of using the Landau-Lifshitz-Gilbert (LLG) equation in its linear approximation to study the linear and non-linear magnetization dynamics in complex nanomagnetic materials and devices. The mathematical formulations are implemented in numerical codes that are integrated with the FastMag micromagnetic framework, which is a high-performance general micromagnetic simulator developed at UCSD. The developed formulations and numerical solvers are used for the analysis and design of MRAM elements. The dissertation is divided into seven chapters.

Chapter 1 presents a summary of the fundamentals of Micromagnetics focusing on the most important interactions that are considered in general models, and how these interactions are accounted for in the FastMag framework.

Chapter 2 introduces spin-torque-driven spintronic devices, with an emphasis on STT MRAM. The basic architectures of MTJs, STT, and SOT MRAM are presented, and the major problems of these devices are discussed.

Chapter 3 presents the construction of an eigenvalue framework based on the linearization of the LLG equation, which is used to study switching of spin-torque-driven devices, including the calculation of the critical current, switching time, and magnetization dynamics.

Chapter 4 studies the switching current reduction using a nonuniform current density distribution in MTJs. It presents an optimization approach for minimizing the critical current based on the eigenvalue framework.

Chapter 5 introduces the Fokker-Planck (FP) approach based on the eigenvalue framework. The probability density function is calculated from the FP equation and is used to study the write error rates with finite temperature for STT-MRAM.

Chapter 6 introduces a finite element method based solver for solving the linearized LLG equation in the frequency domain for complex magnetization amplitude when the system is excited by a time-harmonic applied field, including a preconditioner required for a high computational performance.

Chapter 7 introduces a harmonic balance solver to account for higher-harmonic generation due to the non-linear behavior of the magnetization dynamics under time harmonic excitations.

Finally, Chapter 8 contains conclusion and remarks.

CHAPTER 1

Concepts of Micromagnetics

The magnetic properties of materials are fundamentally described by the quantum theory. For instance, the Pauli paramagnetism and Landau diamagnetism theories give the susceptibility of paramagnetic and diamagnetic materials using quantum theory and statistical physics. The quantum theory of ferromagnets is described as a many-body problem, and the complexity grows exponentially with the number of involved bodies. Therefore, analytical and numerical calculations in this scheme are limited to small systems only. Micromagnetics, on the other hand, is a continuum theory that describes magnetic interactions in materials and devices on a few nanometers to hundreds of micron scales. The original theory is described by Brown [1] who developed a continuous theory predicting the equilibrium magnetization state. Micromagnetics can leverage the computation power of modern computers to perform simulations to study various magnetic materials and devices, such as magnetic hard drives for magnetic recording and MRAM. This chapter discusses fundamentals of the micromagnetic theory. It starts with the governing equation, viz. the LLG equation. It, then, describes how the major magnetic interactions are modeled in Micromagnetics. Then, it discussed thermal effects and energy barrier calculations in Micromagnetics. Finally, it discusses uses of the micromagnetic formulations for computational model.

1.1 Landau-Lifshitz-Gilbert equation

The magnetization dynamics and interactions in magnetic systems are described by the Landau-Lifshitz equation:

$$\frac{d\mathbf{M}}{dt} = -\gamma \mathbf{M} \times \mathbf{H}_{eff} - \gamma \frac{\lambda}{M_s} \mathbf{M} \times (\mathbf{M} \times \mathbf{H}_{eff}),\qquad(1.1)$$

where γ is the gyromagnetic ratio, $\mathbf{M}$ is the magnetization vector, M_s is the saturation

magnetization, $\mathbf{H}_{eff}$ is the effective magnetic field, and λ is the phenomenological damping

parameter [2]. In 1955 Gilbert replaced the damping parameter in the Landau-Lifshitz equation by

a term that depends on the time derivative of the magnetization, which resulted in the LLG

equation [3]:

$$\frac{d\mathbf{M}}{dt} = -\gamma \mathbf{M} \times \mathbf{H}_{eff} + \frac{\alpha}{M_s} \mathbf{M} \times \frac{d\mathbf{M}}{dt},\qquad(1.2)$$

where α is the unitless damping factor. The LLG equation has the form of the LL equation if the

gyromagnetic ratio γ in the Landau-Lifshitz equation is replaced by the modified gyromagnetic

ratio $\gamma' = \gamma / (1 + \alpha^2)$, and $\alpha = \lambda$ [3]:

$$\frac{d\mathbf{M}}{dt} = -\gamma' \mathbf{M} \times \mathbf{H}_{eff} - \gamma' \frac{\alpha}{M_s} \mathbf{M} \times (\mathbf{M} \times \mathbf{H}_{eff}),\qquad(1.3)$$

where (1.2) and (1.3) are usually referred as implicit and explicit forms of the LLG equation. The

right hand side of (1.3) consists of two terms. The first term, $\mathbf{M} \times \mathbf{H}_{eff}$, describes the precession of

magnetic vector $\mathbf{M}$ about the effective field $\mathbf{H}_{eff}$, and the second term, $\mathbf{M} \times (\mathbf{M} \times \mathbf{H}_{eff})$, describes

damping, which leads the magnetic vector $\mathbf{M}$ to align with the effective field $\mathbf{H}_{eff}$. The illustration

of these two terms is shown in Figure 1.1. The LLG equation is often written in a normalized form

for the normalized magnetization $\mathbf{m} = \mathbf{M}/M_s$

$$\frac{d\mathbf{m}}{dt} = -\gamma' \mathbf{m} \times \mathbf{H}_{eff} - \gamma' \alpha \mathbf{m} \times (\mathbf{m} \times \mathbf{H}_{eff}),\qquad(1.4)$$

The LLG equation is a non-linear differential equation where the effective field $\mathbf{H}_{eff}$ is a

function of magnetization vector $\mathbf{M}$. The major interactions considered in Micromagnetics that contribute to the effective field $\mathbf{H}_{eff}$ are discussed in Sec. 1.2.
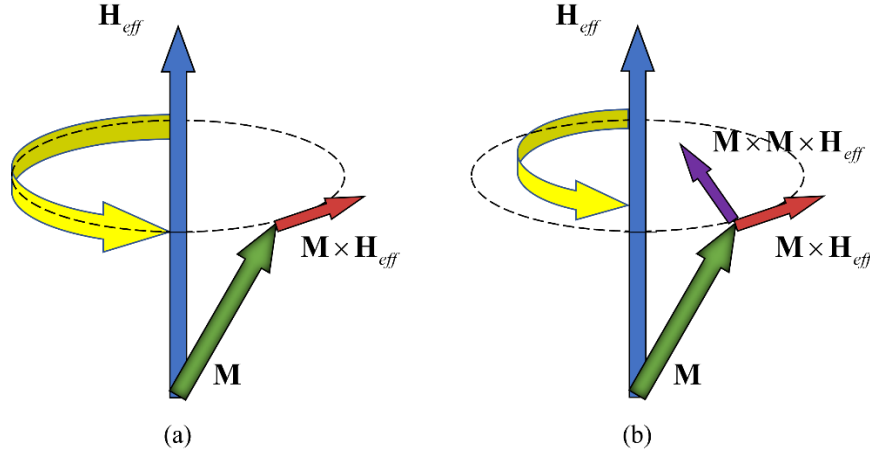
Figure 1.1: Illustration of the magnetization with (a) precession term only and (b) damping term of the LLG equation.

1.2 Major interactions in micromagnetics

The effective magnetic field $\mathbf{H}_{eff}$ in the LLG equation can be expressed as the sum of magnetic fields originating from different interactions. Several major interactions are generally considered in micromagnetic systems:

$$\mathbf{H}_{eff} = \mathbf{H}_{a} + \mathbf{H}_{ms} + \mathbf{H}_{ex} + \mathbf{H}_{anis}, \tag{1.5}$$

where $\mathbf{H}_{a}$ is the Zeeman or applied field, $\mathbf{H}_{ms}$ is the magnetostatic field, $\mathbf{H}_{ex}$ is the exchange field, and $\mathbf{H}_{anis}$ is the magnetocrystalline anisotropy field. In general, the magnetic field from each interaction $\mathbf{H}$ can be calculated from the functional derivative of the magnetic energy E with respect to the magnetization vector $\mathbf{M}$ [4]:

$$\mathbf{H} = -\frac{dE}{d\mathbf{M}}. \tag{1.6}$$

This section discusses the physics background of magnetic fields in (1.5).

1.2.1 Zeeman interactions

The Zeeman interactions are between an external applied field (Zeeman field) $\mathbf{H}_a(\mathbf{r})$ and the magnetization vector. The Zeeman energy is given by

$$E_{Zee} = -\int_{\Omega} \mathbf{M}(\mathbf{r}) \cdot \mathbf{H}_a(\mathbf{r}) dV , \qquad (1.7)$$

where Ω denotes the magnetic domain of interest. As indicated by (1.7), the energy E_{Zee} is lowest when the magnetization vector $\mathbf{M}$ is oriented along the field $\mathbf{H}_a$.

1.2.2 Magnetostatic interaction

To introduce the magnetostatic interactions, consider two magnetic dipole moments, $\boldsymbol{\mu}_1$ and $\boldsymbol{\mu}_2$, that generate the corresponding magnetic fields, $\mathbf{H}_1$ and $\mathbf{H}_2$. By the reciprocity theorem [5], the total energy of the two magnetic moments, denoted as magnetostatic energy E_{ms}, can be expressed as:

$$E_{ms} = -\frac{1}{2}(\boldsymbol{\mu}_2 \cdot \mathbf{H}_1 + \boldsymbol{\mu}_1 \cdot \mathbf{H}_2) , \qquad (1.8)$$

where the factor of $1/2$ excludes the self-interaction. For the general magnetic materials that contain multiple magnetic moments, (1.8) generalizes to

$$E_{ms} = -\frac{1}{2}\sum_i \sum_{j \neq i} \boldsymbol{\mu}_i \cdot \mathbf{H}_j . \qquad (1.9)$$

For a continuum representation in terms of the magnetization vector $\mathbf{M}(\mathbf{r})$, similar to (1.7), the magnetostatic energy E_{ms} is given by

$$E_{ms} = -\frac{1}{2}\int_{\Omega} \mathbf{M}(\mathbf{r}) \cdot \mathbf{H}_{ms}(\mathbf{r}) dV , \qquad (1.10)$$

where $\mathbf{H}_{ms}(\mathbf{r})$ is the magnetostatic (demagnetization) field generated by the magnetization. The

magnetostatic field can be found by using the magnetic charge density

$$\mathbf{H}_{ms}(\mathbf{r}) = -\nabla \int_{\Omega} \frac{\rho_M(\mathbf{r}')}{|\mathbf{r}-\mathbf{r}'|} dV' - \nabla \int_{S_\Omega} \frac{\sigma_M(\mathbf{r}')}{|\mathbf{r}-\mathbf{r}'|} ds' , \qquad (1.11)$$

where S_Ω is the surface of Ω, and $\rho_M(\mathbf{r})$ and $\sigma_M(\mathbf{r})$ denote the volume and surface magnetic

charge densities

$$\begin{aligned}\rho_M(\mathbf{r}) &= -\nabla \cdot \mathbf{M}(\mathbf{r}) \\ \sigma_M(\mathbf{r}) &= \hat{\mathbf{n}}(\mathbf{r}) \cdot \mathbf{M}(\mathbf{r})\end{aligned}, \qquad (1.12)$$

and $\hat{\mathbf{n}}(\mathbf{r})$ is the outward unit normal vector on surface S_Ω.

(a)

(b)
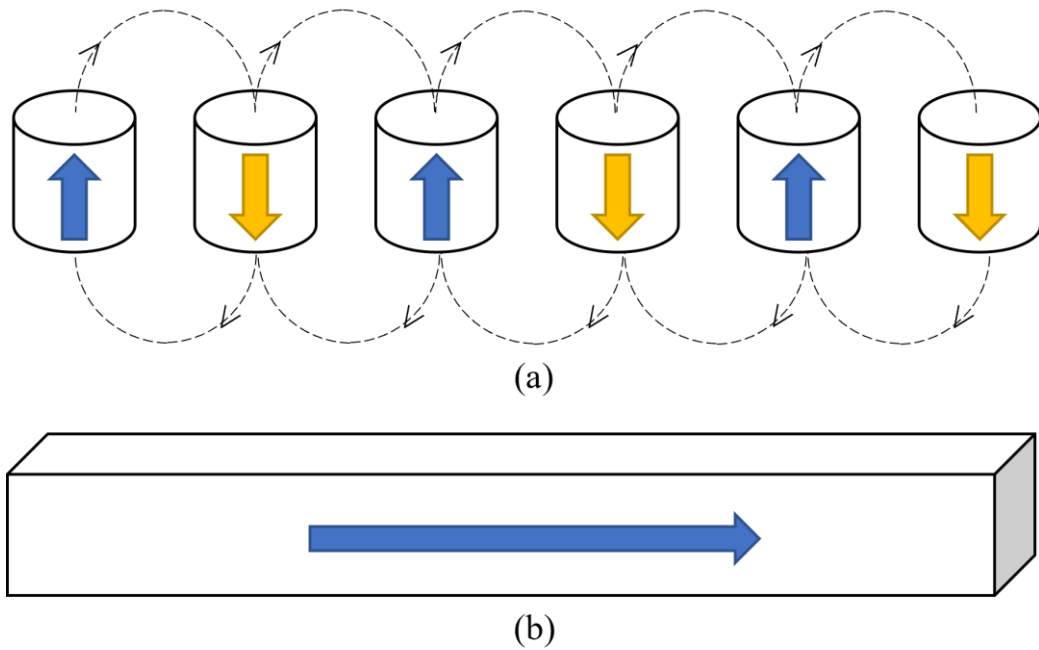
Figure 1.2: Illustration of the magnetostatic interaction of (a) an array of uniform magnetic pillars, and (b) long magnetic nanowire.

The magnetostatic interactions play an important role in the static and dynamic properties

of magnetic materials. Figure 1.2 shows effects of the magnetostatic interaction in several

configurations. Figure 1.2a shows the magnetization configuration of an array of uniform magnetic

pillars, each pair of neighboring pillars is anti-paralleled to minimize the magnetostatic energy. Figure 1.2b shows the magnetization configuration of a magnetic wire, where the minimum magnetostatic energy is achieved when the magnetization aligns with the long axis. More generally, unless other effects dominate, the magnetostatic interaction promotes the magnetization to align in the longer direction of the sample, since this configuration minimizes the surface magnetic charge $\sigma_M(\mathbf{r})$ (see (1.12)), which is the effect called shape anisotropy.

In the general micromagnetic systems, calculating the magnetostatic field can be expensive, since the complexity of computation scales quadratically with the number of the magnetic moments in the system. Consequently, the calculation of the magnetostatic field may be the bottleneck in micromagnetic simulations, especially for large magnetic systems. Several algorithms have been proposed to decrease the computation complexity, such as using the nonuniform fast Fourier transform (NUFFT) [6]. On the other hand, when consider the macrospin approximation, i.e., when assuming that the magnetization is uniform within the entire volume, the demagnetization factor, $\tilde{\mathbf{N}}$, is usually used to calculate the magnetostatic field. The demagnetization factor is a tensor used to represent $\mathbf{H}_{ms}$ in terms of $\mathbf{M}$ as

$$\mathbf{H}_{ms} = -\tilde{\mathbf{N}}\mathbf{M} = -\begin{pmatrix} N_{xx} & N_{xy} & N_{xz} \\ N_{yx} & N_{yz} & N_{yz} \\ N_{zx} & N_{zy} & N_{zz} \end{pmatrix}\mathbf{M} , \qquad (1.13)$$

where the component N_{ij} indicates contribution of the magnetization component M_j to the magnetostatic field component $H_{ms,i}$. The value of elements in $\tilde{\mathbf{N}}$ depends on the geometry of the system, and sometimes can be gained from the symmetry of the system. For example, for a sphere, $\tilde{\mathbf{N}}$ has equal elements on its diagonal, where $N_{xx} = N_{yy} = N_{zz} = 4\pi/3$ and zero elements elsewhere, which means that the sphere does not have a preferred direction of the magnetization.

For an infinite thin film in the xy plane, $\tilde{\mathbf{N}}$ has only a single non-zero element $N_{zz} = 4\pi$. The demagnetization factors of some other commonly used shapes are discussed below. First, the demagnetization factor $\tilde{\mathbf{N}}$ of a finite length cylinder with the z axis of height h and radius r is [7]

$$
\begin{aligned}
N_{zz} &= 4\pi(1+l-\sqrt{1+l^2}), \quad l = r/h \\
N_{xx} &= N_{yy} = 2\pi - N_{zz}/2 \\
N_{ij,i\neq j} &= 0
\end{aligned}
\qquad (1.14)
$$
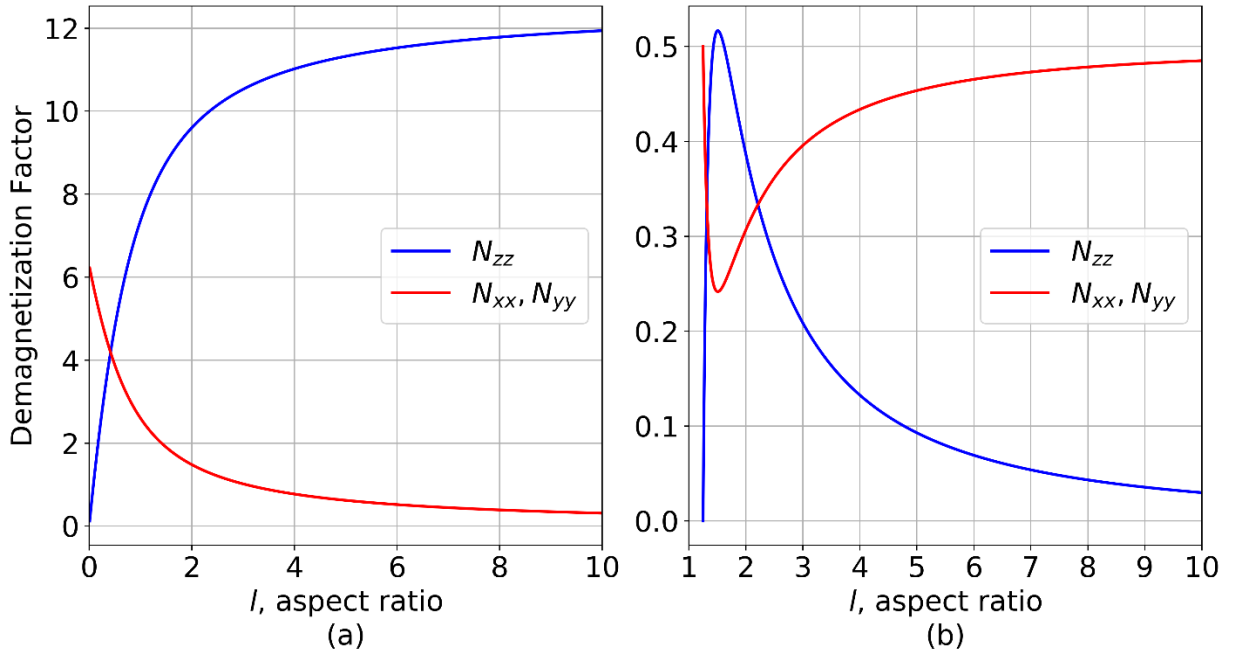
Figure 1.3: Demagnetization factors N_{xx}, N_{yy}, N_{zz} as a function of aspect ratio l for (a) circular cylinder and (b) prolate spheroid.

For a prolate spheroid with axis of length $a = b < c$, where c is in the z axis [8], the demagnetization factor is

$$
\begin{aligned}
N_{zz} &= \frac{4\pi}{l^2-1}\left[\frac{l}{\sqrt{l^2-1}}\ln\left(l+\sqrt{l^2-1}-1\right)\right], \quad l = c/a \\
N_{xx} &= N_{yy} = 2\pi - N_{zz}/2 \\
N_{ij,i\neq j} &= 0
\end{aligned}
\qquad (1.15)
$$

Figure 1.3 shows the demagnetization factor components as a function of the aspect ratio l for a cylinder and prolate spheroid.

1.2.3 Magnetocrystalline anisotropy interaction

Anisotropy interactions describe the effect of the magnetic material having different properties in different directions, which leads the anisotropy magnetic energy to have minima directions in which the magnetization tend to stay. Two common types of magnetocrystalline anisotropy are uniaxial and cubic. The uniaxial anisotropy has a single easy axis so that the magnetization has two opposite favorable directions. This property is used, e.g., for representing a bit element in data storage, where the two preferential directions are used as 0 and 1. The uniaxial anisotropy energy and magnetic field are written as [9,10]

$$
\begin{aligned}
E_{anis}^{uniaxial} &= \int_{\Omega} \left[K_1^U \left(1 - (\mathbf{m}(\mathbf{r}) \cdot \hat{\mathbf{k}})^2 \right) + K_2^U \left(1 - (\mathbf{m}(\mathbf{r}) \cdot \hat{\mathbf{k}})^2 \right)^2 \right] dV \\
\mathbf{H}_{anis}^{uniaxial}(\mathbf{r}) &= \frac{2K_1^U}{M_s} (\mathbf{m}(\mathbf{r}) \cdot \hat{\mathbf{k}}) \hat{\mathbf{k}} + \frac{4K_2^U}{M_s} \left(1 - (\mathbf{m}(\mathbf{r}) \cdot \hat{\mathbf{k}})^2 \right) \left(\mathbf{m}(\mathbf{r}) \cdot \hat{\mathbf{k}} \right) \hat{\mathbf{k}}
\end{aligned}
\tag{1.16}
$$

where $\hat{\mathbf{k}}$ is the uniform anisotropy easy axis vector and K_i^U is the i-th order uniaxial anisotropy energy density.

(a)   (b)
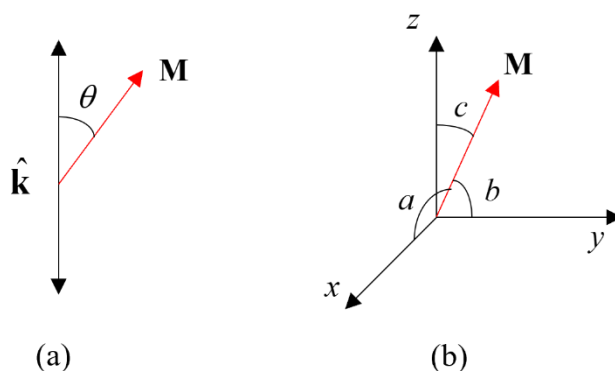
Figure 1.4: Anisotropy field illustration for (a) uniaxial and (b) cubic anisotropy

For the macrospin approximation, for which the magnetization is uniform, (1.16) simplifies to

$$E_{anis}^{uniaxial} = K_1^U V \sin^2 \theta + K_2^U V \sin^4 \theta$$

$$\mathbf{H}_{anis}^{uniaxial}(\mathbf{r}) = \frac{2K_1^U}{M_s}\cos\theta\,\hat{\mathbf{k}} + \frac{4K_2^U}{M_s}\sin^2\theta\cos\theta\,\hat{\mathbf{k}} \quad , \tag{1.17}$$

where θ is the angle between $\mathbf{m}$ and $\hat{\mathbf{k}}$ (Figure 1.4a).

For cubic anisotropy, the magnetocrystalline energy is expressed as a power series of the directional cosines of the magnetization vector $\mathbf{m}$. The directional cosines are defined as $\alpha_1 = \cos a, \alpha_2 = \cos b$ and $\alpha_3 = \cos c$, where a, b, c are the angles between the magnetization vector and the principal crystallographic axes (Figure 1.4b). Here, for simplicity, assuming the macrospin approximation, the cubic anisotropy energy and field can be expressed as [9,10]

$$E_{anis}^{cubic} = K_1^C(\alpha_1^2\alpha_2^2 + \alpha_2^2\alpha_3^2 + \alpha_1^2\alpha_3^2) + K_2^C\alpha_1^2\alpha_2^2\alpha_3^2$$

$$\mathbf{H}_{anis}^{cubic} = -\frac{2}{M_s}\begin{bmatrix} K_1^C\alpha_1(\alpha_2^2 + \alpha_3^2) + K_2^C\alpha_1\alpha_2^2\alpha_3^2 \\ K_1^C\alpha_2(\alpha_1^2 + \alpha_3^2) + K_2^C\alpha_1^2\alpha_2\alpha_3^2 \\ K_1^C\alpha_3(\alpha_1^2 + \alpha_2^2) + K_2^C\alpha_1^2\alpha_2^2\alpha_3 \end{bmatrix} \quad , \tag{1.18}$$

where K_i^C is the i-th order cubic anisotropy energy density.

1.2.4 Exchange interaction

Exchange interactions are the source of ferromagnetism, antiferromagnetism, and ferrimagnetism since they maintain the magnetic order. The exchange interaction is a quantum effect that leads to an energetically favored parallel alignment of the neighboring spins in magnetic materials. Considering the Heisenberg model [11], the energy $E_{i,j}$ between two neighboring spins $\mathbf{S}_i, \mathbf{S}_j$ is given by

$$E_{i,j} = -J_{ex}\mathbf{S}_i \cdot \mathbf{S}_j, \tag{1.19}$$

where J_{ex} is the exchange integral. The sign of J_{ex} determines whether the parallel or anti-parallel alignment of the neighboring spins has a lower energy. When $J_{ex} > 0$, a parallel alignment between $\mathbf{S}_i, \mathbf{S}_j$ has a lower energy, which leads to ferromagnetism, and when $J_{ex} < 0$, an anti-parallel alignment between $\mathbf{S}_i, \mathbf{S}_j$ has a lower energy, which leads to either antiferromagnetism or ferrimagnetism, depending on whether the total magnetization is zero or not. Figure 1.5 shows the type of the strong magnetic material and the corresponding alignment of the spins.

$$J_{ex} > 0$$

(a)

$$J_{ex} < 0$$

(b)
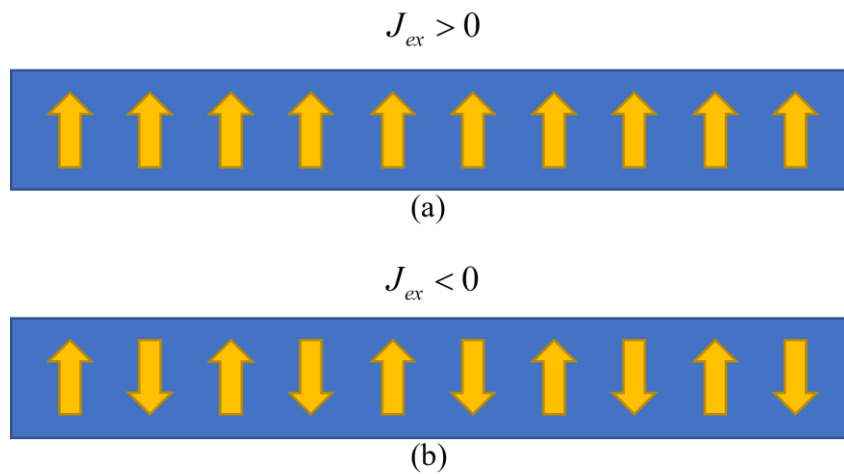
Figure 1.5: Magnetic moment order of (a) ferromagnetic and (b) anti ferromagnetic materials.

Equation (1.19) presents the quantum effect of exchange interaction between two spins. In Micromagnetics, the continuous theory represents the exchange interaction energy and magnetic field as

$$
\begin{aligned}
E_{ex} &= \int_\Omega A_{ex} \left(\nabla \mathbf{m}(\mathbf{r}) \right)^2 dV \\
\mathbf{H}_{ex} &= \frac{2A_{ex}}{M_s^2} \nabla^2 \mathbf{m}(\mathbf{r}) \triangleq l_{ex}^2 \nabla^2 \mathbf{m}(\mathbf{r})
\end{aligned}
\qquad (1.20)
$$

where A_{ex} is the exchange energy density that depends on J_{ex} [11]: $A = \frac{1}{6} n J_{ex} S^2 \sum_j r_j^2$, where n is the number of nearest neighbors, S is the spin magnitude, and r_j is the distance to the nearest neighbor. The parameter $l_{ex} = \sqrt{2A_{ex}}/M_s$ is usually referred as the exchange length. The micromagnetic expression in (1.20) is an approximation, which assumes that the magnetization varies slowly in space, and the rate of the variations is given by the exchange length. To characterize the exchange interaction numerically, these slow variations need to be resolved, which means that the spatial discretization of the system should have a mesh size sufficiently smaller than l_{ex}.

The exchange interactions discussed above are referred to as bulk exchange. There is another type of exchange interaction, referred to as surface exchange, which originates from the Ruderman-Kittel-Kasuya-Yosida (RKKY) interactions [12].

1.3 Thermal effects and stochastic LLG equation

Thermal effects have a large impact on the properties of magnetic materials, and it is necessary to consider the thermal effect in theoretical and numerical studies. When the environment temperature is high, it may break the magnetic order, which is associated with the Curie temperature T_C. The temperature also influences the susceptibility χ of the magnetic material, which for $T < T_C$, can be expressed via the Curie-Weiss law:

$$\chi = \frac{C}{T - T_C},$$
(1.21)

where C is Curie constant that depends on the material properties (Figure 1.6).
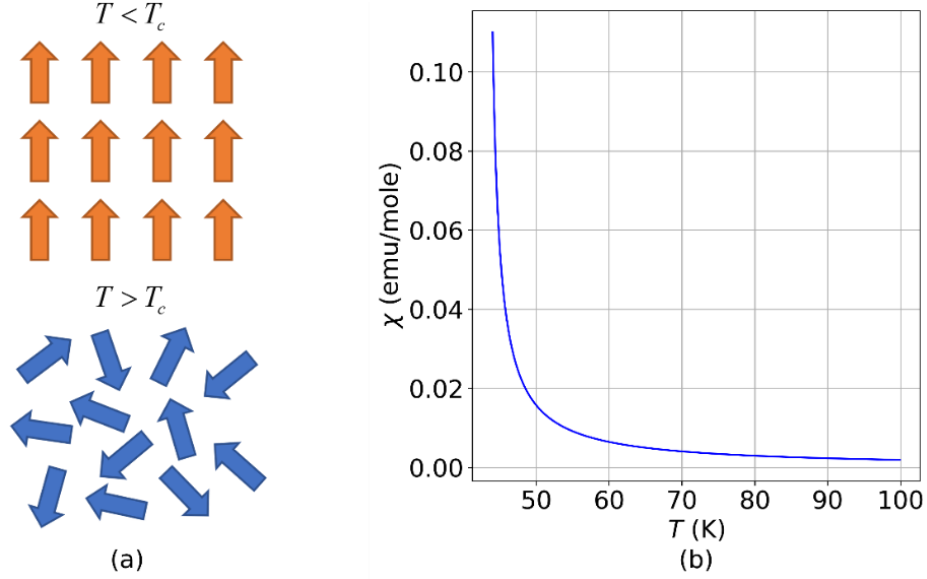
Figure 1.6: (a) Magnetic moments order under (top) and above (bottom) Curie temperature. (b) Magnetic susceptibility vs. temperature above Curie temperature following Curie-Weiss law.

In Micromagnetics, for sufficiently low temperatures, thermal effects can be expressed as an additional term in the effective field $\mathbf{H}_{eff}$ in (1.5). This thermal field $\mathbf{H}_{th}$ can be expressed as a Gaussian white noise (GWN) [13]

$$\mathbf{H}_{th} = \sqrt{\frac{2\alpha k_B T}{\gamma V M_S}}\mathbf{G} \, , \tag{1.22}$$

where k_B is the Boltzmann constant and $\mathbf{G}$ is a three dimensional normalized GWN with $<\mathbf{G}>=0$ and $<\mathbf{G}^2>=1$, where $<x>$ denotes the expectation of x. Adding the thermal field $\mathbf{H}_{th}$ to the LLG equation (1.3), we obtain the stochastic LLG equation

$$\frac{\partial \mathbf{M}}{\partial t} = -\gamma'\mathbf{M}\times(\mathbf{H}_{eff}+\mathbf{H}_{th}) - \gamma'\frac{\alpha}{M_s}\mathbf{M}\times\mathbf{M}\times(\mathbf{H}_{eff}+\mathbf{H}_{th}) \, . \tag{1.23}$$

Note that (1.23) is only applicable when $T \ll T_C$. When T is close to T_C, the total spontaneous magnetization decreases significantly, and (1.23) is not valid. In that case, the Landau-Lifshitz-Bloch (LLB) equation should be used instead [14].

1.4 Nudged elastic band method

In general physics systems, it may be important to know the minimum energy path and barrier between two equilibrium states. In Micromagnetics, knowing the minimum energy path is important for the study of the switching properties of devices, and the energy barrier is also critical for understanding the thermal stability. The thermal stability lifetime τ for a magnetic structure is related to the ratio between the energy barrier E_b and the temperature [15]:

$$\tau = \tau_0 e^{\frac{E_b}{k_B T}}, \tag{1.24}$$

where τ_0 is inverse of the attempt frequency, with typical values on the order of $10^{-10} s$. The lifetime τ exponentially increases with $E_b/k_B T$. As an example, for $E_b/k_B T = 20$, the lifetime $\tau < 1s$. For $E_b/k_B T = 45$, the lifetime $\tau \sim 10$ years, which is the minimum requirement for retaining information in magnetic recording. For $E_b/k_B T = 100$, the lifetime is greater than the age of the universe. The typical value of $E_b/k_B T$ for current magnetic recording or memories is about 80, which accounts for the possibilities of the lifetime reduction due to imperfections in fabrication and parameter distributions.

Nudged elastic band (NEB) method is a widely used method for finding the saddle points to find minimum energy path and energy barrier [16].NEB method works by optimizing a number of intermediate magnetization states $\{\mathbf{M}_n\}$, referred to as image to lead to the energy to follow the minimal path. The path is found by an energy gradient descent method [16–18]

$$\begin{aligned}\frac{d\mathbf{M}_n}{d\xi_{NEB}} &= -\left[\nabla E_n - \left(\nabla E_n \cdot \boldsymbol{\tau}_n\right)\boldsymbol{\tau}_n\right] \\ \boldsymbol{\tau}_n &= \frac{\mathbf{M}_{n+1} - \mathbf{M}_{n-1}}{\|\mathbf{M}_{n+1} - \mathbf{M}_{n-1}\|}\end{aligned}, \tag{1.25}$$

16

where ∇E_n is the gradient of energy for image n associated with magnetization state $\mathbf{M}_n$, $d\xi_{NEB}$ is an integration parameter and, $\boldsymbol{\tau}_n$ is the unit tangent vector to the energy path. The initial guess path can assume a uniform switching or any approximation to the minimal energy path.

1.5 Micromagnetic modeling

The Computational Electromagnetics and Micromagnetics group at UCSD has developed a high-performance micromagnetic simulator FastMag [19]. FastMag is a finite element method (FEM) based micromagnetic simulator,

(a)   (b)
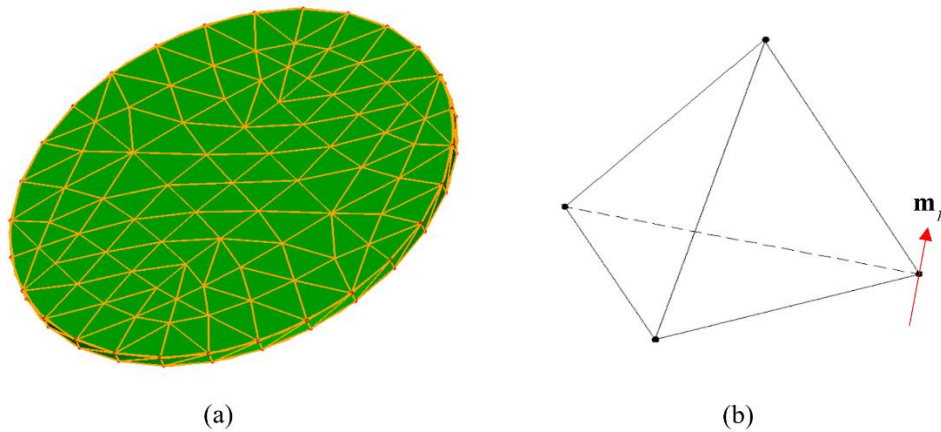
Figure 1.7: Finite element mesh of (a) a general case and (b) one tetrahedral element.

which can run on multicore CPUs and GPUs to efficiently handle highly complex structures [19]. The codes developed in the framework on this dissertation use various modules of FastMag. This section describes several relevant aspects of the FastMag based computations.

Figure 1.7a shows a tetrahedral discretization mesh example of a disc and Figure 1.7b shows one tetrahedral element of the mesh. The normalized magnetization vector is prescribed to the tetrahedral vertices, viz. the mesh nodes. The magnetization vector inside the tetrahedral can be expressed using the magnetization vector values at the nodes

$$\mathbf{m}^l(\mathbf{r}) = \sum_p \xi_p^l(\mathbf{r}) \mathbf{m}_p^l(\mathbf{r}), \tag{1.26}$$

where l denotes the tetrahedron number and p denotes its vertices (also, referred to as nodes). $\xi(\mathbf{r})$ is a linear basis function with $\xi = 1$ at the node and $\xi = 0$ at the opposite surface of the node. Also in FEM, the effective volume V_p, surface area S_p and thickness t_p at node p are defined as

$$V_p = \frac{1}{4} \sum_l^{M_p} V^l$$

$$S_p = \frac{1}{3} \sum_t^{T_p} S^t, \tag{1.27}$$

$$t_p = V_p / S_p$$

where M_p and T_p denote the tetrahedrons and surfaces that contain the node p.

The magnetostatic, magnetocrystalline anisotropy field and exchange fields at the nodes can be calculated from the magnetization vector at the nodes. For exchange field,

$$\mathbf{H}_{ex,p} = \frac{2A_{ex,p}}{M_{s,p}} \sum_l \sum_q \Lambda_{p,q}^l \mathbf{m}_q^l$$

$$\Lambda_{p,q}^l = -\frac{V^l}{V_p} \nabla \xi_p^l \cdot \nabla \xi_q^l \tag{1.28}$$

For the magnetocrystalline anisotropy field,

$$\mathbf{H}_{anis,p} = \frac{2K_p}{M_{s,p}} \left(\mathbf{m}_p \cdot \mathbf{k}_p \right) \mathbf{k}_p. \tag{1.29}$$

For the magnetostatic field

$$\mathbf{H}_{ms,p} = -\nabla \sum_l \int \frac{\rho^l}{|\mathbf{r}' - \mathbf{r}_p|} dV' - \nabla \sum_t \int \frac{\sigma^t}{|\mathbf{r}' - \mathbf{r}_p|} dS'$$

$$\rho^l = -\nabla' \left(M_s(\mathbf{r}') \sum_p \xi_p^l(\mathbf{r}') \mathbf{m}_p^l \right) \tag{1.30}$$

$$\sigma^t = M_s(\mathbf{r}') \hat{\mathbf{n}}' \cdot \sum_p \xi_p^t(\mathbf{r}') \mathbf{m}_p^t$$

18

The magnetic parameter values at the node ($A_{ex,p}, M_{s,p}, K_p, \mathbf{k}_p$) are computed by weighted averaging over the tetrahedral containing the node, e.g., $A_{ex,p} = \sum_{l}^{M_p} A_{ex}^l V^l \Big/ \sum_{l}^{M_p} V^l$. More details of the FEM representation of effective field components can be found in [20]. Using the effective field representations, the LLG equation can be solved in this FEM framework with a time domain integration [19,21].

Chapter 2

Spin-torque-driven devices

Interactions described in Chapter 1 are basic interaction types and more interactions can be included, depending on the physics occurring in a particular material or device. Another class of interactions are related to the spin as considered in the general field of spintronics. The field of spintronics is related to the discovery of giant magnetoresistance (GMR). GMR is a quantum mechanical magnetoresistance effect observed in multilayers consisting of ferromagnetic and non-magnetic conductive layers [22,23], which revolutionized the magnetic recording industry. The recent progress of spintronics suggests that MRAM devices are the major candidate for future memory technologies, especially the spin-torque-driven MRAM. In this chapter, we discuss the spin-torque (ST) driven devices, which are a central topic of this dissertation. We discuss spin transfer torque (STT) and spin orbit torque (SOT) types of ST mechanisms and describe effects of these torques in micromagnetic systems governed by the Landau-Lifshitz-Gilbert-Slonczewski (LLGS) equation. We also discuss several spin-torque-driven devices.

2.1 Spin torque and LLGS equation

2.1.1 LLGS equation

To describe the magnetization dynamics including spin torque (ST) effects, an additional torque term in the LLG equation need to be added to result in the LLGS equation:

$$\frac{d\mathbf{M}}{dt} = -\gamma \mathbf{M} \times \mathbf{H}_{eff} + \frac{\alpha}{M_s} \mathbf{M} \times \frac{d\mathbf{M}}{dt} + \boldsymbol{\tau}_s \, , \tag{2.1}$$

where $\boldsymbol{\tau}_s$ is the spin torque. The torque $\boldsymbol{\tau}_s$ can describe different types of spin torques, including spin transfer torque and spin orbit torque. For example, considering a spin valve or a magnetic tunnel junction, the spin transfer torque can be written as

$$\boldsymbol{\tau}_s = a(J)\mathbf{m} \times \mathbf{m} \times \mathbf{p} + b(J)\mathbf{m} \times \mathbf{p} , \qquad (2.2)$$

where the first term is the damping term, the second term is the field-like term, $\mathbf{p}$ is normalized magnetization vector of the polarizing layer, $a(J)$ and $b(J)$ are parameters dependent on the type of spin torque, i.e., STT or SOT, and J is the density of the injection spin polarized current. Figure 2.1 illustrates the effect of $\boldsymbol{\tau}_s$ in LLGS equation.
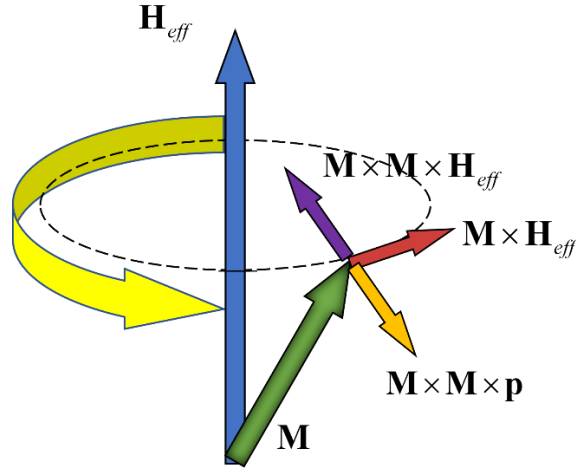
Figure 2.1: Illustration of the magnetization with spin torque of Landau-Lifshitz-Gilbert-Slonczewski equation.

The LLGS equation with the ST term can also be written in an equivalent form, where the ST is considered as a part of the effective field, denoted as $\mathbf{H}_{ST}$

$$\frac{d\mathbf{M}}{dt} = -\gamma' \mathbf{M} \times (\mathbf{H}_{eff} + \mathbf{H}_{ST}) - \gamma' \frac{\alpha}{M_s} \mathbf{M} \times (\mathbf{M} \times (\mathbf{H}_{eff} + \mathbf{H}_{ST})) , \qquad (2.3)$$

where $\mathbf{H}_{ST} = a(J)\mathbf{m} \times \mathbf{p} + b(J)\mathbf{p}$.

2.1.2 Spin transfer torque

When the current flows through the ferromagnet, the electron angular momentum can be transferred to the ferromagnetic lattice. Consequently, the spin unpolarized current can become spin polarized passing through the ferromagnet, and the spin polarized current can transfer its angular momentum and change the magnetization of the ferromagnet. This effect is known as spin transfer torque (STT). Figure 2.2a illustrates the STT effect in a simple five-layer structure. The current flows freely through normal metal (NM) layers and has an STT effect in the ferromagnet (FM) layers. The FMs are soft (no magnetocrystalline anisotropy) with shape anisotropy resulting in the easy axis perpendicular to the current flow. Figure 2.2b shows the STT effect in NM/FM1/NM structure. The normal (spin unpolarized current) flows through the structure. The FM1 layer is thick with a large magnetic moment so that the angular momentum transferred from the electron is not large enough to change the magnetization in FM1, but the opposite interaction changes the polarization of the itinerant electrons. Such structure is called spin polarizer used to generate spin polarized current. Figure 2.2c shows the STT effect in a NM/FM2/NM structure. The injected current is spin polarized generated by NM/FM1/NM. The magnetization of FM2 layer can be switched by the angular momentum transferred from the spin polarized electrons. This effect is used in STT-MRAM devices. Here, we use a one-dimension quantum model of STT originally employed in [24] to illustrate the physics picture of STT. The FM layer imposes different effective potential on different injected current electron spin states. The interaction between the spin up state electrons with the FM can then be described by calculating the transmission and reflection wave functions inside and at the boundary of the potential wall. Considering a difference between the total wave function of spin up electrons in left and right NM layers, we can determine the transferred angular momentum from the electrons to FM layer.
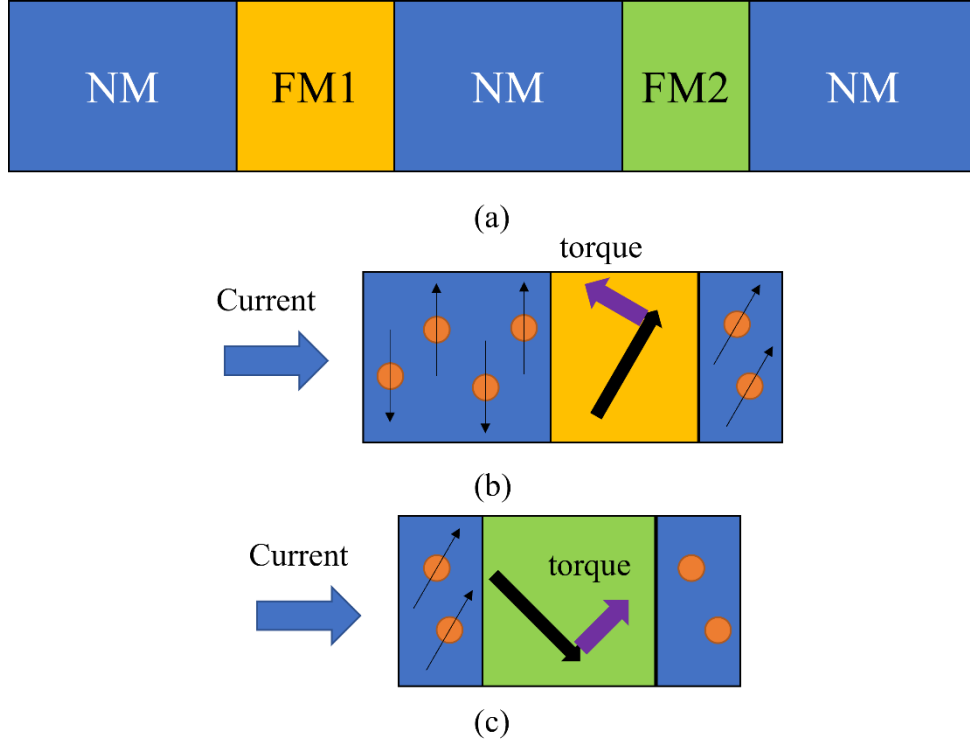
Figure 2.2: (a) NM/FM1/NM/FM2/NM five-layer heterostructure. (b) NM/FM1/NM structure, the input unpolarized current is polarized by FM1 layer. (c) NM/FM2/NM structure, the input polarized current can switch the magnetization in FM2 layer.

The parameters of the STT term in (2.2) can be defined as [24–26]

$$a_{STT}(J) = -\eta \frac{\gamma \hbar}{2eM_s\delta} J$$
$$b_{STT}(J) = -\beta \eta \frac{\gamma \hbar}{2eM_s\delta} J \tag{2.4}$$

where $\hbar$ is the reduced Planck constant, e is the electron charge, δ is the effective thickness of the surface where the current injects in, β is the strength of the field-like STT contribution, whose typical value is 0 to 0.2, and $\eta = \eta(\theta)$ is angular dependent STT efficiency which is a function of the angle θ between **m** and **p** (detailed expressions and discussion for $\eta(\theta)$ can be found in [26]).

2.1.3 Spin orbit torque

Consider a bilayer structure consisting of a FM layer and a non-magnetic heavy metal (HM) layer with strong spin orbit coupling, such as platinum. In this structure, the current flowing along the interface creates torque, referred to as spin orbit torque (SOT) in the FM side of the interface (Figure 2.3).
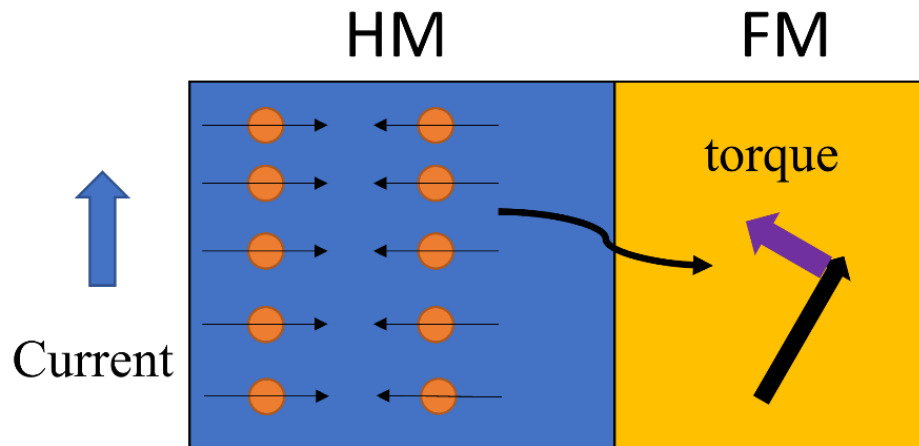
Figure 2.3: Illustration of SOT in HM/FM structure.

There are several models to describe the SOT effect in the HM/FM bilayer structure. The first model considers the HM and FM layers as thick so that they have bulk properties [27]. In this case, the electrons with different spin states in the unpolarized injection current flowing through the HM layer are separated based on the spin state, which is known as the spin Hall effect (SHE). SHE generates a spin polarized current perpendicular to the HM/FM interface. As a result, the spin polarized current flows through the FM layer and generate ST similar to STT discussed in Sec. 2.1.2 (Figure 2.4a). The second model assumes that coupling between the magnetization in FM and the current in HM can be directly described by the Rashba-Edelstein model, which is similar to the model used to describe the spin orbit coupling in the two-dimensional electron gas [28]

(Figure 2.4b). These two models give qualitatively similar results, where the SOT contains both the damping like and field-like torque component. There is also a third model that attempts to unify the first two models based on the Boltzmann equation [29].

(a)   (b)
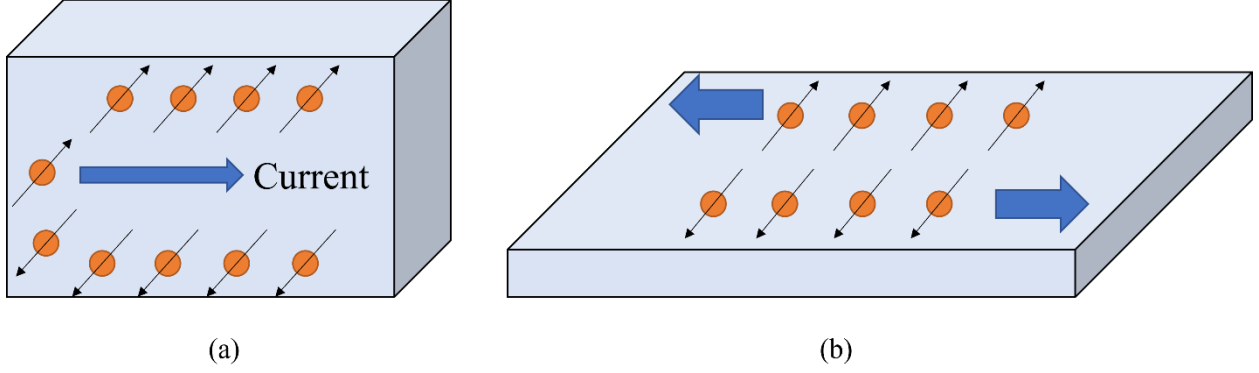
Figure 2.4: Illustration of SOT from (a) spin Hall effect model and (b) Rashba-Edelstein effect model.

In this dissertation, we use the first model to express the SOT in (2.2) as [30,31]

$$
\begin{aligned}
a_{SOT}(J) &= -\tau_d(\theta_{SH}) \frac{\mu_B}{eM_s\delta} J \\
b_{SOT}(J) &= -\tau_f(\theta_{SH}) \frac{\mu_B}{eM_s\delta} J
\end{aligned}
, \tag{2.5}
$$

where μ_B is the Bohr magnetron, and $\tau_d(\theta_{SH})$ and $\tau_f(\theta_{SH})$ characterize the damping and field-like contributions, and they both are functions of the spin Hall angle θ_{SH}. $\tau_d(\theta_{SH})$ and $\tau_f(\theta_{SH})$ are also related to the material properties, such as the spin diffusion length of the HM layer. Detailed expressions and discussions for $\tau_d(\theta_{SH})$ and $\tau_f(\theta_{SH})$ can be found in [30].

2.2 Spin-torque-driven devices

Spin torques give rise to new opportunities to device designs. Spin torque driven devices are envisioned as a promising candidate for future fast memory and low power consumption applications. We discuss several of such devices in this section.

2.2.1 Magnetic tunnel junction

Magnetic tunnel junctions (MTJs) are used in many of the current prototypes of spintronic devices. An MTJ has a multilayer structure consisting of two FM layers, such as Fe, Co and Ni, separated by a thin insulating layer. The left FM layer in MTJ is referred to as free layer (FL) and reference layer (RL), respectively. The magnetization of the RL is usually fixed, and the binary information that the MTJ stores is represented by the relative magnetization of the FL to RL. The MTJ structure has a greater electric resistance when the magnetization of FL anti-parallels to RL, and a lower resistance when they are parallel. This effect is known as tunnel magnetoresistance (TMR), which defines a binary state structure that can be used in storage and memory systems (e.g., large resistance represents state 0 and low resistance represents state 1). The origin of TMR is in the electron energy band misalignment between the FL and RL. When magnetization of FL is parallel to that of RL (Figure 2.5a), the spin up and down energy band in FL aligns with that of RL, but misaligns when they are anti-parallel (Figure 2.5b). The energy band misalignment leads to the electron density of the state difference in FL and RL. According to Fermi's golden rule, the electric resistance is large when flowing from the high electron density side to the low electron density side, and consequently results in the TMR effect.

To quantify the TMR effect in MTJ the following ratio is usually used [32]

$$TMR = \frac{R_{AP} - R_P}{R_P},$$
(2.6)

where R_{AP} and R_P are electric resistances for anti-parallel and parallel states, respectively. High *TMR* ratio can be achieved in MTJ devices. Julliere found the *TMR* ratio was 14% at 4.2K in Fe/Ge(-O)/Co in 1975 [33]. The development of the Al_2O_3 tunnel barrier layer led to the first TMR-based magnetic memory in 1995 [34] and reached 70% at room temperature over the years.

The next breakthrough was the development of the MgO tunnel barrier layer with giant *TMR* ratio, which was first predicted in 2001 and observed in the Fe/MgO/FeCo MTJ structure [35]. Later in 2004 and 2006, [36] and [37] discover the *TMR* in the Fe/MgO/Fe structure up to 200% and 180% at room temperature, respectively.

(a)   (b)
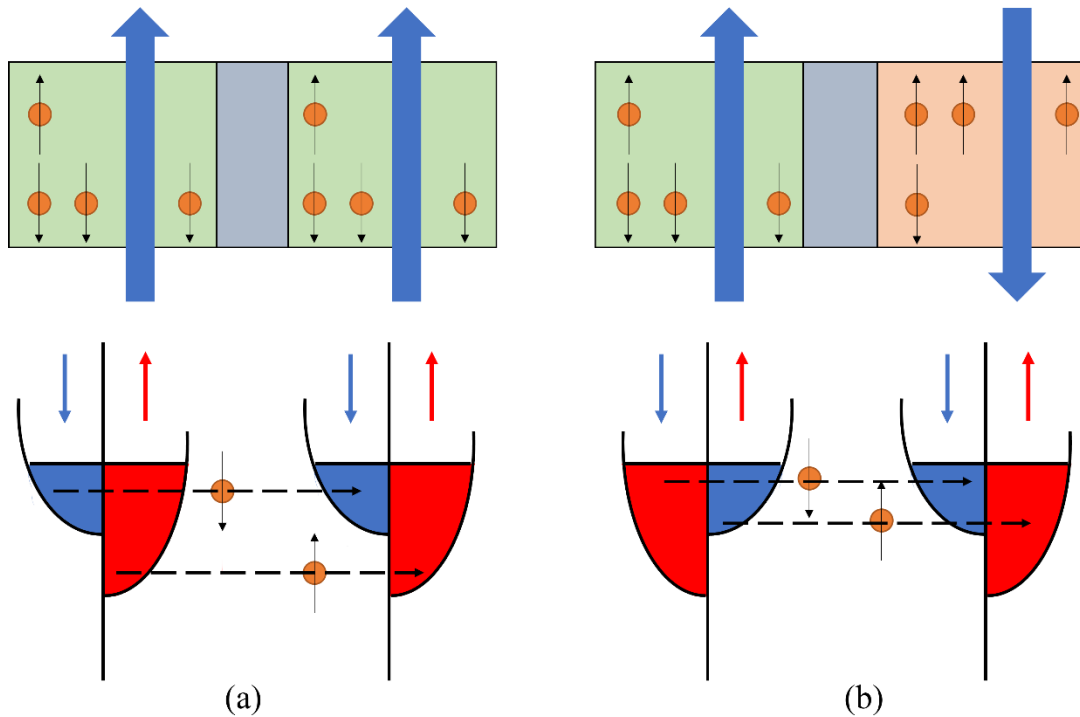
Figure 2.5: Illustration of (a) parallel and (b) anti-parallel state of MTJ.

2.2.2 Spin-transfer-torque MRAM

Spin transfer torque MRAM (STT-MRAM) is a non-volatile memory technology envisioned as a promising candidate for future "universal" memories, including replacing the embedded flash at advanced technology nodes [38]. Current STT-MRAM prototypes are based on MTJs. The reading operation of STT-MRAM is done by measuring the electron resistance of the MTJ. The

spin polarized current is used to exert STT and switch the magnetization state in FL to implement the write operation. Figure 2.6 shows the illustration of STT-MRAM structure.
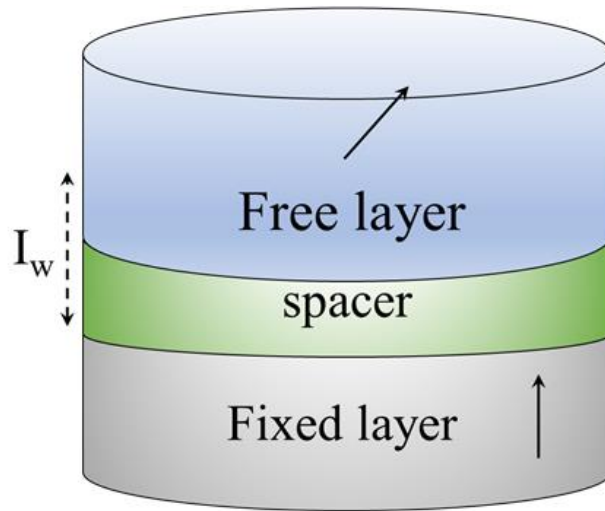
Figure 2.6: Illustration of STT-MRAM.

Schwee first proposed the concept of MRAM in 1972 [39]. Sony proposed the concept of STT-MRAM and demonstrated a 4-kbit functional STT-MRAM chip in 2005 [40]. A 2-Mbit STT-MRAM was first demonstrated in 2007 [41]. Everspin Technologies shipped the commercial STT-MRAM product first in 2012 with a capacity of 64-Mbit [42], and then with a capacity of 256-Mbit in 2018 and 1-Gbit in 2021 [43].

2.2.3 Spin-orbit-torque MRAM

Spin orbit torque MRAM (SOT-MRAM), like STT-MRAM, is also a promising candidate for next-generation non-volatile memories. The writing operation of SOT-MRAM is done by passing the current through the HM to generate SOT in FL and consequently switching the magnetization state. Figure 2.7 shows the illustration of SOT-MRAM structure. Compared to STT-MRAM, SOT-MRAM may have a high and reliable speed at sub-ns levels [38]. This enables the SOT-MRAM to work both as working memories (like dynamic RAM) and cache memories (like static RAM).
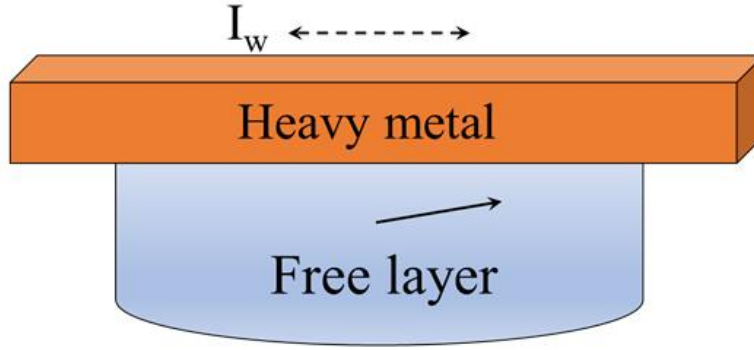
Figure 2.7: Illustration of SOT-MRAM

The concept of SOT-MRAM was first proposed in 2011 by Miron [44] and 2012 by Buhrman [30]. In 2018, SOT-MRAM was first fabricated on 300mm wafers using CMOS compatible process by Imec [45]. Next, Intel demonstrated the next-gen CMOS-compatible SOT-MRAM in 2020 [46], and ISI shipped the first SOT-MRAM tester system in 2021 [47].

2.2.4 Important properties of spin-torque-driven MRAM

Some properties are critical in practical spin-torque-driven MRAM applications, which are one of the focuses of this work. One property is the thermal stability, which determines the life time of its magnetization state (see (1.24)). Considering the FL as small thin disc, for which a macrospin approximation is valid, the energy barrier E_b can be given by [48]

$$E_b = K_{eff} V ,\tag{2.7}$$

where K_{eff} is the effective anisotropy energy density, including both the magnetocrystalline and shape anisotropy. Considering the perpendicular uniaxial magnetocrystalline anisotropy, with the assumption $h \ll D$, where h is the thickness and D is the diameter of the FL, K_{eff} is approximately given by [49,50]

$$K_{eff} = K^U - 2\pi M_s^2, \tag{2.8}$$

where K^U denotes the intrinsic anisotropy energy density, which can be due to bulk intrinsic anisotropy or due to surface anisotropy, in which case $K^U = K_s/h$ with the surface anisotropy energy density K_s. For larger lateral sizes, when the thermal minimal energy path or switching is by domain wall, the energy barrier can be approximately given by [51,52]

$$E_b = 4hD\sqrt{K_{eff}A_{ex}}. \tag{2.9}$$

For more complicated cases, e.g., when accounting for effects of all the layers in the MRAM stack or for sop called bubble switching [53], the NEB method can be used to calculate the barriers (see Sec. 1.4 and [54]). To control the thermal stability, one can either change the geometrical sizes or the magnetic parameters.

The second important property is the required current (density) needed to switch the FL magnetization state for infinite time, viz., the critical current (density). Lower critical current leads to lower energy consumption and faster writing speed for a given driving current. It is important to be able to accurately calculate the critical current. It is also important to be able to reduce the critical current. Under macrospin approximation, the critical writing current I_{c0} can be given as [50]

$$I_{c0} = \frac{4e\alpha}{\eta\hbar} K_{eff}V, \tag{2.10}$$

From here, one can see that the critical current I_{c0} is proportional to the damping factor α, suggesting that the material engineering plays an important role in making STT MRAM a viable storage solution at high bit densities. For general cases where complex switching behaviors such as domain wall or bubble state switching are involved, there are no rigorous analytical models predicting the switching currents and one needs to resort to numerical simulations based on solving

30

LLG equation (1.2). A typical method for obtaining the critical switching current I_{c0} is calculating the switching current at multiple switching times and extrapolating to the infinite time assuming a linear dependence of the switching current versus the inverse time [32]. Figure 2.8a shows an example of calculating I_{c0} using this method from [32]. This method has two major shortcomings. First, it is computationally expensive and time consuming to carry out multiple simulations. Second, the linear assumption can be invalid when the macrospin assumption does not hold. Figure 2.8b shows the inaccuracy this method introduces when the linear assumption fails. Third, when the magnetization starts with precessing around the equilibrium state, it results in slow computations and inaccuracies due to the initial process. Figure 2.9 shows the simulation with different time tolerance of 10^{-9} and 10^{-5}, demonstrating that a very tight computational tolerance may be required, which results in a long computational time.
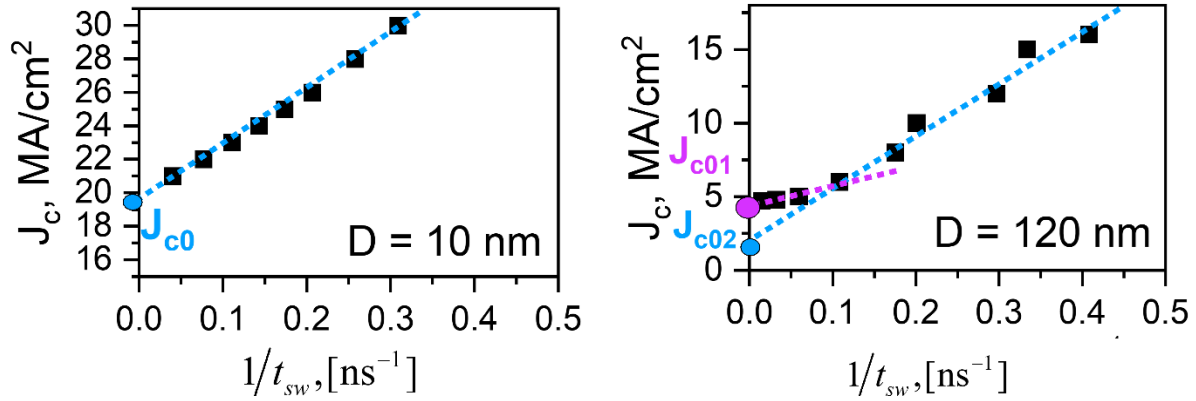
Figure 2.8: Critical current from time domain simulation extraction of (a) small size and (b) large size. For large size the linear assumption is invalid.

The third property is the figure of merit (*FOM*) of the STT-MRAM. *FOM* is defined as the ratio between the energy barrier and critical current

$$FOM = \frac{E_b}{I_{c0}}. \tag{2.11}$$

31

FOM is a useful parameter to characterize the scalability and efficiency of the devices. Larger *FOM* , indicating higher stability and smaller critical current, is desired. However, increasing the energy barrier usually increases the critical current, and can result in a decrease of *FOM* . Figure 2.10 shows the lateral size dependence of the *FOM* [54]. Increasing the size, according to (2.7) and (2.10), increases E_b and I_{c0}, and as a result, *FOM* decreases with the diameter increase.
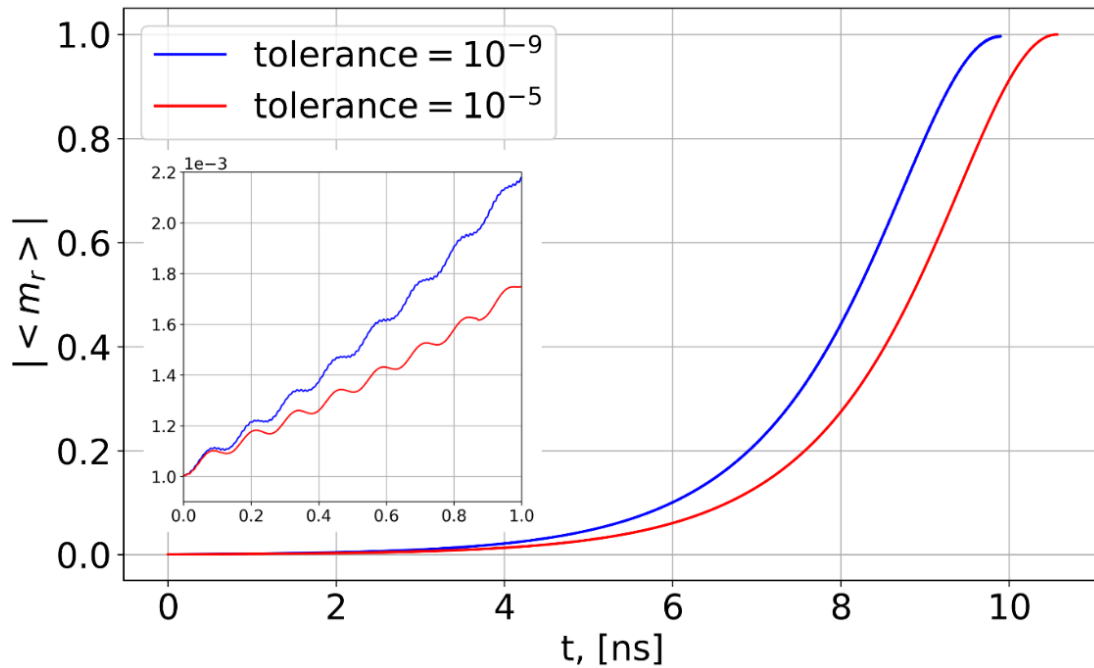
Figure 2.9: Time dynamics difference using different time tolerance in the numerical time evolver of the LLG equation solver with small ST excitation.

Another important characteristic of the MRAM operation is write error rate (WER). Since the devices operate at finite temperatures, spontaneous thermally driven switching or non-switching effects occur. WER is the non-switching probability. The most straight forward way to calculate WER is to perform a large number of the simulations (N_{tot}) and count the number of non-switching events at a certain time t ($N_{ns}(t)$). The WER, i.e., non-switching probability P_{ns} as a function of time t is given by

$$P_{ns}(t) = \frac{N_{ns}(t)}{N_{tot}} . \tag{2.12}$$
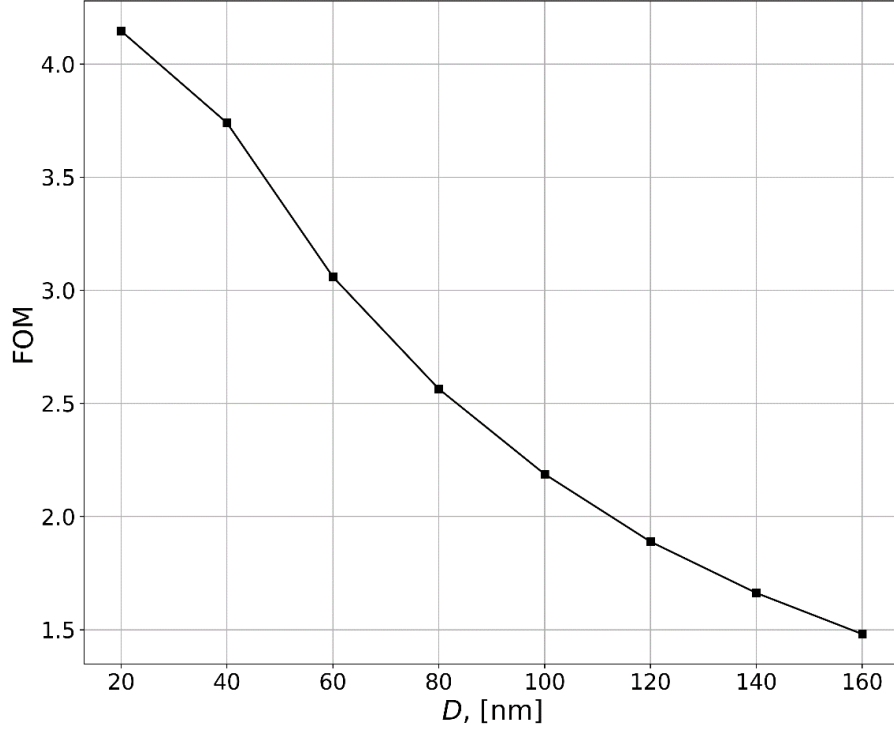
Figure 2.10: FOM for the disc as a function of the lateral size. More results can be found in [54].

This method is certainly expensive. Also, the accuracy of this method is limited by the total number of the system N_{tot}. The highest accuracy this method can achieve is bounded by $1/N_{tot}$. An alternative method is to derive a FP equation, whose solution is the probability density function (PDF) of the system switching. The WER can be calculated from the PDF. This method has been introduced for the macrospin approximation [55,56], where $P_{ns}(t)$ with driven current I and finite temperature T is given by

$$P_{ns}(t) = \int_0^{\pi/2} \rho(\theta;t)\sin\theta d\theta , \tag{2.13}$$

where θ is the angle between the magnetization and the equilibrium direction, and $\rho(\theta;t)$ is the PDF solved from the FP equation

$$\frac{\partial \rho(\theta;t)}{\partial t} = -\frac{1}{\sin\theta}\frac{\partial}{\partial\theta}\left[\sin^2\theta\left(i-\cos\theta\right)\rho(\theta;t) - D\sin\theta\frac{\partial\rho(\theta;t)}{\partial\theta}\right], \tag{2.14}$$

where

$$i = \frac{I}{\dfrac{\alpha}{\eta}\dfrac{2e}{\hbar}H_k M_s V}, \tag{2.15}$$

is the normalized current and

$$D = \frac{k_B T}{2E_b}, \tag{2.16}$$

is the thermal factor. Results from (2.13) and (2.14) are shown in Figure 2.11.
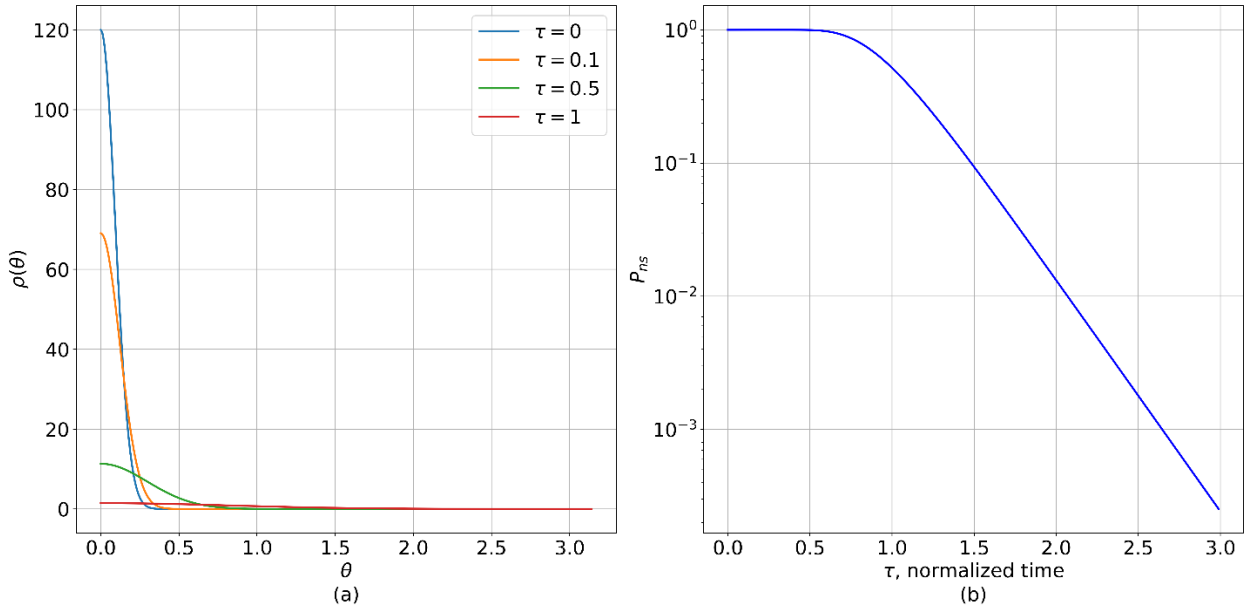
Figure 2.11: WER results from FP equation calculations. (a) PDF as at different normalized time steps. (b) Non-switching probability as a function of normalized time. More results are shown in later chapters.

The FP equation based method can calculate the WER at any time by solving the FP equation only once and achieve much higher accuracy then the straightforward statistical method. However, this method cannot be easily, and has not been, extended beyond the macrospin approximation, where non-uniform switching occurs.

Chapter 3

Eigenvalue-based micromagnetic analysis of switching in spin-torque-driven structures

The LLG equation (1.4) provides time dependent solutions for the magnetization dynamics for a general case. In some important cases, the magnetization dynamics occurs as a perturbation around the equilibrium state, such that the dynamics can be considered as linear. For example, when a magnetic structure is driven by a weak dynamic magnetic field, the system response is approximately linear. Another example is the initial switching dynamics in an MRAM element. Such initial dynamics is due to the fact that the spin torque overcomes the system damping, which results in initially weak oscillations of the magnetization around the equilibrium state, which also occurs in the linear regime. Once such precessions start, they grow in their magnitude, and eventually they become large, such that the system become non-linear and switching occurs. The initial dynamics is characterized by the precessional frequency, which is related to the ferromagnetic resonance at Larmor frequency [1], and more generally it is related to the resonant magnetic modes supported by the structure. The term resonant mode refers to an oscillation pattern where the system oscillates with a certain frequency, which is known as the resonant frequency. The resonant modes and frequencies are the eigenstates and eigenvalues of the system described by the linearized LLG (L-LLG) equation.

In ferromagnetic resonance experiments, the power absorbed by the magnetic system has peaks when the external AC magnetic field frequency is close to the resonant frequencies. The determination of the generic resonant modes is an important step in the study of microwave driven

magnetization dynamics. Much research has been done on the theoretical description of magnetization resonance phenomena. For example, Walker analyzed the case of saturated ellipsoidal particles where the exchange interaction is neglected [57]. Aharoni considered a case of saturated magnetic nanospheres in which the exchange interaction was prevalent with respect to magnetostatics [58], and Brown analyzed the case of an infinite cylinder [1]. More recently, resonant modes in micromagnetic systems were studied via micromagnetic formulations and simulations [59–61].

In this chapter, we show how to calculate these eigenstates and eigenfrequencies, and how to use them for the study of the switching behavior in spin-torque-driven structures. First, we introduce the eigenstates in magnetic structures. We discuss how to derive the eigenvalue problem of the system and construct the eigenvalue-based micromagnetic framework. Then, we show how this eigenvalue-based framework is used to study the spin-torque driven structures, and how to enable efficient and accurate calculations of the critical switching current.

3.1 Eigenstates in magnetic structures

In principle, there are two approaches to compute resonant states in micromagnetic structures, including the ringdown and eigenvalue problem methods. The idea of the ringdown method is to apply a short pulse to slightly perturb the system our of its equilibrium state and then calculate the time domain magnetization dynamics during the relaxation process. A discrete Fourier transform can compute the intensity of each frequency contribution to the relaxation oscillation and give a power spectrum. The peeks in the power spectrum correspond to the resonant frequencies. Once the resonant frequencies are determined, the Fourier coefficients belonging to these frequencies can be extracted and used to find the resonant modes. An example of this method is shown in Ref. [62], where the resonant frequencies of a thin permalloy film are calculated. The ringdown

method can be directly applied to any existing time domain LLG equation simulation framework, but it has several drawbacks. It is difficult to find all resonant modes because not all modes are coupled to a specific excitation. The ringdown method cannot distinguish the degenerate resonant modes because these modes contribute to the same peak in the power spectrum. The frequency resolution obtained by the ringdown method depends on the length of the relaxation phase, thus requiring potentially very long simulation times in order to obtain a fine resolution. Additionally, computing the imaginary part of the resonant frequency may be inaccurate as the overall response mixes multiple modes.

The eigenvalue method is developed to overcome these drawbacks. In the eigenvalue method, the LLG equation is first linearized around on the equilibrium state of the magnetic structure. It is proven rigorously that such a linearization is an accurate approximation to the full non-linear LLG equation [59]. The linearized LLG equation, when the external field is absent, can be viewed as an eigenvalue problem, and the eigenfrequencies and eigenstates to this eigenvalue problem are the resonant frequencies and modes of the system. We refer to the resonant frequencies and modes as to the eigenfrequencies and eigenstates in the rest of the dissertation. The eigenvalue method can precisely compute all eigenfrequencies and eigenstates of the system and it also solves the degeneracy issue so that it is generally preferred over the ringdown method. Figure 3.1 shows the results of first six eigenstates of a thin permalloy film from the eigenvalue method, where the degenerate states 2 and 3 are clearly distinguished. In the remaining parts of the chapter, we discuss how we build an eigenvalue framework that computes the eigenfrequencies and eigenstates and extends the framework to study the switching behavior in spin-torque driven structures.

| 8.130 | 10.327 | 10.382 | 12.426 | 13.672 | 13.763 | (GHz) |
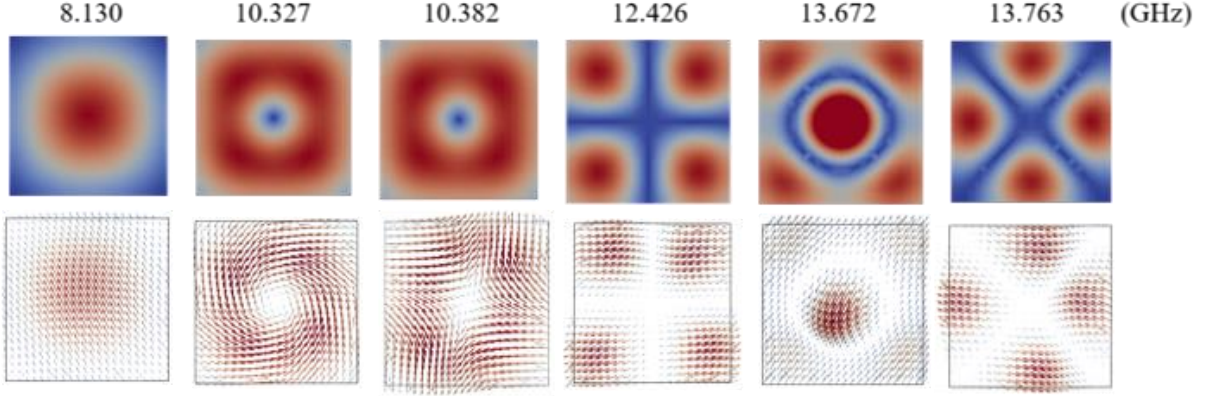
Figure 3.1: First six eigenfrequencies and states of a thin permalloy film from eigenvalue framework discussed below.

3.2 Eigenvalue-based micromagnetic framework

In this section, we present an eigenvalue framework (EVF) allowing for the study of switching properties in spintronic devices. We first derive the linearized LLG equation with effective fields including spintronic terms, which is the used to construct the EFV to find the eigenfrequency and corresponding eigenstate solutions to the system. We then invoke a perturbation theory to find the eigenfrequencies and eigenstates in the presence of spintronic excitations, allowing easily using the presented framework for cases with time dependent currents. These solutions are used to represent the LLG equation dynamic solutions as a sum over the damped or growing eigenstates modulated by time dependent coefficients for which simple equations are constructed.

3.2.1 Linearized LLG equation

To construct the EVF, the first step is to linearize the LLG around the equilibrium state. We start with the LLG equation with the spin torque term

$$\frac{\partial \mathbf{m}}{\partial t} = -\gamma' \mathbf{m} \times (\mathbf{H}_{eff}(\mathbf{m}) + \mathbf{H}_{st}(\mathbf{m})) - \alpha \gamma' \mathbf{m} \times \mathbf{m} \times (\mathbf{H}_{eff}(\mathbf{m}) + \mathbf{H}_{st}(\mathbf{m})), \qquad (3.1)$$

The effective field $\mathbf{H}_{eff}(\mathbf{m})$ excludes the ST field and it can be viewed as a linear function of $\mathbf{m}$

$$\mathbf{H}_{eff} = \mathbf{H}_{ms} + \mathbf{H}_{ex} + \mathbf{H}_{anis} = C\mathbf{m}. \tag{3.2}$$

The term $\mathbf{H}_{st}(\mathbf{m})$ is the spin transfer related field that using simplified models can be given by

$$\mathbf{H}_{st} = \beta\mathbf{m}\times\mathbf{p}, \tag{3.3}$$

where we exclude the field-like ST field assuming that its effect is insignificant for the magnetization switching. The spin-like torque can be included in the derivations in the same way as the damping torque. The ST parameter β can be written as $\beta = Jb$, where J is the electric current density and b is a coefficient related to the spintronic excitation. For STT, the coefficient $b = \eta\hbar_e/(2eM_s\delta)$, where δ is the effective thickness and the rest of the parameters are defined after (2.4) [24,25]. For SOT, $b = \mu_B\theta_{SH}/eM_s\delta$, where the parameters are defined after (2.5) [30,31]. Note that β and $\mathbf{p}$ can be functions of space and time.

To linearize the LLG equation (3.1), we denote the equilibrium state $\mathbf{m}_0$ for the system without an STT field. This equilibrium is given by the Brown condition [1]:

$$\mathbf{m}_0 \times \mathbf{H}_{eff}(\mathbf{m}_0) = 0, \tag{3.4}$$

which corresponds to $\partial\mathbf{m}_0/\partial t = 0$ when $\mathbf{H}_{st}$ is excluded in (3.1). The effect of the system excitation by spin torque can be considered as a perturbation from this equilibrium.

We seek a solution for small magnetization deviations $\mathbf{v}$ around the equilibrium state such that

$$\mathbf{m} = \mathbf{m}_0 + \mathbf{v}, \tag{3.5}$$

and $\mathbf{v}$ is normal to $\mathbf{m}_0$, so that the normalization of $\mathbf{m}$ is maintained. Because of the linearity of $\mathbf{H}_{eff}(\mathbf{m})$, we can write $\mathbf{H}_{eff}(\mathbf{m}) = \mathbf{H}_0 + C\mathbf{v}$, where $\mathbf{H}_0 = \mathbf{H}_{eff}(\mathbf{m}_0) = C\mathbf{m}_0$ is the effective field at the equilibrium state. Insert the expansion (3.5) into (3.1), assuming that the damping constant α

and spin-torque coefficient β are small, which is the case for materials for which spin-torque excitations are typically used, keeping only the first order terms that are linear in $\mathbf{v}$, α and β, we have the L-LLG

$$
\begin{aligned}
\frac{\partial \mathbf{v}}{\partial t} = &-\gamma \left[\mathbf{m}_0 \times \left(C\mathbf{v} + \beta \mathbf{v} \times \mathbf{p} \right) + \mathbf{v} \times \mathbf{H}_0 \right] \\
&- \alpha \gamma \mathbf{m}_0 \times \left[\mathbf{m}_0 \times \left(C\mathbf{v} + \beta \mathbf{v} \times \mathbf{p} \right) + \mathbf{v} \times \mathbf{H}_0 \right]. \\
&+ \gamma \beta \mathbf{m}_0 \times \mathbf{m}_0 \times \mathbf{p}
\end{aligned}
\tag{3.6}
$$

We can simplify the L-LLG (3.6) by using the cross-product operator Λ. Λ is defined as [59]

$$
\Lambda(\mathbf{v})\mathbf{w} = \mathbf{v} \times \mathbf{w}.
\tag{3.7}
$$

Using operator Λ, the L-LLG (3.6) can be written as the matrix form

$$
\begin{aligned}
\frac{\partial \mathbf{v}}{\partial t} = &-\gamma \left(\Lambda(\mathbf{m}_0)C\mathbf{v} - \beta\Lambda(\mathbf{m}_0)\Lambda(\mathbf{p})\mathbf{v} - \Lambda(\mathbf{H}_0)\mathbf{v} \right) \\
&- \alpha\gamma \left(\Lambda(\mathbf{m}_0)\Lambda(\mathbf{m}_0)C\mathbf{v} - \beta\Lambda(\mathbf{m}_0)\Lambda(\mathbf{m}_0)\Lambda(\mathbf{p})\mathbf{v} - \Lambda(\mathbf{m}_0)\Lambda(\mathbf{H}_0)\mathbf{v} \right). \\
&+ \gamma\Lambda(\mathbf{m}_0)\Lambda(\mathbf{m}_0)\mathbf{p}
\end{aligned}
\tag{3.8}
$$

In view of the linearized LLG equation (3.8), the first term in the right hand side is linear in $\mathbf{v}$ and it corresponds to the precessional torque of the effective field. The second term is also linear in $\mathbf{v}$ and it corresponds to the damping torque of the effective field and the linear component of the spin torque. The last term of (3.8) can be regarded as a forcing term corresponding to the STT torque, which is a term independent of $\mathbf{v}$. The magnetization dynamics via the linearized LLG equation can be solved numerically using standard finite difference or finite element methods [19]. The linearization carried out above is generally allowed when the magnetization varies only slightly from its equilibrium state. Weak magnetization variations can be due to weak excitations, e.g., by weak applied fields or by spin-torque. The variations are also weak in the initial stages of the magnetization dynamics near an equilibrium state even when the system is driven by strong spin torque. The initial dynamics contains important information about the system behavior and

can be used to study the micromagnetic systems, e.g. the strip line ferromagnetic resonance response in ferromagnetic films [63], and the switching behavior in spin-torque driven structures discussing below.

3.2.2 Eigenvalue problem formulation

We can set up the eigenvalue problem from linearized LLG equation (3.8) by ignoring the last term on the right hand side for now

$$A\varphi_n = j\omega_n\varphi_n, \tag{3.9}$$

where ω_n and φ_n are the n-th eigenfrequency and eigenstate of the system, respectively. The eigenfrequency ω_n comes from the time derivative $\partial\mathbf{v}/\partial t$ with the phasor notation

$$\mathbf{v}(\mathbf{r},t) = \mathrm{Re}\left\{\tilde{\mathbf{v}}(\mathbf{r})e^{j\omega t}\right\}, \tag{3.10}$$

where $j = \sqrt{-1}$ is the imaginary unit. The operator A is defined following (3.8)

$$A = \gamma\Lambda(\mathbf{m}_0)A_0 + \gamma\Lambda(\mathbf{m}_0)\left(\alpha\Lambda(\mathbf{m}_0)A_0 - \beta\Lambda(\mathbf{p})\right), \tag{3.11}$$

where

$$A_0 = \left((\mathbf{H}_0\cdot\mathbf{m}_0)I - C\right), \tag{3.12}$$

with the unit operator I [59,60]. Note that as discussed before, β can be time-dependent so that the eigenvalue problem (3.9) is defined at a particular time t.

Note that the small deviation $\mathbf{v}$ is normal to the equilibrium magnetization $\mathbf{m}_0$, and it only has non-zero component in the tangent space $TM(\mathbf{m}_0)$ [59]. In the tangent space $TM(\mathbf{m}_0)$, we denotes the unit vectors of spatial basis as $\{\mathbf{e}_1,\mathbf{e}_2,\mathbf{e}_3\}$ [59]

$$\mathbf{e}_3 = \mathbf{m}_0$$
$$\mathbf{e}_2 = \mathbf{e}_z \times \mathbf{m}_0 \, ,$$
$$\mathbf{e}_1 = \mathbf{e}_2 \times \mathbf{e}_3 \qquad (3.13)$$

where $\mathbf{e}_z$ is the unit basis vector in the original space.

Thus, the operator A is not full rank and has zero eigenvalues, which results in difficulties in solving the eigenvalue problem. To eliminate this problem, we can project the vectors of the eigenvalue problem into $TM(\mathbf{m}_0)$ using the projection operator $P_{\mathbf{m}_0}$ [59]

$$P_{\mathbf{m}_0} = (I - \mathbf{m}_0 \otimes \mathbf{m}_0) \, . \qquad (3.14)$$

Applying the projection operator $P_{\mathbf{m}_0}$ to eigenvalue problem (3.9)-(3.12), noting that in $TM(\mathbf{m}_0)$ the operator $\Lambda(\mathbf{m}_0)$ is linear, and anti-symmetric and invertible [59–61], i.e.,

$$\Lambda(\mathbf{m}_0)\Lambda(\mathbf{m}_0) = -I \, , \qquad (3.15)$$

we obtain the projected eigenvalue problem

$$A_\perp \varphi_n = j\omega_n \varphi_n \, , \qquad (3.16)$$

where

$$A_\perp = \gamma\Lambda(\mathbf{m}_0)A_{0\perp} + \gamma\left(-\alpha A_{0\perp} - \beta\Lambda_\perp(\mathbf{p})\right)$$
$$A_{0\perp} = P_{\mathbf{m}_0} A_{0\perp} ; \Lambda_\perp(\mathbf{p}) = P_{\mathbf{m}_0} \Lambda(\mathbf{p}) \qquad (3.17)$$

Solving the eigenvalue problem (3.16)-(3.17) gives the eigenfrequencies and eigenstates of the system.

3.2.3 Perturbation analysis

The eigenvalue problem (3.16) is time dependent because the term β can be time dependent. This indicates the eigenvalue problem needs to be solved at each time, which is computationally expensive. To present important properties of the eigen-solutions and provide a practical method for solving the time-dependent eigenvalue problem, we present a perturbation solution.

For the perturbation solution, we note that we consider small damping cases where $\alpha \ll 1$. We note that the parameter β of the spin torque terms is usually on the same order as α [26], i.e., the linear STT term is small as well. Therefore, we can carry out a perturbation theory in which we define the base eigenvalue problem:

$$\Lambda(\mathbf{m}_0)A_{0\perp}\bar{\varphi}_n = j\bar{\omega}_n\bar{\varphi}_n , \tag{3.18}$$

which has eigenfrequencies $\bar{\omega}_n$ and eigenstates $\bar{\varphi}_n$. The eigenfrequencies $\bar{\omega}_n$ can be shown to be purely real and the eigenstates $\bar{\varphi}_n$, when normalized, can be shown to satisfy the weighted orthonormality condition [59]

$$<\bar{\varphi}_n, A_{0\perp}\bar{\varphi}_{n'}>_\Omega = \frac{1}{V_\Omega}\int_c \bar{\varphi}_n^* A_{0\perp}\bar{\varphi}_{n'}dV = \delta_{nn'} , \tag{3.19}$$

where $<\cdot, \cdot>_\Omega$ is the inner product defined as the integral over the entire domain Ω of the magnetic structure, the asterisk denotes the complex conjugation, and $\delta_{nn'}$ is the Kronecker's symbol. The base eigenvalue problem (3.18) has operators contain only values related to the equilibrium state so that it is time independent. The eigen-states $\bar{\varphi}_n$ form an orthonormal basis that can be used to represent more general eigen-solutions and time domain solutions. We recognize that the operator $A_\perp$ in the eigenvalue problem (3.16) can be written as $A_\perp = \Lambda(\mathbf{m}_0)A_{0\perp} + \delta A$, where

$$\delta A = \gamma\Lambda(\mathbf{m}_0)\big(\alpha\Lambda(\mathbf{m}_0)A_{0\perp} - \beta\Lambda_\perp(\mathbf{p})\big) \tag{3.20}$$

is the perturbation operator that has a first order small term compared to the base operator $\Lambda(\mathbf{m}_0)A_0$. The eigenfrequencies and eigenstates of the original eigenvalue problem are obtained as $\omega_n = \bar{\omega}_n + \delta\omega_n$ and $\varphi_n = \bar{\varphi}_n + \delta\varphi_n$. Implementing the matrix perturbation analysis and keeping

only the linear terms in the perturbations of the operators and solutions, the perturbation to the eigenfrequency is given by

$$\delta\bar{\omega}_n = \bar{\omega}_n < \bar{\varphi}_n, \gamma\beta\Lambda_\perp(\mathbf{p})\bar{\varphi}_n > + j\alpha\bar{\omega}_n^{\,2} < \bar{\varphi}_n, \bar{\varphi}_n > . \tag{3.21}$$

Note that $\delta\omega_n$ is purely imaginary, which is due to the fact that $\bar{\omega}_n$ and $< \bar{\varphi}_n, \bar{\varphi}_n >$ are real, and the real and imaginary parts of the complex vectors $\gamma\beta\Lambda_\perp(\mathbf{p})\bar{\varphi}_n$ and $\bar{\varphi}_n$ are perpendicular to each other. As a result, we understand that the eigen-frequencies are complex, i.e.,

$$\omega_n = \omega_n' + j\omega_n'', \tag{3.22}$$

where $\omega_n' = \mathrm{Re}\{\omega_n\}$ and $\omega_n'' = \mathrm{Im}\{\omega_n\}$. In the perturbation approximation, $\omega_n' = \bar{\omega}_n$ and $\omega_n'' = j\delta\omega_n$. And the perturbation to the eigenstate is given by

$$
\begin{aligned}
\delta\bar{\varphi}_n &= \sum_m \varepsilon_{nm}\bar{\varphi}_n \\
\varepsilon_{nm} &= \frac{\bar{\omega}_m < \bar{\varphi}_n, (j\alpha\bar{\omega}_m I + \gamma\beta\Lambda_\perp(\mathbf{p}))\bar{\varphi}_m >_\Omega}{\bar{\omega}_n - \bar{\omega}_m}, m \neq n . \\
\varepsilon_{nn} &= \frac{1}{2} < \bar{\varphi}_n, (\gamma\beta\Lambda_\perp(\mathbf{p}) + j\alpha\bar{\omega}_n I)\bar{\varphi}_n >_\Omega
\end{aligned}
\tag{3.23}
$$

3.2.4 Time domain solutions based on the eigenvalue framework

The eigen solutions in the previous section can be used to represent the solutions of the time domain problem of (3.8). To that end, we write $\mathbf{v}$ as $\mathbf{v} = 2\mathrm{Re}\{\tilde{\mathbf{v}}\}$, where

$$\tilde{\mathbf{v}} \approx \sum_n a_n \bar{\varphi}_n , \tag{3.24}$$

is the time domain complex solution expressed approximately given in terms of the base eigenstates $\bar{\varphi}_n$, complex eigenfrequencies ω_n, and coefficients a_n determining the excitation of the eigenstates. The factor of 2 accounts for the fact that the two modes are symmetric in the positive and negative frequencies. The base eigenstates $\bar{\varphi}_n$ are used instead of the actual

eigenstates φ_n assuming that the differences between $\bar{\varphi}_n$ and φ_n are insignificant, which is the case under the assumption of small α. Similar approximations were used in related applications of eigenvalue based solutions in Micromagnetics [59,61] and other areas of physics, e.g., electromagnetics [64]. Using $\bar{\varphi}_n$ has important benefits due to the fact that $\bar{\varphi}_n$ are time independent and have the orthogonality property of (3.19).

Substituting the representation of (3.24) into (3.8), using the eigenvalue problem with the perturbation solutions of (3.21) and (3.23), using the orthogonality in (3.19), and performing a weighted inner product with $A_0\bar{\varphi}_n(\mathbf{r})$ in both sides of (3.24), we obtain the following set of independent time domain differential equations for a_n :

$$\frac{da_n}{dt} = j\omega_n a_n + P_n^{st} , \tag{3.25}$$

where

$$P_n^{st} = < \gamma\beta\Lambda(\mathbf{m}_0)\Lambda(\mathbf{m}_0)\mathbf{p}, A_0\bar{\varphi}_n > , \tag{3.26}$$

relates to the last term in the right hand side of (3.8). Solution for a_n can be given by analytically solving the ordinary differential equation (3.25)

$$a_n(t) = e^{\int_0^t j\omega_n(\tau)d\tau}\left[a_n(0) + \int_0^t e^{\int_0^\tau -j\omega_n(t')dt'} P_n^{st}(\tau)d\tau \right]. \tag{3.27}$$

Here, $a_n(0)$ is determined from the initial condition as $a_n(0) = < \tilde{\mathbf{v}}(t = 0), A_0\bar{\varphi}_n >$, where $\tilde{\mathbf{v}}(t = 0)$ is the initial complex small deviation magnetization state, and the integrals in the power exponentials appear because ω_n is generally a complex time dependent function. The solutions of (3.27) are valid for any time dependence of the current, including constant and pulsed currents. When the current is constant, the solution can be simplified to

$$a_n(t) = e^{-\omega_n'' t} e^{j\omega_n' t} \left(a_n(0) + \frac{P_n^{st}}{j\omega_n} \right) - \frac{P_n^{st}}{j\omega_n}.$$ (3.28)

3.3 Switching analysis in spin-torque-driven structures

The switching behavior in spintronics driven structures typically starts from one of the equilibrium states as small oscillations that increase in their magnitude to result in large oscillations, which are followed by the magnetization reversal to the other equilibrium state. Structures of a small size can be approximated by a single spin because the magnetization motion is mostly coherent in the macrospin approximation, switching properties, such as the switching current and time as well as the switching trajectory, can be obtained analytically. On the other hand, for larger structures, which are greater than the exchange or domain wall length, the magnetization dynamics is non-uniform so that obtaining switching parameters numerically can be complicated and non-reliable. For example, obtaining the critical switching current, viz. the current required for switching at infinite time, is accomplished by calculating the switching current at multiple switching times and extrapolating to infinite time assuming a linear dependence of the switching current versus the inverse time. However, while such an extrapolation is accurate and efficient for small structures, for which a single-spin approximation is valid, it may be inaccurate and slow for larger structures. Additionally, relying purely on brute-force numerical simulations does not provide a clear physical picture as to why a certain type of switching occurs and how it is related to the operational parameters.

In this section, we present how to use the EVF introduced in the previous section to study the switching properties in spin-torque driven devices. The EVF allows reliably obtaining the critical current density required for switching in spintronic devices as well as the switching current and switching time for pulsed current excitations. The EVF can be also extended to simulate the

magnetization dynamics in time domain with and without finite temperature. This method based on EVF provides understanding of the switching dynamics behavior for structures of small and large sizes, including cases with non-uniform dynamics. In the following sections, we demonstrate the eigenvalue framework by considering switching in an STT-MRAM cell, comprised of a cylindrical free layer of 1 nm thickness and two diameters of 20 nm and 80 nm with $M_s = 960\,\text{emu/cm}^3$, $A_{ex} = 1\,\mu\text{erg/cm}$, damping factor $\alpha = 0.01$, and uniaxial anisotropy $K_U = 6.11\,\text{Merg/cm}^3$ with easy axis perpendicular to disc.

3.3.1 Eigenstates of spin-torque-driven structures

We first solve the base eigenvalue problem (3.18) for $\bar{\omega}_n$ and $\bar{\varphi}_n$. Figure 3.2 shows the first six eigenstates of an 80 nm diameter free layer of a perpendicular MTJ. We find that the first eigenstate has a more uniform distribution with the maximum in the middle. The rest of the modes have a more non-uniform distribution with maxima and minima modulation. The eigenstates can be classified according to the winding numbers [65]. Here, the first six modes

have winding numbers of 0, 1, -1, 2, -2, 1, respectively. We also calculated the eigenstates of a smaller, 20 nm diameter, MRAM cell, and found that its eigenstates have an almost the same spatial distribution. On the other hand, the eigenfrequencies of the 80 nm and 20 nm cells

are different. The eigenfrequencies of the 20 nm cell are higher and have a much greater separation for different n. Table 3.1 provides the corresponding eigenfrequencies with for 20 nm and 80 nm diameter cases.
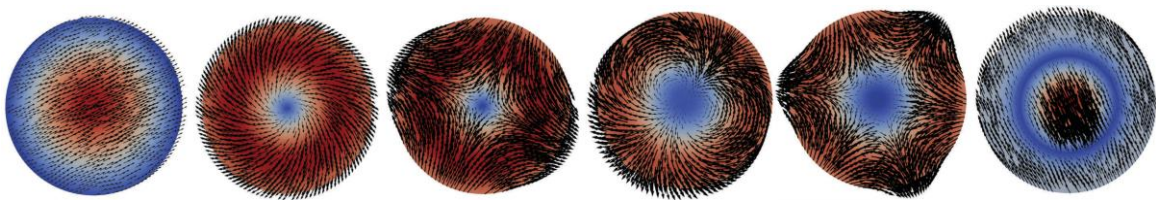
Figure 3.2: First six eigenfrequencies and modes for 80nm MRAM free layer disc.

Table 3.1: Eigenvalue framework parameters: eigenstate no n, $f_n' = \omega_n'/(2\pi)$, J_{cn} and P_n^{ST} calculated with $J = J_{c1}$ and scaled with $|\varphi_n|_{max}/\omega_n'$ to make it unitless and related to the magnetization values.

D (nm)	n	f_n' (GHz)	J_{cn} (MA/cm^2)	$\|P_n^{ST}\varphi_n/\omega_n'\|_{max}$
20	1	8.13	0.85	7.57e-7
	2	29.17	3.10	3.94e-7
	3	29.81	3.11	1.99e-7
	4	65.55	6.82	7.61e-7
	5	65.61	6.83	1.03e-7
	6	94.18	9.93	2.78e-8
80	1	3.76	0.39	1.01e-6
	2	5.80	0.60	1.08e-6
	3	5.86	0.61	8.12e-8
	4	8.63	0.90	9.14e-8
	5	8.70	0.91	7.17e-8
	6	9.93	1.04	1.30e-7

3.3.2 Critical current prediction

From the perturbation analysis in the previous section, it can be shown that when the spin currant density $J = 0$, i.e., $\beta = 0$, $\omega_n'' > 0$ for $\alpha > 0$. For $J < 0$, i.e., $\beta < 0$, ω_n'' has an even greater positive value. For $J > 0$, i.e., for $\beta > 0$, the positive value of ω_n'' decreases and there is a certain critical value of J_{cn} for which $\omega_n'' = 0$. At values $J > J_{cn}$, $\omega_n'' < 0$, which corresponds to increasing precessional amplitude for the eigenstate φ_n. Therefore, we can use the condition $\omega_n'' = 0$ to calculate the critical current density J_{cn} for n-th eigenstate. Let $\omega_n'' = 0$ in (3.21) we have

$$J_{cn} = \frac{-j\alpha\bar{\omega}_n <\bar{\varphi}_n, \bar{\varphi}_n>}{\gamma b <\bar{\varphi}_n, \Lambda_\perp(\mathbf{p})\bar{\varphi}_n>}, \tag{3.29}$$

and the overall critical current density J_c is defined as $J_c = \min_n\{J_{cn}\}$ obtained for the eigenstate number n_c. At $J = J_c$, $\omega_{n_c}'' = 0$, so that the STT effects overcomes the effect of the system damping, and any $J > J_c$ lead to increased oscillations and switching. Compared to the

48

conventional method calculating critical current by extracting from multiple time domain simulations [32], (3.29) solves J_{cn} directly from the eigenfrequency and eigenstate. Also with (3.19), (3.21) and (3.29), ω_n'' can be expressed as a function of applied current density J:

$$\omega_n'' = -\alpha\omega_n'\left(\frac{J}{J_{cn}} - 1\right).$$

(3.30)

We show the calculated the critical current density J_{cn} for first six eigenstates for 20 nm and 80 nm cases in Table 3.1. The results are consistent with high accuracy time domain extraction results. To understand the excitation of different eigenstates and the overall time dynamics, Figure 3.2 shows ω_n'' for n = 1, 2, 3,4, 5, 6 as a function of J for 20 nm and 80 nm cells. When $J > J_{c1}$ but smaller than the rest of critical currents, only $\omega_1'' < 0$, whereas the rest $\omega_n'' > 0$. As a result, only the n = 1 eigenstate is important for the time dynamics. On the other hand, for large J, all $\omega_n'' < 0$ and they are close to each other. This behavior can be explained by This behavior can be explained by noting that for large J, $\omega_n'' \approx -\alpha J/k_n$, as shown in (3.30), so that assuming that k_n is close for different n, ω_n'' is also approximately the same for different n. As a result, many eigenstates become important to describe the time dynamics.

3.3.3 Switching time prediction

The presented theory provides not only the critical current density J but also an approximation for the switching current density for a given time or stitching time for a given current density $J > J_c$. To that end, we can set a condition on $|a_n|$ in (3.24) to be at a certain level $|a_n|_{\max}$ to lead to switching. This can be set by requiring that $|a_n\bar{\varphi}_n| = C$, where C is a constant of $O(1)$. Then, assuming constant current, using (3.28) and (3.29), we can obtain the conditions for the switching

current J_{sw} for a given pulse duration τ and switching time t_{sw} for switching time for a given current $J > J_c$:

$$\frac{J_{sw}}{J_c} = 1 + \frac{\log(\xi)}{\alpha \omega_c' \tau}; t_{sw} = \frac{\log(\xi)}{\alpha \omega_c' (J/J_c - 1)},$$ (3.31)

where $\xi \approx \zeta / \left(|\bar{\varphi}_{nc}|_{\max} | a_{n_c}(0) + P_{n_c}^{st} / j\omega_{n_c} | \right)$ is the coefficient related to the initial magnetization conditions and the driving term. For zero-temperature simulations starting from equilibrium, $a_{n_c}(0) = 0$ and ξ is determined by $P_{n_c}^{st}$.
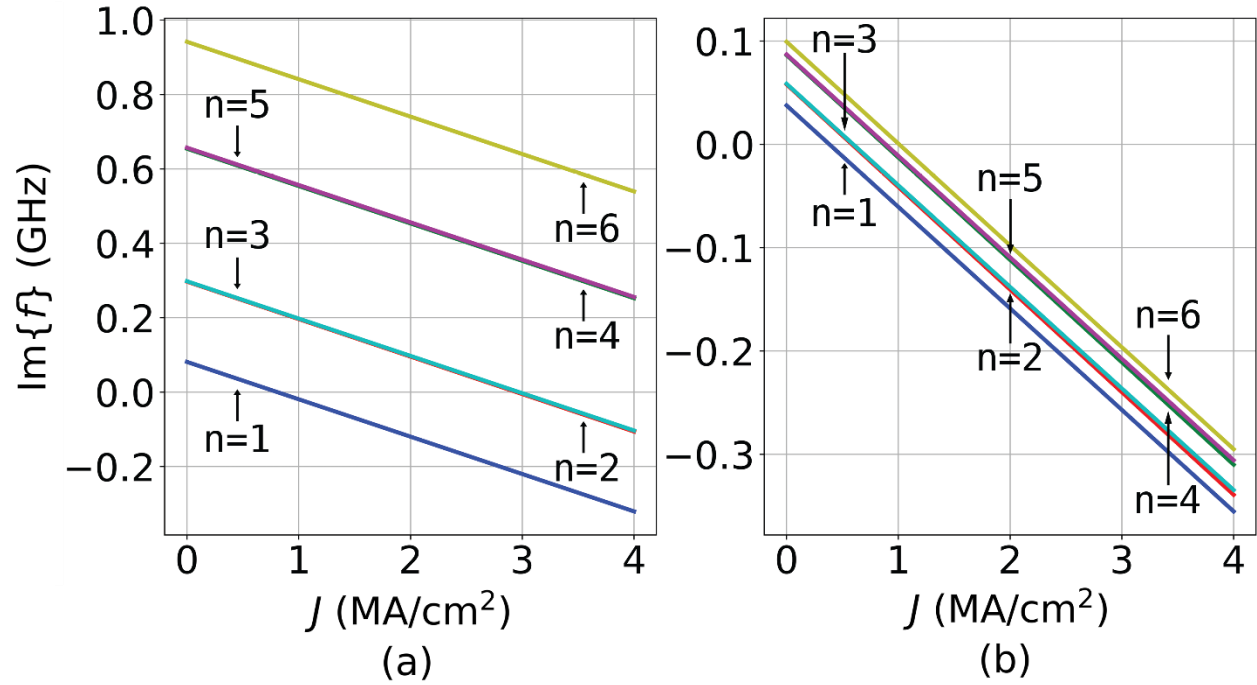
Figure 3.3: Imaginary eigenfrequencies ω_n'' vs. current J for the first 6 eigenstates for (a) $D = 20$ nm and (b) $D = 80$ nm disc.

Figure 3.3 shows J_{sw} as a function of $1/\tau$ obtained via the eigenvalue framework analysis and via the complete LLG equation solver. In the LLG equation simulations, switching is defined as the average perpendicular magnetization crossing zero. In EVF, the results were obtained via

50
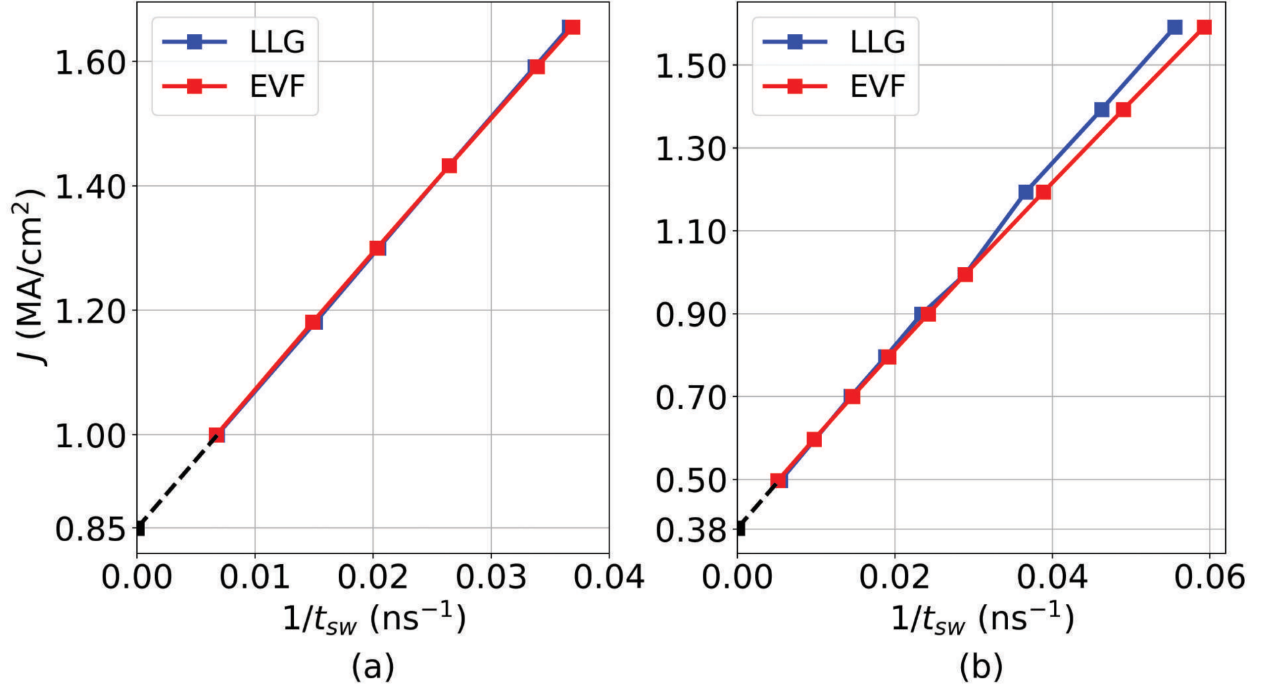
Figure 3.4: Inverse of switching time with different current densities for (a) $D = 20\,\mathrm{nm}$ and (b) $D = 80$ nm disc. Black dash lines show linear extrapolation of 5 points with smallest current of LLG equation simulations and the intercept is the predicted J_c.

(3.31), where ζ was chosen such that curve of J vs. $1/\tau_{sw}$ obtained for $J > J_c$ is accurately extrapolated to J_c at $1/\tau_{sw} = 0$, and the corresponding P_n^{st} values of the first six eigenstates are shown in Table 3.1. This choice resulted in $\zeta = 1.08$ and $\zeta = 1.32$ for 20 nm and 80 nm disc., respectively. The initial magnetization conditions for both eigenvalue framework and LLG equation simulations were the same equilibrium state, i.e., for eigenvalue framework $\tilde{\mathbf{v}}(t = 0) = 0$ and $a_n(0) = <\tilde{\mathbf{v}}(t = 0), A_0\bar{\varphi}_n> = 0$. The results obtained via the eigenvalue framework and LLG equation approaches are close to each other. The curve obtained via the LLG equation solver is linear for the 20 nm case, but it is not linear for the 80 nm case. For the 80 nm case, the curve has different curvatures for larger and small $1/\tau$. The values of J_c are typically obtained by linearly extrapolating from the J_{sw} vs. $1/\tau$ curve such that $J_c = J_{sw}(1/\tau = 0)$. The non-linearity of the

J_{sw} vs. $1/\tau$ curve, therefore, poses a significant problem in terms of the reliability and speed of calculating J_c. Indeed, one needs to run simulations for a large τ to obtain more reliable results, which is slow, and it is not clear a priori what values of τ are required. The eigenvalue framework, on the other hand, allows obtaining the results by simply obtaining a solution to a single eigenproblem problem followed by the perturbation theory analysis for the results in Table 3.1.

3.3.4 Magnetization dynamics simulation

Besides predicting the switching time directly from (3.31), the detailed magnetization dynamics can also be calculated from the eigenvalue framework using (3.24) and (3.27). We demonstrate the time domain dynamics using the eigenvalue framework and the LLG equation solver for the 20 nm and 80 nm cells for two values of $JD = 20\,\text{nm}$ in Figure 3.4. The eigenvalue framework results are shown for the overall solution $\mathbf{v}$ and for scaled a_n corresponding to individual eigenstates. The LLG equation results are shown for the magnitude of the spatially averaged transverse magnetization component $\mathbf{m}_r = \mathbf{m} - \left(\mathbf{m}\cdot\mathbf{m}_0\right)\mathbf{m}_0$ equivalent to $\mathbf{v}$ in eigenvalue framework. The results are shown for the magnitude of the averages $|<\mathbf{m}_r>|$ and $|<\mathbf{v}>|$, which represent a more global characterization, e.g., related to magnetoresistance that would be obtained if a read layer .were added to the stack, as well as the average of the magnitudes $<|\mathbf{m}_r|>$ and $<|\mathbf{v}|>$, which represent more local behavior of the magnetization. The initial magnetization conditions for both eigenvalue framework and LLG equation simulations were the same equilibrium state, as in Figure 3.3. For eigenvalue framework, we stopped the simulation when $|<\mathbf{v}>|=1$, which is the physically maximal possible value. For the 20 nm cell (Figure 3.4 (a, b, e, f)), the EVF results for $<|\mathbf{v}|>$ and $|<\mathbf{v}>|$ are close to the LLG equation results $<|\mathbf{m}_r|>$ and $|<\mathbf{m}_r>|$ for all times until switching occurs. The increase of $|\mathbf{v}|$ is exponential and the increase

rate is directly given by ω_1''. This behavior is explained by the fact that for the 20 nm cell with $J = 1.5 J_{c1}$, $J > J_{c1}$ but $J < J_{cn}$ with $n > 1$ (see Table 3.1), i.e., only $n = 1$ eigenstate is growing with $\omega_1'' < 0$, whereas all other eigenstates are damped $\omega_n'' > 0$ (Figure. 3.4(i, j)). For the 20 nm cell with $J = 10 J_{c1}$, $J > J_{cn}$ and $\omega_n'' < 0$ for $n < 6$, but ω_1'' is significantly more negative, such that the $n = 1$ eigenstate is still dominant. For the 80 nm cell, the behavior is similar for the smaller J (Figure 3.4(c, g, k)), which has the same explanation as the cases for the 20 nm cell. The behavior of $\mathbf{m}_r$ after switching starts is more complicated because switching for the 20 nm cells is mostly by uniform rotation and for 80 nm cells it is by domain wall. For greater J for the 80 nm cells (Figure 3.4(d)), the time dependence of $|<\mathbf{m}_r>|$ and $|<\mathbf{v}>|$ still appears to be mostly as an exponential increase. On the other hand, the time dependence of $<|\mathbf{m}_r|>$ and $<|\mathbf{v}|>$ (Figure 3.4(h)) is not just an exponential increase but rather it is modulated with oscillations. The agreement between the eigenvalue and LLG equation solver frameworks is still good for times until switching starts. The oscillatory behavior in Figure 3.4 (h) is explained by the fact that multiple eigenstates become growing, and their coupling needs to be accounted for. Specifically, from Figure 3.4(l) and Table 3.1, the $n = 2$ eigenstate has a significant contribution. Because of the $n = 2$ eigenstate symmetry, this contribution is not revealed in the $|<\mathbf{m}_r>|$ and $|<\mathbf{v}>|$, but it leads to the oscillations in $<|\mathbf{m}_r|>$ and $<|\mathbf{v}|>$.

Additionally, for large amplitudes of m_r, the dynamics obtained via the general LLG equation solver becomes highly non-linear, e.g., the final switching may be via domain walls. Still, EVF predicts the initial dynamics and onset of switching accurately even for such large cells.

53
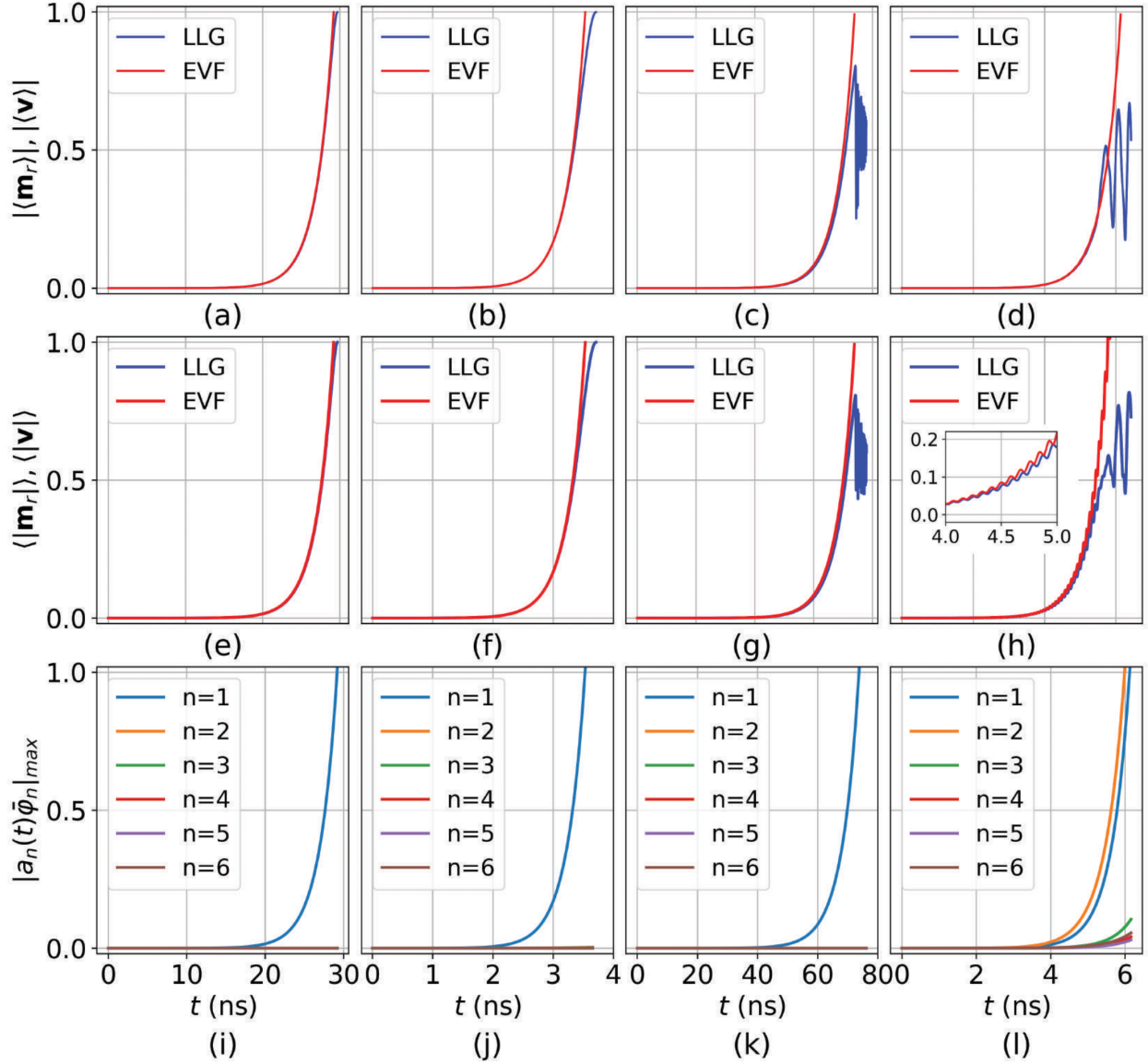
Figure 3.5: Time dependence of the magnetization behavior for different D and different values of constant and uniform J. (a-d) Magnitude of the averaged $|<\mathbf{m}_r>|$ and $|<\mathbf{v}>|$; (e-h) Average of the magnitude of $<|\mathbf{m}_r|>$ and $<|\mathbf{v}|>$; (i-l) Magnitudes of the averaged $|<\mathbf{v}_n>|$. The results are given for (a, e, i) $D=80\,\text{nm}$ $D=20\,\text{nm}$ with $J=1.5J_c$; (b, f, j) $D=20\,\text{nm}$ with $J=10J_c$; (c, g, k) with $J=1.5J_c$; (d, h, l) with $J=10J_c$. The inset in (h) presents a zoom in showing the magnetization oscillations appearing due to the excitation of multiple eigenstates.

3.4 Summary

In summary, we presented a theoretical and numerical framework for studying the switching properties of nanomagnetic structures driven by spintronic excitations. The framework considers

a linearized LLG equation for the small magnetization deviations from the equilibrium state. It expands the small magnetization deviations in terms of eigenstates with corresponding complex eigenfrequencies. Depending on the current driving spin torque, the eigenfrequencies can have a positive or negative imaginary part corresponding to damped or growing time domain solutions, respectively. The system time dynamics is then driven by a small number of growing eigenstates and for small currents just a single eigenstate may be sufficient. We developed a perturbation theory that provides semi-analytical dynamic solutions by using the base eigenvalue solutions, i.e., eigenvalue problem solutions with no current or damping. The framework allows obtaining accurate predictions of the switching properties, including the critical switching current, switching time for a given current and switching current for a given time. The critical switching current is obtained as the smallest current leading to vanishing imaginary part of the eigenfrequencies. The switching time and switching current can be obtained based on the values of the imaginary part of the eigenfrequencies. The presented eigenvalue framework can also be extended to account for thermal effects, which will be discussed later. The approach provides important insights into dynamics in such systems and allows solving several difficulties in their modeling, such extracting the switching current in MRAM and understanding reasons for switching mechanisms. The introduced framework is intended for applications in design and modeling of spintronic devices and understanding physics of their switching mechanisms.

Acknowledgements

Chapter 4

Switching Current Reduction in MRAM

In Chapter 3, we discussed how to predict the critical current of spin-torque driven MRAMs based on the eigenvalue framework. It was shown that the critical current of each eigenstate is determined by the eigenfrequency and the eigenstate spatial distribution. We showed with the uniform current density through the MTJs, the overall critical current always corresponds to the first eigenstate. This is because of the first eigenstate smallest eigenfrequency and the weighted orthogonality of the eigenstates. This could be changed if the spin current has a non-uniform spatial distribution passing through the MTJs. We present a method in which the current density and the material magnetic parameters are allowed to be spatial distributions. Such optimizations results in a lower critical current and higher efficiency of MRAM. First, we introduce the optimization of the current density based on the eigenvalue framework and using the projected gradient descent (PGD) method. We show how the optimization achieves, first, lower critical current for each eigenstate and, therefore, the overall critical current, second how the higher eigenstate is excited over the first eigenstate, and last, how the optimization increases the switching efficiency, viz. the ratio between the energy barrier and the critical current. We also show that such optimization, comparing to the decrease of the efficiency as an inverse of the MTJ size for the uniform current density, can achieve an approximately linear growth of the critical current and switching efficiency with the lateral size.

4.1 Non-uniform current density optimization

Consider that the current flowing through the MTJs is allowed to have a spatial density distribution, as illustrated in Figure 4.1, we denote the spin current density spatial distribution $J(\mathbf{r})$ as

$$J(\mathbf{r}) = J_{max}\psi(\mathbf{r}) , \tag{4.1}$$

57

where J_{max} is the maximal value of the current density and $\psi(\mathbf{r}) \geq 0$ is the normalized real-valued spatial distribution with respect to the spatial coordinate $\mathbf{r}$. The total current I is then given by

$$I = J_{max} \int_S \psi(\mathbf{r}) ds, \tag{4.2}$$

where the surface integral is over the cross-sectional area of the MTJ stack. Using the spatial distribution expression (4.1), the spin torque coefficient β is also a spatial function $\beta(\mathbf{r})$ defined by

$$\beta(\mathbf{r}) = bJ(\mathbf{r}). \tag{4.3}$$
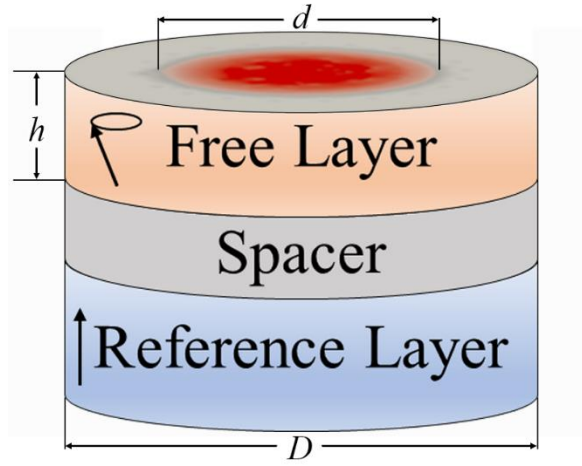
Figure 4.1: Illustration to the considered MTJ stack with non-uniform current distribution.

Using (4.3), following the similar procedure in the eigenvalue framework discussed in 3.3.2, the critical current density for eigenstate n is given by

$$J_{cn}(\mathbf{r}) = \frac{-j\alpha\bar{\omega}_n <\bar{\varphi}_n, \bar{\varphi}_n>}{\gamma b <\bar{\varphi}_n, \psi(\mathbf{r})\Lambda_\perp(\mathbf{p})\bar{\varphi}_n>} \psi(\mathbf{r}), \tag{4.4}$$

and inserting (4.4) into (4.2), the corresponding critical current is

$$I_{cn} = \frac{-j\alpha\bar{\omega}_n <\bar{\varphi}_n, \bar{\varphi}_n>}{\gamma b <\bar{\varphi}_n, \psi(\mathbf{r})\Lambda_\perp(\mathbf{p})\bar{\varphi}_n>} \int_S \psi(\mathbf{r}) ds. \tag{4.5}$$
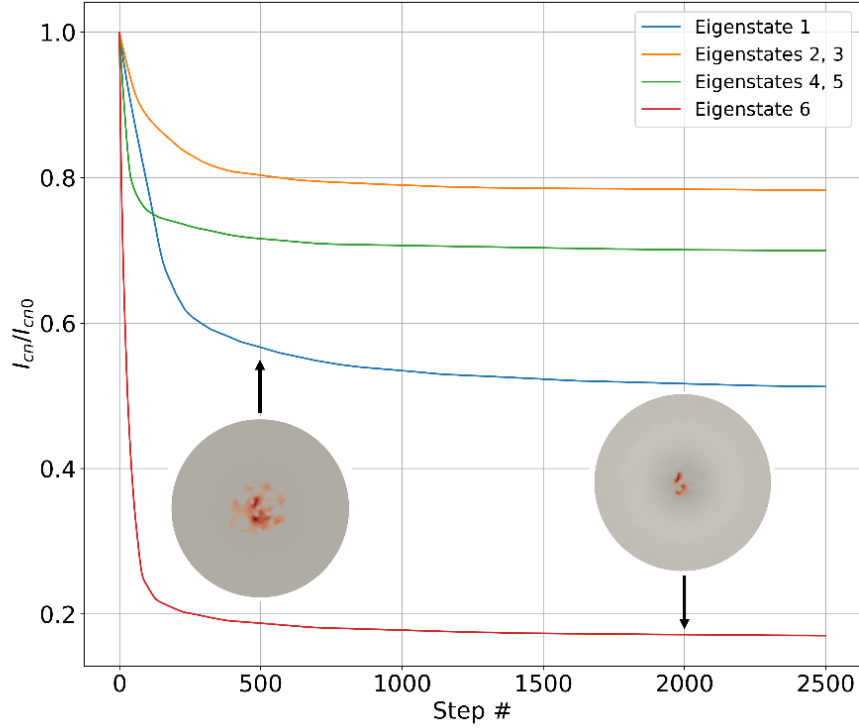
Figure 4.2: PGD optimization process for first 6 eigenstates for $D = 80\,\mathrm{nm}$. The curves for the sets of eigenstates $n = 2, 3$ and $n = 4, 5$ almost overlap, so that they cannot be visually distinguished.

In view of (4.5), I_{cn} can be regarded as a functional of $\psi(\mathbf{r})$. We can minimize the functional to find the optimal current density distribution $\tilde{\psi}_n(\mathbf{r})$ for a given n that leads to the minimum critical current $\tilde{I}_{cn}$. An approach that we follow is PGD [66], which finds $\tilde{\psi}_n(\mathbf{r})$ by the following iterative procedure

$$\psi_{i+1}(\mathbf{r}) = P\left[\psi_i(\mathbf{r}) - \lambda \nabla_{\psi_i} I_{cn}(\psi_i(\mathbf{r}))\right], \tag{4.6}$$

where λ is the hyperparameter learning rate and i is the minimization step number, the notation $\nabla_\psi I_{cn}(\psi(\mathbf{r})) = \partial I_{cn}/\partial \psi(\mathbf{r})$ denotes the gradient of the critical current I_{cn} given by (4.5) with respect to the distribution $\psi(\mathbf{r})$:

$$\nabla_{\psi} I_{cn}\left(\psi_n(\mathbf{r})\right) = \frac{-j\alpha\bar{\omega}_n <\bar{\varphi}_n, \bar{\varphi}_n>}{\gamma b\left(<\bar{\varphi}_n, \psi_n(\mathbf{r})\Lambda_{\perp}(\mathbf{p})\bar{\varphi}_n>\right)^2} \times$$

$$\left[\begin{array}{c} <\bar{\varphi}_n, \psi_n(\mathbf{r})\Lambda_{\perp}(\mathbf{p})\bar{\varphi}_n> S(\mathbf{r}) \\ - <\bar{\varphi}_n, \Lambda_{\perp}(\mathbf{p})\bar{\varphi}_n><\psi_n(\mathbf{r}), S(\mathbf{r})>\psi_n(\mathbf{r}) \end{array}\right],$$

(4.7)

where P denotes the projection operator of the optimization given the constraint $\psi_n(\mathbf{r}) \geq 0$,

$$P\left[\psi_n(\mathbf{r})\right] = \arg\min_{\psi(\mathbf{r})\geq 0} \|\psi - \psi_n\|_2 = \begin{cases} \psi_n(\mathbf{r}), & \text{if } \psi_n(\mathbf{r}) \geq 0 \\ 0, & \text{else} \end{cases}.$$

(4.8)

We can initialize with a uniform distribution and carry out PGD iteratively by combining (4.5)-(4.8) until I_{cn} is converged to $\tilde{I}_{cn}$, and the overall optimized critical current $\tilde{I}_c$ is then found by

$\tilde{I}_c = \min_n \{\tilde{I}_{cn}\}$.

We will carry out the optimization method descried above in the following sections. For the results, we consider an MTJ with the free layer of thickness $h = 1\,\text{nm}$, diameters D in the range of $20-160\,\text{nm}$, $\alpha = 0.01$, saturation magnetization $M_s = 960\,\text{emu/cm}^3$, exchange constant $A_{ex} = 10^{-6}\,\text{erg/cm}$, and uniaxial anisotropy energy density $K_U = 6.11\,\text{Merg/cm}^3$. The magnetization of reference layer is considered to be fixed to direction $\mathbf{p}$. For all the calculations, the eigenvalues and eigenstates were found using the FastMag micromagnetic simulator [19]. The tetrahedral mesh edge length was chosen $< 3\,\text{nm}$ to insure convergence. The numerical eigenvalue problem was solved with an iterative implicitly restarted and preconditioned Arnoldi method [67]. The time integration in the LLG equation solver was accomplished using a time step and order adaptive implicit solver based on the backward differentiation formulars [68,69] with the relative tolerance of 10^{-6}, which resulted in time steps of 0.1-1 ps. The time domain solutions corresponding to the eigenproblem were found via (3.24). The minimal energy paths and the corresponding energy barriers were found by using the nudged elastic band method, implemented

as a FastMag module.
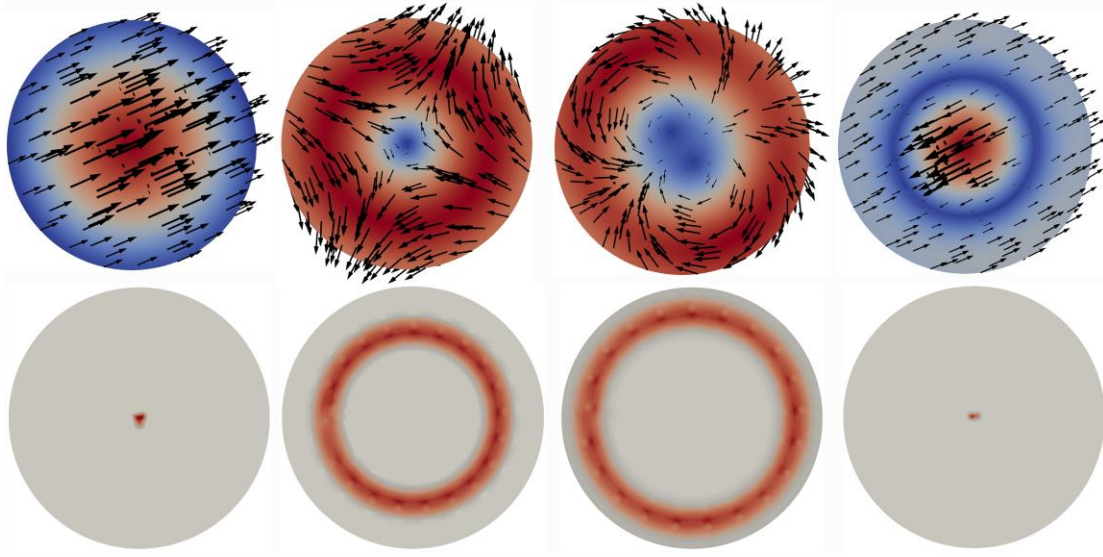
Figure 4.3: Top row shows eigenstates 1, 3, 4, 6 for $D = 80\,\mathrm{nm}$, where the color plot represents the spatial distribution of the magnitude, and the arrow plot represents the real part of the eigenstate. The bottom row shows the PGD optimized current distribution for each eigenstate.

4.2 Critical current with optimization

We first carry out the optimization for the first six eigenstates starting from a uniform distribution initialization. Figure 4.2 shows the convergence of the minimization process together with the magnetization snapshots at different minimization iterations. It is evident that the convergence is achieved with a few tens of iterations.

In Figure 4.3, we show the optimal current density distributions $\tilde{\psi}_n$ for most representative eigenstates $n = 1, 3, 4, 6$ for $D = 80\,\mathrm{nm}$ and they are similar for other sizes. The corresponding minimized $\tilde{I}_{cn}$ are shown in Table 4.1 for $D = 40\,\mathrm{nm}$ and $D = 80\,\mathrm{nm}$. For comparison, Table 4.1 also shows I_{cn} corresponding to the uniform current distribution $\psi = 1$. For the uniform ψ, I_{cn} increases with n, which can be explained by (4.5) and the fact that $\bar{\omega}_n$ increases with n. As a

result, $I_c = I_{c1}$, i.e., it corresponds to the smallest eigenfrequency. The optimized distributions in

Figure 4.3 are such that the stronger current density regions correspond to higher magnitude of the

eigenstate spatial distributions, which is due to the fact that, from (4.5), the optimal distribution is

weighted by the magnitude of the eigenstates. In all cases, $\tilde{I}_{cn} < I_{cn}$. The achievable reduction of

$\tilde{I}_{cn}$ as compared to I_c as well as the behavior of $\tilde{I}_{cn}$ for different n depends on the MTJ lateral

size. For the smaller $D = 40\,\text{nm}$, the $I_c/\tilde{I}_c$. ratio is 1.5, whereas for $D = 80\,\text{nm}$, the $I_c/\tilde{I}_c$ ratio

achieved a greater value of 2.3. for greater D, the ratio $I_c/\tilde{I}_c$ increases further. For $D = 40\,\text{nm}$,

$\tilde{I}_c = \tilde{I}_{c1}$, i.e., the best minimization is achieved for the $n = 1$ eigenstate, which is related to the fact

that ω_6' is significantly greater than ω_1'. On the other hand, for $D = 80\,\text{nm}$, $\tilde{I}_c = \tilde{I}_{c6}$, i.e., the best

minimization is achieved for the $n = 6$ eigenstate, which means that the switching process in this

case proceeds completely differently from what is conventionally assumed. The fact that $\tilde{I}_c = \tilde{I}_{c6}$

for $D = 80\,\text{nm}$ is because ω_6' is not significantly different than ω_1' and because φ_6 is more

confined to the center, thus allowing for a deeper minimization for $\tilde{\psi}_6$ than for $\tilde{\psi}_1$.

Table 4.1: Eigenfrequencies and critical currents for $D = 40\,\text{nm}$ and $D = 80\,\text{nm}$ for uniform, optimal, and confined current density distributions.

D (nm)	n	f (GHz)	I_{cn} (μA)	$\tilde{I}_{cn}$ (μA)	I_{cn}^{10} (μA)	I_{cn}^{20} (μA)
40	1	5.68	7.43	5.15	5.23	5.62
	2	12.0	15.8	12.1	102	31.3
	3	12.1	15.9	12.2	101	31.2
	4	21.7	28.4	17.6	189e3	141
	5	21.8	28.5	17.7	153e3	140
	6	27.9	36.6	5.95	7.74	15.8
80	1	3.76	19.7	9.84	10.0	10.4
	2	5.80	30.6	23.8	525	144
	3	5.86	30.7	23.9	520	143
	4	8.63	45.5	31.6	4.89e3	3.01e3
	5	8.70	45.6	31.7	2.46e3	1.85e3
	6	9.92	52.3	8.66	9.14	11.3

From Figure 4.3, we find that the optimal distribution is either $\tilde{\psi}_1$ or $\tilde{\psi}_6$, and thus $\tilde{\psi}$ for different sizes are nearly the same and they are mostly confined to the center. It may be hard to achieve such distributions practically. An alternative is to have a uniform distribution confined to a circular region of radius $d \leq D$, i.e., $\psi = 1$ for radii of $r \leq d$, and $\psi = 0$, otherwise. We used such confined distributions for $d = 10\,\text{nm}$ and $20\,\text{nm}$, and found that, as summarized in Table 4.1, while the obtained values of the critical current, referred to as $\tilde{I}_c^{10}$ and $\tilde{I}_c^{20}$ for $d = 10\,\text{nm}$ and $20\,\text{nm}$, respectively, are greater than the minimized $\tilde{I}_c$, the increase is only in the range of 10% for any D. For $D = 40\,\text{nm}$ and $D = 80\,\text{nm}$, $\tilde{I}_c^{10}$ and $\tilde{I}_c^{20}$ are obtained for the $n = 1$ and $n = 6$ eigenstates, respectively, which is the same behavior as that for the optimal current density distributions. On the other hand, for the rest of the shown n, the values of $\tilde{I}_{cn}$ are much greater than those for the corresponding optimal distributions, which is because these confined distributions for not match the corresponding eigenstates.

4.3 Magnetization dynamics with optimization

To relate the results for the critical current to the magnetization dynamics and switching, Figure 4.4 shows the time evolution of the magnetization for the confined current distribution with $d = 10\,\text{nm}$, two MTJ diameters $D = 40\,\text{nm}$ and $80\,\text{nm}$, and corresponding $I = 1.5\tilde{I}_c^{10}$. The polarization direction is tilted with a small angle of $0.1°$ with respect to the perpendicular direction, i.e., $\mathbf{p} = \left(0, \sin(\pi/1800), \cos(\pi/1800)\right)$. The small tilt in $\mathbf{p}$ is set to break the symmetry. The results were computed by solving the original LLG equation and via the eigenvalue framework converted into the time domain via (3.24). The results based on LLG equation are shown for the spatially averaged transverse magnetization component $\mathbf{m}_r = \mathbf{m} - (\mathbf{m} \cdot \mathbf{m}_0)\mathbf{m}_0$,

which is a counterpart of $\mathbf{v}$ obtained via the eigenvalue framework. From Table 4.1, the main contributions to the time dynamics are expected from the eigenstates with $n=1$ and 6. To demonstrate the role of these eigenstates, we show not only the dynamics of $\mathbf{v}$ but also the individual dynamics of $\mathbf{v}_1$ and $\mathbf{v}_6$, viz. the contribution to $\mathbf{v}$ from eigenstates $n=1$ and 6 respectively. For both $D=40\,\mathrm{nm}$ and $80\,\mathrm{nm}$, we find that, for early times, the micromagnetic and eigenvalue framework results match providing a great characterization of the switching onset. Once the magnetization starts switching non-linear effects, such as domain wall motion, become important and the micromagnetic results become different. For $D=40\,\mathrm{nm}$, the switching process is dominated by $\mathbf{v}_1$. This is explained by the fact that $\tilde{I}_c^{10}=\tilde{I}_{c1}^{10}$ and the corresponding $\omega_1''=-1.74\times10^8\,\mathrm{rad/s}$ for
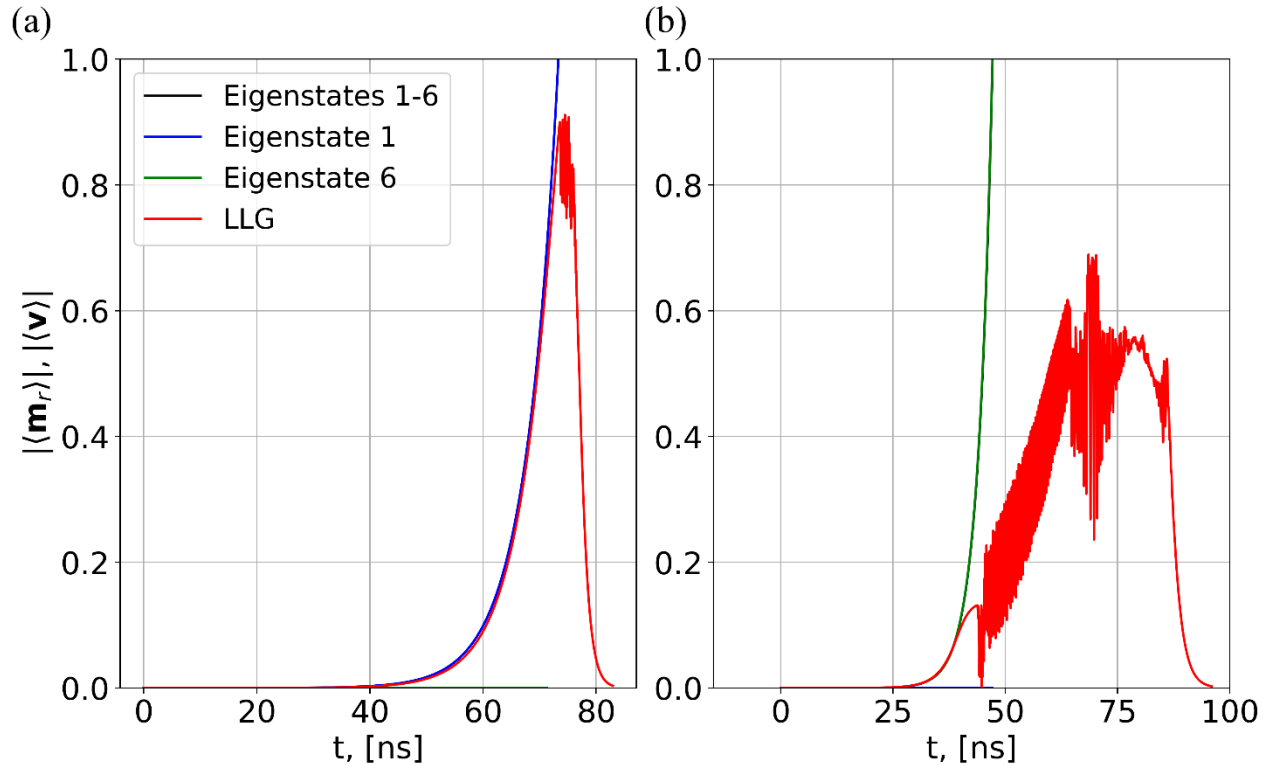
Figure 4.4: Magnetization dynamics obtained via micromagnetic and eigenvalue framework for the confined ψ with $d=10\,\mathrm{nm}$ for (a) $D=40\,\mathrm{nm}$ and (b) $D=80\,\mathrm{nm}$, each with corresponding $I=1.5\tilde{I}_c^{10}$.

$I = 1.5\tilde{I}_c^{10}$ has the largest negative value as compared to the rest of ω_n''. For $D = 80\,\text{nm}$, the switching process is dominated by $\mathbf{v}_6$, which is because $\tilde{I}_c^{10} = \tilde{I}_{c6}^{10}$ and the corresponding $\omega_6'' = -3.11\times10^8\,\text{rad/s}$ for $I = 1.5\tilde{I}_c^{10}$ has the largest negative value. We also find that the switching for $D = 80\,\text{nm}$ is faster than that for $D = 40\,\text{nm}$, which is explained by the greater negative value of the ω_6'' for $D = 80\,\text{nm}$ than ω_1'' for $D = 40\,\text{nm}$. The fact that different eigenstates dominate leads to different time dynamics of the switching process.

To further explain the switching process, Figure 4.5 shows a time sequence of the magnetization snapshots during switching for the confined current distribution with $d = 10\,\text{nm}$ for $D = 40\,\text{nm}$
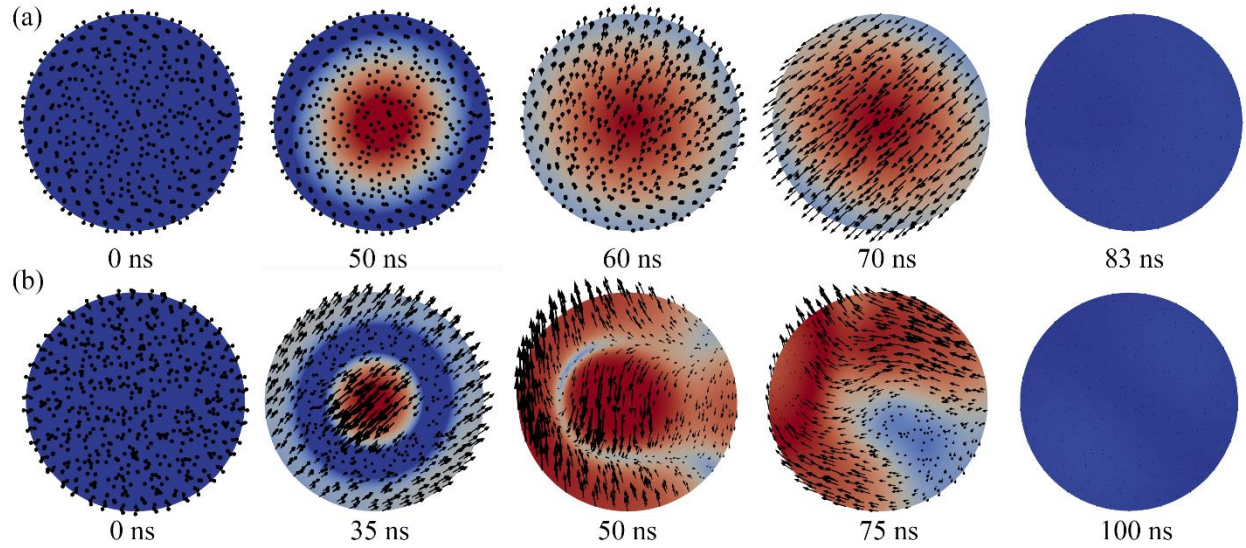
Figure 4.5: Time sequence of the magnetization snapshots during switching for the confined current distribution with $d = 10\,\text{nm}$ for (a) $D = 40\,\text{nm}$ and (b) $D = 80\,\text{nm}$. The arrows are for the magnetization $\mathbf{m}$, whereas the colormap is based on the magnitude of transverse magnetization component $\mathbf{m}_r$ for comparison with Figure 4.3.

and $80\,\text{nm}$. For both D the magnetization spatial distribution during the switching onset, i.e., for early times (the second snapshot from the left), follows the eigenstate spatial distribution. For the $D = 40\,\text{nm}$ and $80\,\text{nm}$ cases, this distribution is that for the $\boldsymbol{\varphi}_1$ and $\boldsymbol{\varphi}_6$ eigenstates, which is in
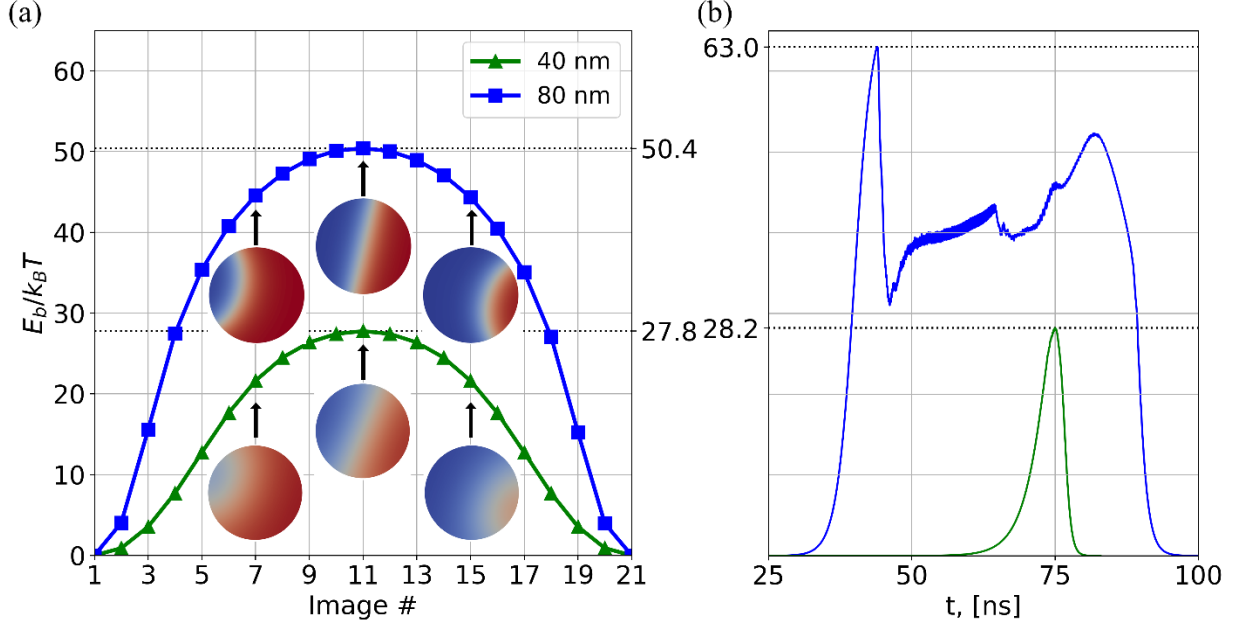
Figure 4.6: (a) Minimal energy path and associated images for $D = 40\,\text{nm}$ and $D = 80\,\text{nm}$, and (b) energy versus time during the STT driven switching with $I = 1.5\tilde{I}_c$ for $D = 40\,\text{nm}$ and $80\,\text{nm}$.

agreement with the fact that $\tilde{I}_c = \tilde{I}_{c1}$ and $\tilde{I}_{c6}$, respectively. For later times, the final switching process is non-linear and spatially non-uniform. For comparison, figure 4.6(a) shows the minimal energy path, including the energy and the magnetization snapshots. The minimal energy path is by domain wall, which is consistent with earlier shown results. As compared to the switching process, the minimal energy path has a different behavior in terms of the reversal onset in that the magnetization spatial distribution does not exhibit any relation to the eigenstates. However, there is a resemblance of the minimal energy path and the STT switching process at later times when non-linear effects kick in. For comparison, Figure 4.6(b) shows the time dependence of the energy during switching for $I = 1.5\tilde{I}_c^{10}$. The energy corresponding to switching and the minimal energy path for $D = 40\,\text{nm}$ follow a similar track in terms of the energy. On the other hand, for $D = 80\,\text{nm}$, the energy corresponding to switching follows a different, more complicated track than the minimal energy path, which is because of more complicated dynamics for larger MTJ sizes.
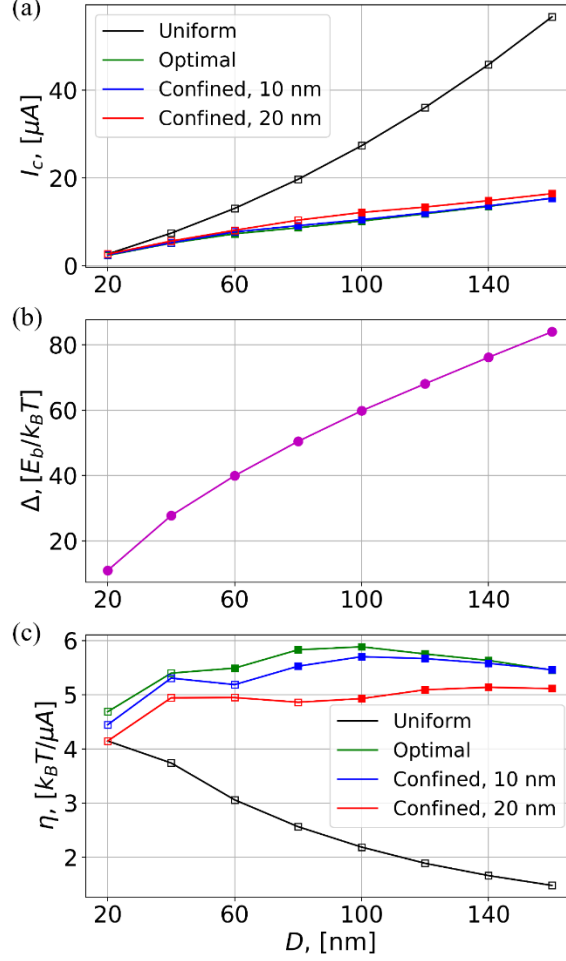
Figure 4.7: Size dependence of the critical current (a), energy barrier (b), and efficiency (c) with different distributions. The empty and solid markers in (a) and (c) correspond to results from eigenstate 1 and eigenstate 6 respectively.

4.4 Efficiency with optimization

We note that the achieved $\tilde{I}_c$, $\tilde{I}_c^{10}$, and $\tilde{I}_c^{20}$ reduction is greater for greater D, which suggests a quantitatively and qualitatively different scaling of the critical current and the corresponding efficiency η as a function of D. To demonstrate this point, Figure 4.7a shows dependences of I_c, $\tilde{I}_c$, $\tilde{I}_c^{10}$, and $\tilde{I}_c^{20}$ as a function of D. The critical current I_c for the uniform ψ, increases slightly less quadratically with D. On the other hand, the minimized $\tilde{I}_c$ scales nearly linearly with D, but

as two curves with a slightly different slope for $D < 60\,\text{nm}$ and $D > 60\,\text{nm}$, corresponding to $\tilde{I}_c = \tilde{I}_{c1}$ and $\tilde{I}_c = \tilde{I}_{c6}$, respectively. The increase of $\tilde{I}_c$ with D is nearly linearly with D, but as two curves with a slightly different slope for $D < 60\,\text{nm}$ and $D > 60\,\text{nm}$, corresponding to $\tilde{I}_c = \tilde{I}_{c1}$ and $\tilde{I}_c = \tilde{I}_{c6}$, respectively. The increase of $\tilde{I}_c$ with D is much slower than that for I_c. For the confined distribution, the scaling of $\tilde{I}_c^{10}$ and $\tilde{I}_c^{20}$ with D is similar to that of the minimized case. An insignificant difference is that the transition between the optimal minimization obtained for $n = 1$ or $n = 6$ occurs at greater D as compared to the fully minimized case. The values of $\tilde{I}_c^{10}$ and $\tilde{I}_c^{20}$ are only slightly greater than those of $\tilde{I}_c$.

Figure 4.7b shows that the energy barrier Δ as a function of D increases slightly less than linearly. The resulting efficiencies obtained as $\eta = \Delta / I_c$, $\tilde{\eta} = \Delta / \tilde{I}_c$, $\tilde{\eta}^{10} = \Delta / \tilde{I}_c^{10}$, and $\tilde{\eta}^{20} = \Delta / \tilde{I}_c^{20}$ are shown in Figure 4.7c. The efficiency η for uniform ψ decreases as $1/D$, which was reported previously [54,70]. The optimized efficiencies $\tilde{\eta}$, $\tilde{\eta}^{10}$, and $\tilde{\eta}^{20}$ are much greater than η, and they nearly constant with respect to the dependence of D; interestingly, $\tilde{\eta}$ is even greater for greater D.

4.5 Non-uniform material parameter distribution

Inspecting the operation of the MTJs with uniform material parameters shows that the reason for the optimal current density distribution being in the central region of the free layer is the fact that the eigenstate is more confined there. The eigenstates can be manipulated by modifying the material parameters to achieve additional MTJ operation improvements. To demonstrate this point, we use spatially varying material parameters, specifically, we choose a spatially varying M_s in two configurations. In the first non-uniform M_s configuration, we use the same

$M_s = 960\,\mathrm{emu/cm^3}$ for $r \geq d$ and a lower $M_s = 480\,\mathrm{emu/cm^3}$ for $r < d$. In the second non-uniform M_s configuration, $M_s = 480\,\mathrm{emu/cm^3}$ for $r \geq d$ and $M_s = 960\,\mathrm{emu/cm^3}$ for $r < d$. Such modified M_s can be achieved, e.g., by ion irradiation [71]. The modulation of M_s modulates the spatial distribution of the effective anisotropy energy density, approximately given by $K_{eff} = K_U - 2\pi M_s^2$ for thin films [72].

Results for $I_c, \tilde{I}_c$, Δ, and $\eta, \tilde{\eta}$ as a function of D for both non-uniform M_s distributions are shown in Figure 4.8. For both distributions with uniform current density (Figures. 4.8(e) and 4.8(f)), the efficiency decreases with D is slower than that for the case of uniform M_s with uniform current density (Figure. 4.7(c)). This can be explained by the fact that the lower K_{eff} assists switching, thus effectively suppressing the critical current increase with D. A benefit is that for both non-uniform M_s distributions, the energy barriers (Figures 4.8(c) and (d)) are higher than the barrier in Figure 4.7(b), which is important to maintain thermal stability. For the first non-uniform M_s distribution, the φ_1 eigenstate is confined to the edge, as shown in the inset of Figure 4.8(a). The corresponding optimized current density distribution, shown in the inset of Figure 4.8(a), is also confined closer to the edge, which differs from that for the uniform M_s in Figure 4.3. The minimized critical current $\tilde{I}_c$ is again significantly reduced as compared to I_c and the efficiency is increased. The optimized efficiency $\tilde{\eta}$ slightly decreases with the size, which is because, for this case, the φ_1 eigenstate determines switching for all considered sizes, and there is not an additional efficiency improvement associated with a higher order eigenstate as in the uniform M_s case. For the second non-uniform M_s distribution, the eigenstate is confined to the center even more than in the uniform M_s case (inset in Figure 4.8(b)). For this case, the optimal

current density distribution is mostly confined to the center and the φ_1 eigenstate also determines switching for all sizes. The behaviors of the critical current density, energy barrier, and efficiency are similar to the first non-uniform distribution.
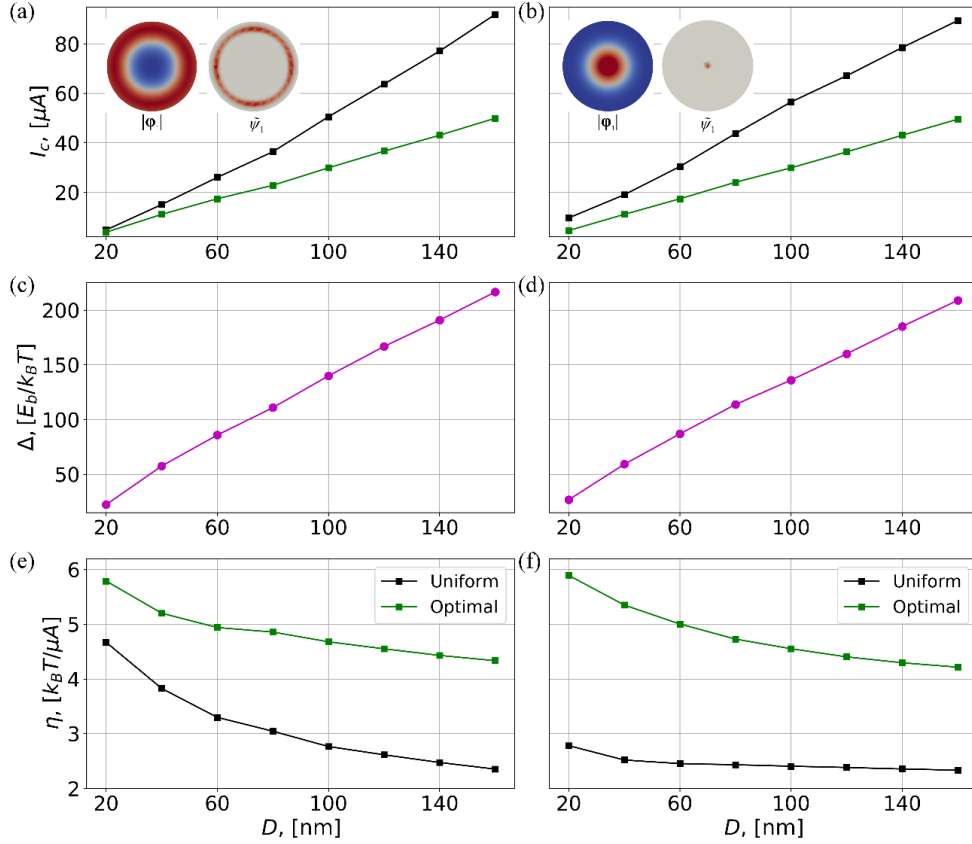
Figure 4.8: Size dependence of (a) the critical current, (c) energy barrier, and (e) efficiency with different current density distributions for a non-uniform M_s with $M_s = 960\,\text{emu/cm}^3$ for $r \geq d$ and $M_s = 480\,\text{emu/cm}^3$ for $r < d$. (b), (d), and (f) are results for $M_s = 480\,\text{emu/cm}^3$ for $r \geq d$ and $M_s = 960\,\text{emu/cm}^3$ for $r < d$. The insets are for the complex magnitudes of the $|\varphi_1|$ eigenstate and the corresponding optimal current density distribution $\tilde{\psi}$.

4.6 Summary

In summary, we showed how it is possible to minimize I_c in MTJs by optimizing $\psi(\mathbf{r})$. The minimization is based on the understanding that finding I_c is equivalent to making one of the eigenstates grow in time. The condition for I_c is given in terms of $\bar{\varphi}_n(\mathbf{r})$, $\bar{\omega}_n$, and $\psi(\mathbf{r})$. I_c can

be viewed as a functional of $\psi(\mathbf{r})$, which can be minimized. We show that the optimized or confined $\psi(\mathbf{r})$ result in a significantly reduced I_c and increased η. Moreover, the optimization results in a major improvement in the scaling of $\tilde{I}_c$ and $\tilde{\eta}$ in that $\tilde{I}_c$ increases nearly linearly and $\tilde{\eta}$ is mostly constant with an increase of the MTJ size. The fact that there is no need to reduce the MTJ size to improve the efficiency opens opportunities for the MTJ optimization. We note that the same minimization approach may be applied to other spintronic systems, e.g., those using SOT or to spin torque oscillators, e.g., to selectively drive their eigenstates.

Acknowledgements

CHAPTER 5

Eigenvalue-based Fokker-Planck approach for thermal statistics analysis

Thermal effects play an important role in determining the operation of magnetic materials and devices. Thermal effects lead to probabilistic magnetization dynamics. For example, in MRAM, the thermal effects result in statistical switching, i.e., switching events should be described by a probability function, which depends on the materials and structure parameters and the temperature. The magnetization switching under STT reacts to thermal fluctuations and results in a distribution of switching times. There is a finite probability that an MRAM cell is switched or not switched for any value of the polarized current. The non-switching probability is known as write error rate (WER). For proper operation, WER needs to be less than 10^{-9} and 10^{-18} with or without an error correction, respectively [73]. It is essential to be able to calculate the WER. Several works have studied WER using different methods. Based on the macrospin model, which is valid for small magnetic elements, analytical analysis can be performed for subcritical [74] and supercritical [75] regimes. For general current values in small-size cases, a FP equation can be derived and used to calculate WER [74]. For larger magnetic elements, in which switching dynamics follows a spatially non-uniform path, the general modeling approach is to simulate the switching process by solving the LLG equation with the stochastic thermal field for many switching events to obtain enough statistical information for calculating the WER. Although recent work has proposed several methods to improve the simulation process, such as batch simulation [76], rare event enhancement [77], and machine learning assistance [78], it is still time consuming and inefficient.

Using FP equation is efficient but only macrospin based FP equation formulations are available, and they are inaccurate for larger sized magnetic elements because they do not account for the spatial non-uniformities in the magnetization switching [74].

In this chapter, we present a FP equation-based approach for calculating the probability densities in nanomagnetic systems characterized by complex magnetization dynamics. First, we discuss how thermal effects can be accounted for in the eigenvalue framework. Next, we introduce the FP formulation based on an eigenstate expansion of the solutions to the L-LLG equation, which allows considering statistical properties of non-uniform magnetization dynamics accounting for all effective magnetic field including STT. The formulations include finding eigenstates and eigenfrequencies of the structure of interest, formulating a FP equation describing the probability density dynamics of the excitation coefficients of the eigenstate solutions, and using this equation for finding derived quantities, such as WER. We show that the magnetization dynamics of the L-LLG equation can be represented in terms of the normal modes and corresponding time dependent coefficients. We then formulate a FP equation related to the magnitude and phase of the time dependent modal coefficient. Next, we show that solving the FP equation gives the probability density function (PDF) as a function of time, which can be related to the magnetization and used to calculate the WER. Compared to the generally used stochastic LLG equation simulations, the presented approach directly obtains the probabilities and WER by solving FP equation only once. Compared to generally used FP equation approaches, the presented formulation allows handling non-uniform dynamics, which otherwise would be impossible. The idea of using FP equation with eigenstate expansion can be generalized to other physical types, such as studying the magnetic susceptibility under AC applied field.

5.1 Thermal noise in eigenvalue framework

In Chapter 1.3, we discussed stochastic LLG equation accounting for the thermal effect in LLG equation. And in Chapter 3, we discussed the eigenvalue framework to solve the L-LLG equation. Following the similar procedure, we can construct the L-LLG equation including the thermal filed

$$\frac{\partial \mathbf{v}}{\partial t} = A\mathbf{v} - \gamma\beta\Lambda(\mathbf{m}_0)\Lambda(\mathbf{m}_0)\mathbf{p} - \gamma\Lambda(\mathbf{m}_0)\mathbf{H}_{th} - \alpha\gamma\Lambda(\mathbf{m}_0)\Lambda(\mathbf{m}_0)\mathbf{H}_{th}, \tag{5.1}$$

where

$$\mathbf{H}_{th} = \sqrt{\frac{2\alpha k_B T}{\gamma V M_S}}\mathbf{G} \tag{5.2}$$

is the thermal field defined in (1.22), and other symbols have the same definitions in. As discussed in Chapter 1.3, $\mathbf{G}$ is a three dimensional normalized Gaussian white noise (GWN) with $<\mathbf{G}>=0$, $<\mathbf{G}^2>=1$, where $<x>$ denotes the expectation of x.

From (5.1) and following the eigenvalue framework derivation steps discussed in Chapter 3, (3.25) with thermal field is written as

$$\frac{da_n}{dt} = j\omega_n a_n + P_n^{stt} + P_n^{th}, \tag{5.3}$$

where

$$P_n^{th} = <-\gamma\Lambda(\mathbf{m}_0)\mathbf{H}_{th} - \alpha\gamma\Lambda(\mathbf{m}_0)\Lambda(\mathbf{m}_0)\mathbf{H}_{th}, A_0\varphi_n>_\Omega, \tag{5.4}$$

with the inner product $<\cdot,\ \cdot>_\Omega$ defined as the volume integral over the structure domain Ω, the subscript n denotes the n-th eigenstates of the system, and the rest of the symbols have the same definitions as in (3.26).

As shown in Chapter 3, the formulation based on the eigenstates represents the system in terms of a typically small number of eigenstate coefficients. The non-uniform dynamics is automatically accounted for by the fact that the eigenstate states are spatially non-uniform.

Statistical properties can be obtained by solving (5.3) repetitively to obtain a sufficient ensemble of realizations. While this approach already allows for a much more efficient and convenient way of computing statistical properties, it is still a brute force approach that requires many simulations and provides limited insights into the physics of the magnetization dynamics. To address these difficulties, an FP equation can be formulated as a counterpart of (5.3), which can be regarded as a Langevin equation, for the probability density function corresponding to the coefficients a_n.

5.2 Fokker-Planck equation based on eigenstates

In this section, we show the derivation of the FP equation from the Langevin equation based on (5.3), including the boundary and initial conditions.

5.2.1 Langevin equation formulation

We represent the coefficients a_n in (5.3) in the polar form $a_n = |a_n| e^{j\phi_n}$, where $|a_n|$ is the complex magnitude and ϕ_n is the complex phase, so that (5.3) can be written as

$$
\begin{aligned}
\frac{d|a_n|}{dt} &= -\omega^i |a_n| + \left(\left(P_{stt}^r\right)_n \cos\phi_n + \left(P_{stt}^i\right)_n \sin\phi_n\right) + \left(\left(P_{th}^r\right)_n \cos\phi_n + \left(P_{th}^i\right)_n \sin\phi_n\right) \\
\frac{d\phi_n}{dt} &= \omega^r + \frac{1}{|a_n|}\left(\left(P_{stt}^i\right)_n \cos\phi_n - \left(P_{stt}^r\right)_n \sin\phi_n\right) + \frac{1}{|a_n|}\left(\left(P_{th}^i\right)_n \cos\phi_n - \left(P_{th}^r\right)_n \sin\phi_n\right)
\end{aligned}
, \quad (5.5)
$$

where the superscripts r and i represent the real and imaginary part of the complex values, respectively. Note the statical properties of the random variables, i.e., the thermal field, in (5.5) can be viewed as a multi-dimensional Langevin equation [79]:

$$
\begin{aligned}
\frac{d|a_n|}{dt} &= h_1 + \sum_{i=\mathbf{e}_1,\mathbf{e}_2} g_{1i} H_{th}^i(t) \\
\frac{d\phi_n}{dt} &= h_2 + \sum_{i=\mathbf{e}_1,\mathbf{e}_2} g_{2i} H_{th}^j(t)
\end{aligned}
. \quad (5.6)
$$

Here,

$$h_1 = -\omega^i \mid a_n \mid + P_{stt}^r \cos\phi_n + P_{stt}^i \sin\phi_n$$

$$h_2 = \omega^r + \frac{1}{\mid a_n \mid}(P_{stt}^i \cos\phi_n - P_{stt}^r \sin\phi_n)$$

$$g_{1\mathbf{e}_1} = R_{\mathbf{e}_1}^n \cos\phi_n + I_{\mathbf{e}_1}^n \sin\phi_n$$

$$g_{1\mathbf{e}_2} = R_{\mathbf{e}_2}^n \cos\phi_n + I_{\mathbf{e}_2}^n \sin\phi_n \qquad , \qquad (5.7)$$

$$g_{2\mathbf{e}_1} = \frac{1}{\mid a_n \mid}(I_{\mathbf{e}_1}^n \cos\phi_n - R_{\mathbf{e}_1}^n \sin\phi_n)$$

$$g_{2\mathbf{e}_2} = \frac{1}{\mid a_n \mid}(I_{\mathbf{e}_2}^n \cos\phi_n - R_{\mathbf{e}_2}^n \sin\phi_n)$$

and

$$R_n^{\mathbf{e}_1} = \alpha\gamma'\left(\varphi_{\mathbf{e}_1}^r\right)_n + \gamma'\left(\varphi_{\mathbf{e}_2}^r\right)_n$$

$$R_n^{\mathbf{e}_2} = \alpha\gamma'\left(\varphi_{\mathbf{e}_2}^r\right)_n - \gamma'\left(\varphi_{\mathbf{e}_1}^r\right)_n$$

$$I_n^{\mathbf{e}_1} = -\alpha\gamma'\left(\varphi_{\mathbf{e}_1}^i\right)_n - \gamma'\left(\varphi_{\mathbf{e}_2}^i\right)_n \qquad , \qquad (5.8)$$

$$I_n^{\mathbf{e}_2} = -\alpha\gamma'\left(\varphi_{\mathbf{e}_2}^i\right)_n + \gamma'\left(\varphi_{\mathbf{e}_1}^i\right)_n$$

where the subscript $\mathbf{e}_1$ and $\mathbf{e}_2$ represent the unit basis vector in $TM(\mathbf{m}_0)$ as defined in (3.13).

In the multi-dimensional Langevin equation (5.6), the h_1 and h_2 terms are the force terms accounting for micromagnetic interactions and spin torques, the $g_{1\mathbf{e}_1}, g_{1\mathbf{e}_2}, g_{2\mathbf{e}_1} g_{2\mathbf{e}_2}$ terms are drift terms accounting for the stochastic thermal field.

5.2.2 Fokker-Planck equation formulation

We define a time dependent probability density function (PDF) $\rho_n(\mid a_n \mid, \phi_n; t)$ for the magnitude and phase coefficients $\mid a_n \mid$ and ϕ_n at time t. The FP equation is a time-dependent partial differential equation for the PDF $\rho_n(\mid a_n \mid, \phi_n; t)$, which is obtained from the Langevin equation (5.6) based on the Kramers-Moyal expansion [79]:

$$\frac{\partial}{\partial t}\rho_n(\mid a_n \mid, \phi_n; t) = -\sum_{\substack{k=1,2 \\ a_p=\mid a_n\mid,\phi_n}} \frac{\partial}{\partial a_p}(A_k\rho_n) + \sum_{\substack{k,l=1,2 \\ a_p,a_q=\mid a_n\mid,\phi_n}} \frac{\partial}{\partial a_p \partial a_q}(B_{kl}\rho_n), \qquad (5.9)$$

77

where

$$A_k = h_k + \mu \sum_{\substack{a_p = |a_n|, \phi_n \\ i = x, y}} \frac{\partial g_{ki}}{\partial a_p} g_{ic}, \ B_{kl} = \mu \sum_{i = x, y} g_{ki} g_{li} \,, \tag{5.10}$$

are terms calculated from the Langevin equation (5.6) terms, and $\mu = 2\alpha k_B T / \gamma V M_S$ is the variance of the thermal field. Solving the FP equation gives the time dependent PDF of time coefficients of each eigenstate coefficient. The PDF of the magnetization can be obtained based on the PDFs of the eigenstate coefficients.

5.2.3 Boundary conditions and initial conditions

The FP equation (5.9) can be solved numerically with proper boundary and initial conditions. First, for boundary conditions, it is natural that the phase ϕ_n should satisfy the periodicity boundary condition

$$\phi_n(0) = \phi_n(2\pi) \,. \tag{5.11}$$

Considering the normalization and conservation of the probability, the magnitude $|a_n|$ should satisfy the zero flux boundary condition

$$\frac{\partial |a_n|}{\partial \hat{\mathbf{n}}} |_{\partial \Omega} = 0 \,, \tag{5.12}$$

where $\hat{\mathbf{n}}$ is the unit vector on the boundary of magnetic domain.

The initial condition for FP equation (5.9), i.e. $\rho_n(|a_n|, \phi_n; t = 0)$, is obtained by setting $P_n^{stt} = 0$ under infinite time. Note that $\left(P_{th}^r\right)_n$ and $\left(P_{th}^i\right)_n$ are linear transformations of the Gaussian
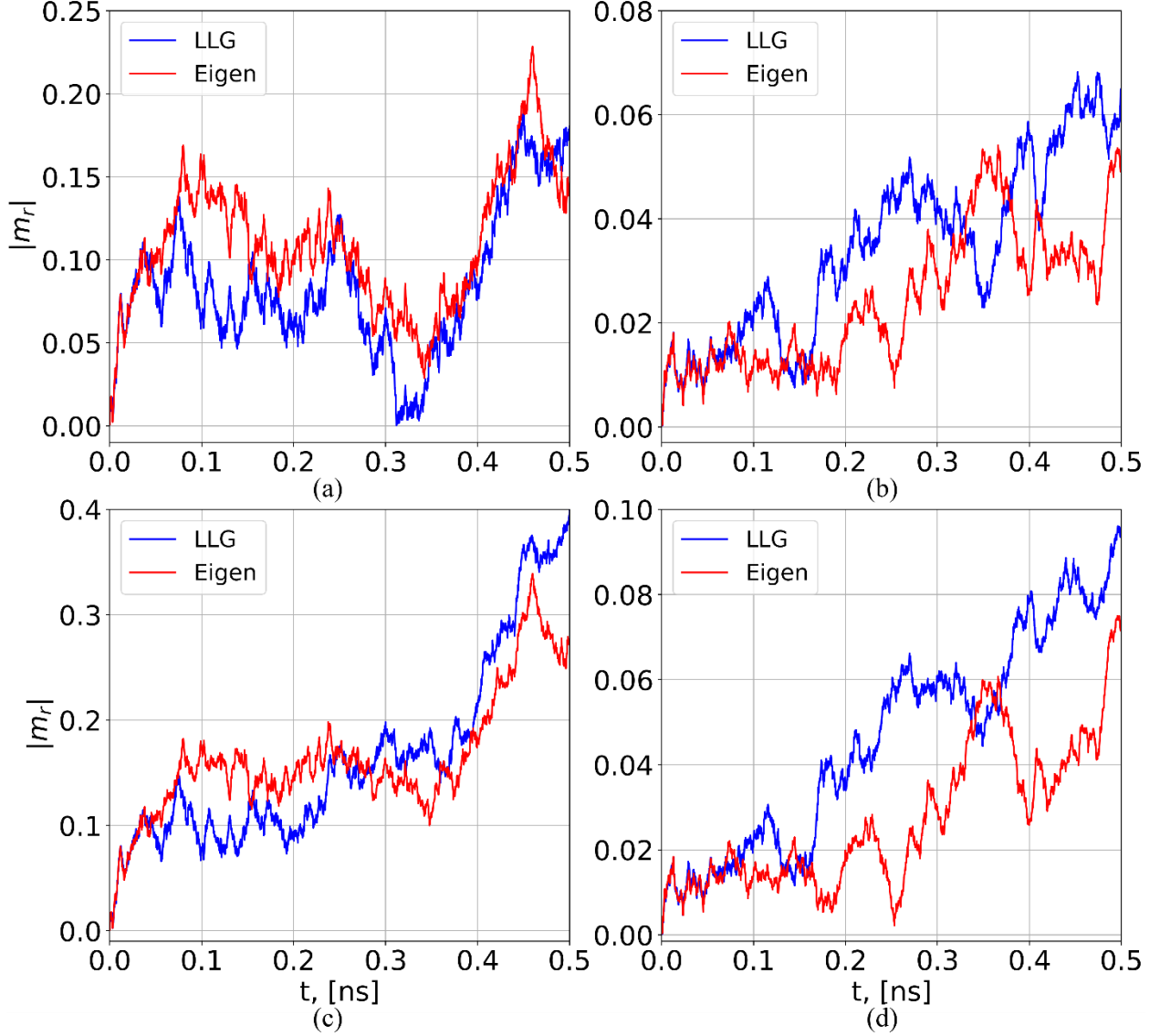
Figure 5.1: Spatially averaged in-plane magnetization component m_r with a constant current for (a) and (c) $D = 20\,\text{nm}$ and (b) and (d) $D = 80\,\text{nm}$ with finite temperature $T = 300K$. The current $J = 1.5 J_c$ ((a) - (b)) and $J = 10 J_c$ ((c)-(d)).

white noise $\mathbf{H}_{th}$, so that they also follow the normal distribution with dispersions of the Gaussian

distribution $N(0, (\sigma_{pth}^r)^2)$ and $N(0, (\sigma_{pth}^i)^2)$, respectively, where

$$
\begin{aligned}
\left(\sigma_{pth}^r\right)^2 &= \left[\left(-\alpha\gamma'\varphi_x^r + \gamma'\varphi_y^r\right)^2 + \left(-\gamma'\varphi_x^r - \alpha\gamma'\varphi_y^r\right)^2\right]\mu \\
\left(\sigma_{pth}^i\right)^2 &= \left[\left(-\alpha\gamma'\varphi_x^i + \gamma'\varphi_y^i\right)^2 + \left(-\gamma'\varphi_x^i - \alpha\gamma'\varphi_y^i\right)^2\right]\mu
\end{aligned}
\tag{5.13}
$$

are the variances of the Gaussian distribution. Consequently, the real and imaginary parts of the coefficient a_n, i.e. a_n^r and a_n^i, also follow the Gaussian distribution $N(0, (\sigma_{a^r})^2)$ and $N(0, (\sigma_{a^i})^2)$, respectively, where

$$
\begin{aligned}
(\sigma_{a^r})^2 &= \frac{2\omega^{i^2} + \omega^{r^2}}{4\omega^i(\omega^{i^2} + \omega^{r^2})}(\sigma_{pth}^r)^2 + \frac{\omega^{r^2}}{4\omega^i(\omega^{i^2} + \omega^{r^2})}(\sigma_{pth}^{im})^2 \\
(\sigma_{a^i})^2 &= \frac{2\omega^{i^2} + \omega^{r^2}}{4\omega^i(\omega^{i^2} + \omega^{r^2})}(\sigma_{pth}^{im})^2 + \frac{\omega^{r^2}}{4\omega^i(\omega^{i^2} + \omega^{r^2})}(\sigma_{pth}^{re})^2
\end{aligned}
\tag{5.14}
$$

Note that for a complex random variable, if the real and imaginary parts follow the Gaussian distribution, the magnitude and phase should follow the Rayleigh distribution [80]. Therefore, the resulting initial PDF is given by

$$
\rho_n(|a_n|, \phi_n; t = 0) = \frac{|a_n| \exp\left(-\frac{1}{2}|a_n|^2\left(\frac{\cos^2(\phi_n)}{(\sigma_{a^r})^2} + \frac{\sin^2(\phi_n)}{(\sigma_{a^i})^2}\right)\right)}{2\pi\sigma_{a^r}\sigma_{a^i}}.
\tag{5.15}
$$

With the boundary and initial conditions, the FP equation can be solved numerically to get the PDF of the coefficient a_n.

5.3 Write error rate analysis

5.3.1 Write error rate from probability density function

An important quantity for the system can be calculated from the PDF is WER. To calculate WER, we first characterize the switching behavior by the average in-plane magnetization, as discussed in Chapter 3. From (3.24), we have the average in-plane magnetization $<\mathbf{v}_{inp}> = \sqrt{(\mathbf{v}_x)^2 + (\mathbf{v}_y)^2}$. The non-switching condition can be defined as $<\mathbf{v}_{inp}> \leq s$, where s is a certain critical value. Using (5.9), the time dependent non-switching probability is given by

$$P_{ns}(t) = \int_{<\mathbf{v}_{inp}>\leq s} \rho(a_m, a_\phi; t) da_m da_\phi. \qquad (5.16)$$

To determine the integration upper limit, we consider the approximation

$$<\mathbf{v}_{inp}> \approx \sum_n <\mathbf{v}_{inp}>_n, \qquad (5.17)$$

where the average in-plane magnetization is approximately equal to the sum of the average in-plane magnetization of each eigenstate. For each eigenstate, we consider the condition independently, such that

$$<\mathbf{v}_{inp}>_n \leq s_n, \qquad (5.18)$$

and the total upper limit is the sum of the upper limit of each eigenstate s_n, i.e.

$$s = \sum_n s_n. \qquad (5.19)$$

Considering the non-switching probability for each eigenstate, where we have the upper limit u_n for each eigenstate, we have

$$[P_{ns}(t)]_n = \int_0^{2\pi} d\phi_n \int_0^{u_n} \rho(|a_n|, \phi_n; t) d|a_n| \qquad (5.20)$$

where the upper limit u_n is calculated from the in-plane magnetization upper limit of each eigenstate s_n:

$$u_n = s / \left(2\sqrt{\left(\left[\varphi_x^{m_n} \cos\left(\phi_n + \varphi_x^{\phi_n}\right)\right]\right)^2 + \left(\left[\varphi_y^{m_n} \cos\left(\phi_n + \varphi_y^{\phi_n}\right)\right]\right)^2} \right), \qquad (5.21)$$

where φ^{m_n} and φ^{ϕ_n} denote the magnitude and phase of the n-th eigenstate, respectively.

With the non-switching probability of each eigenstate, and the approximation in (5.17), the WER is the total non-switching probability combined of all the eigenstates

$$P_{ns}(t) = \sum_{s_n} \prod_n [P_{ns}(t)]_n. \tag{5.22}$$

5.3.2 Write error rate results

As an example of using the presented framework, we consider switching in a MTJs, which is comprised of a cylindrical free layer of 1 nm thickness and diameter (*D*) of 20nm and 80nm for
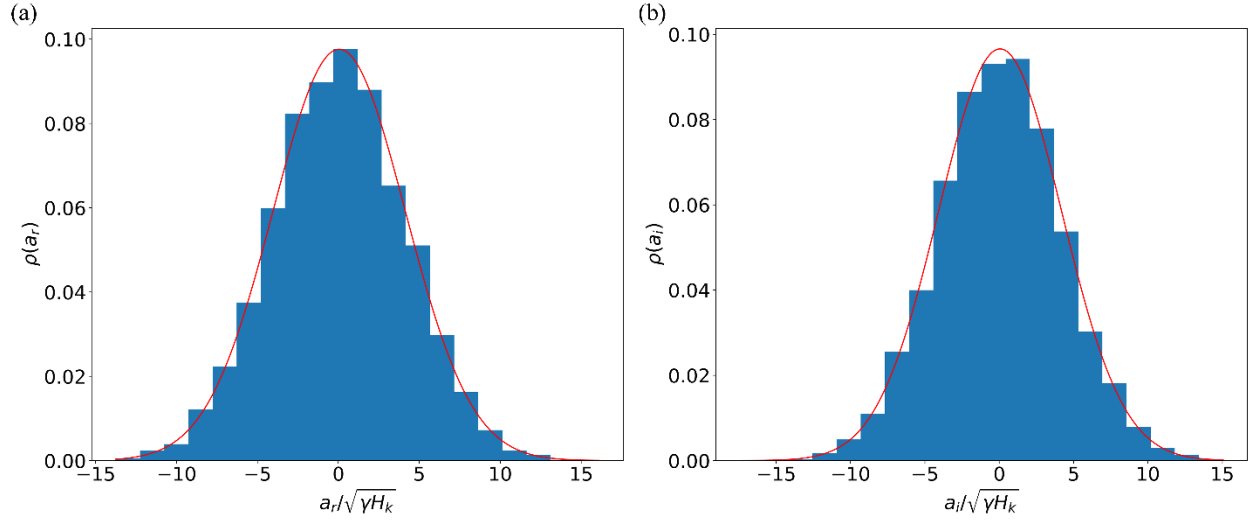
Figure 5.2: The initial distribution of normalized (a) a_r and (b) a_i. Histogram shows the 10000 times simulation from eigenvalue framework based on (5.3) with $P^{stt} = 0$. The red line shows the Gaussian distribution from (5.14). The results are for $n = 1$ eigenstate of the system.

temperatures (*T*) of 100K and 300K. The magnetic material parameters are with the uniaxial anisotropy $K_U = 6.11 \, \text{Merg/cm}^3$ of the easy axis perpendicular to the disc, saturation magnetization $M_s = 960 \, \text{emu/cm}^3$, exchange stiffness $A_{ex} = 1 \, \mu\text{erg/cm}$, and damping constant α = 0.01. An STT field is applied to the bottom surface of the cell.

The WER is calculated in two steps. First, we carried out eigenstate calculations as a part of the finite element method based micromagnetic simulator FastMag [19]. The numerical eigenvalue problem is solved with an iterative implicitly restarted and preconditioned Arnoldi method [67]. Details of the eigenstate solver framework analysis are given in Chapter 3. The eigen solver results indicate the active modes involved in the switching process, where the imaginary

parts of the eigenfrequencies are negative. We, then, use the presented FP equation (5.9) formulation to calculate the PDF and WER. The FP equation is solved numerically with the FEniCS software [81].
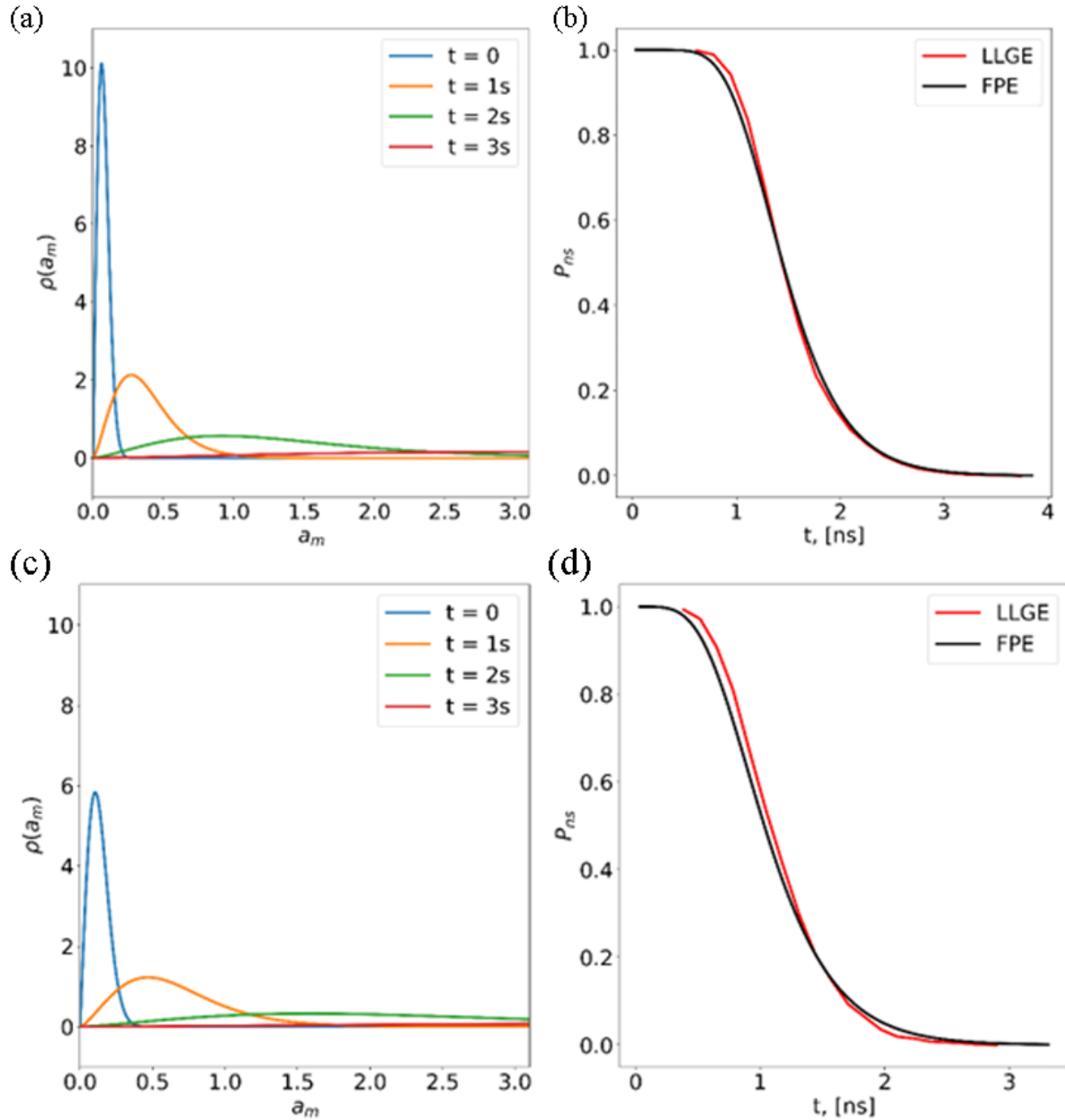

Figure 5.3: WER results for $D = 20$nm with current $I = 9.5\mu$A for temperature (a)-(b) $T = 100$K and (c)-(d) $T = 300$K. (a) (c) Marginal PDF of normalized eigen framework time coefficient magnitude for different time. (b) (d) WER results based on stochastic LLG simulations and FP equation solution.

To illustrate the switching process and WER with the thermal effect, we first show solutions of the linearized LLG equation from the eigenvalue framework with thermal fields. Figure 5.1 shows the results for a $D = 80\,\text{nm}$ disc with the magnetic parameters listed above and $T = 300K$. The thermal filed for eigenvalue framework and stochastic LLG equation simulations are calculated with same random seed. The eigenvalue-based results are in a good agreement with the stochastic LLG equation simulations.

Next, to validate the initial condition derived in 5.2.3, in Figure 5.2, we show the marginal distribution of the coefficients a_1^r and a_1^i with the finite temperature $T = 300K$ based on the distribution of (5.14) and the histogram from 10,000 times simulations based on (5.3). The marginal distribution of a^r and a^i are defined as

$$
\begin{aligned}
\rho(a^r;t) &= \int_{a^i} \rho(a^r,a^i;t)da^i \\
\rho(a^i;t) &= \int_{a^r} \rho(a^r,a^i;t)da^r
\end{aligned}
\tag{5.23}
$$

The agreement indicates the validity of the initial condition.

Next, we show PDF and WER obtained by solving the FP equation. For validation, we also compare the WER results with WER obtained by running 10,000 times the stochastic LLG equation simulations and counting the number of switching and non-switching events. This number of stochastic simulations results in the P_{ns} accuracy on the order of 10^{-4}.

Figure 5.3 shows results for a smaller diameter of $D = 20\text{nm}$ with $I = 9.5\mu A$ and temperatures of $T = 100\text{K}$ and $T = 300\text{K}$. For this current, only the first eigenstate with the smallest eigenfrequency is active. Figure 5.3a shows the marginal distribution of the time coefficient magnitude at different times. The WER can be regarded as the area below the curve up to the upper limit. The initial parameter marginal distribution at $t = 0$ due to the thermal

84

fluctuations localize in a small range near zero. Also, the higher (room) temperature of 300K has a broader initial distribution. Due to the STT effects, for
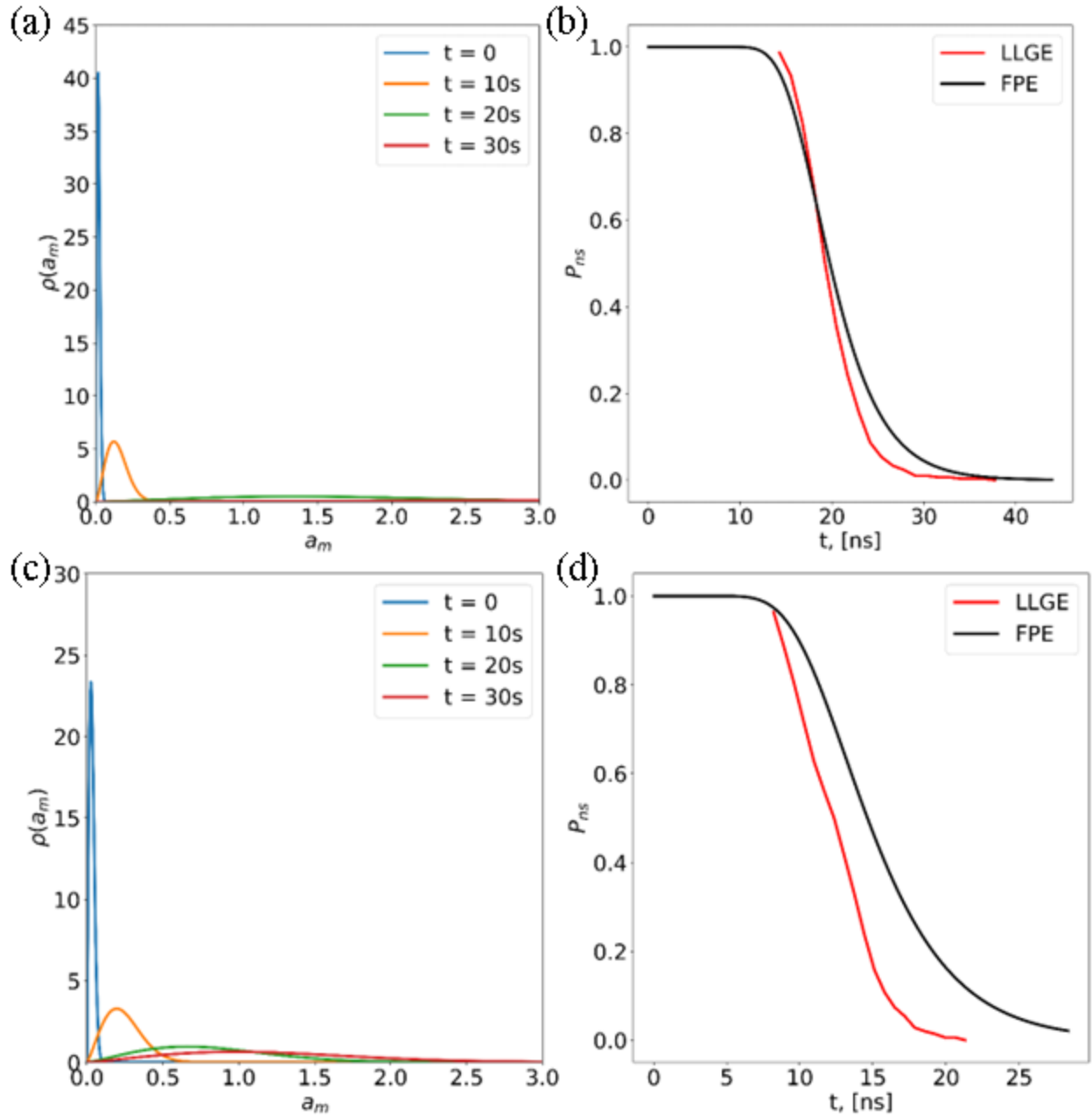
Figure 5.4: WER results for $D = 80$nm with current $I = 29.5\mu\text{A}$ for (a)-(b) $T = 100$K and (c)-(d) $T = 300$K. (a) (c) Marginal PDF of eigen framework time coefficient magnitude for different time. (b) (d) WER results based on stochastic LLG simulations and FP equation solution.

$t > 0$, the distribution is flattened, and the non-switching probability decreases. Figure 5.3b shows the time evolution of WER from the FP equation and LLG equation calculations. The results show

an agreement between the stochastic LLG equation and FP equation simulations. We see that the

higher temperature
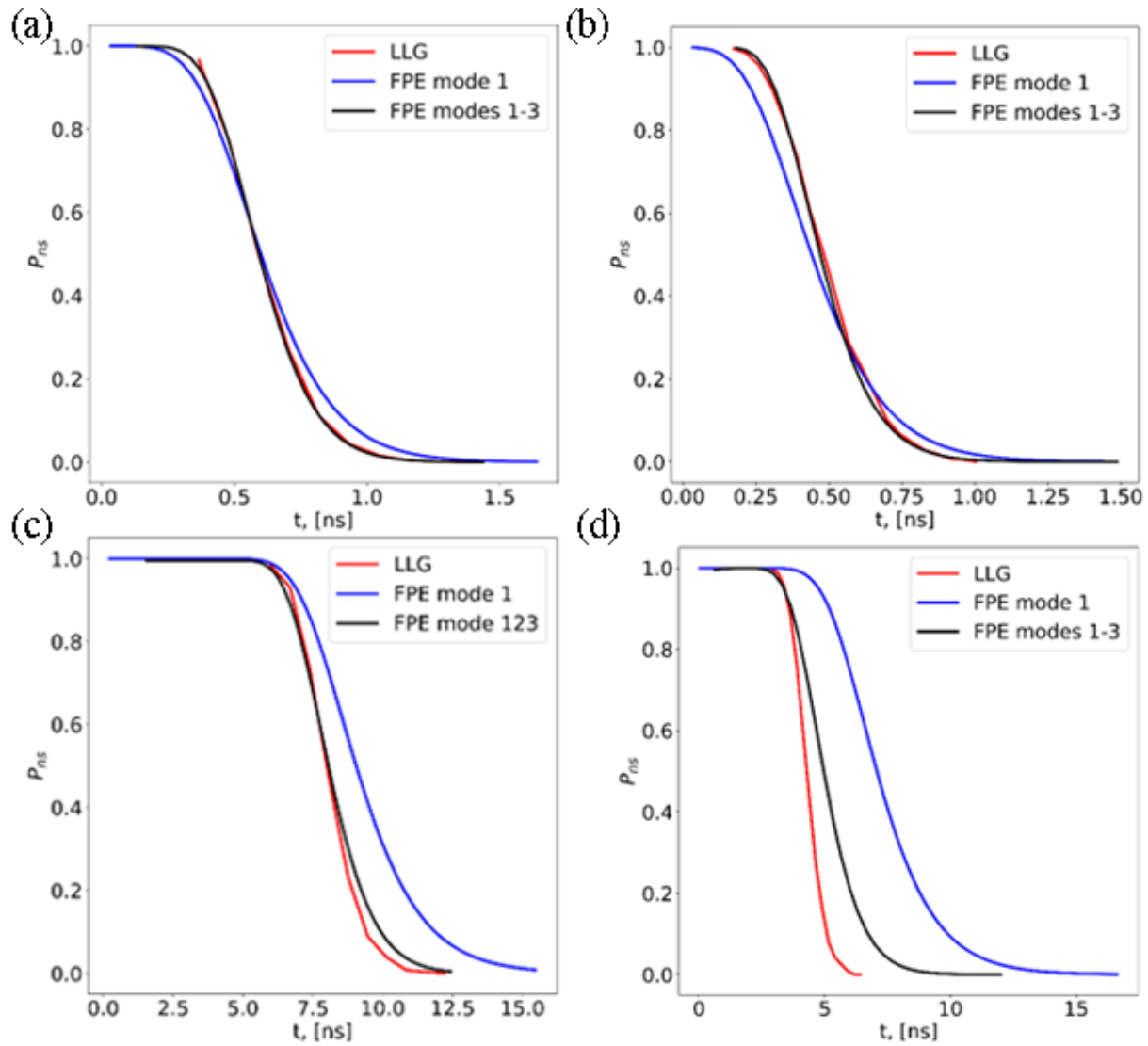
Figure 5.5: WER results for (a)-(b) $D = 20\text{nm}$ with current $I = 21\mu\text{A}$ for temperature (a) 100K and (b) 300K. (c)-(d) $D = 80\text{nm}$ with current $I = 45\mu\text{A}$ for temperature (c) 100K and (d) 300K.

has greater thermal effects, which results in a more flattened marginal distribution and a faster

switching time. For the higher temperature, the FP equation model slightly overestimates P_{ns},

more so for smaller currents, which is related to the linearized approximation. Nevertheless, it still

represents the exponential decay rate of the WER well.

Figure 5.4 shows similar results for the larger diameter of $D = 80$nm with the current of $I = 29.5$μA. For this current, only the lowest eigenfrequency eigenstate is active. Compared to the smaller diameter, the initial distribution for the same temperature has a smaller variance, which is consistent with a greater thermal stability. For the larger case, where the macrospin approximation is invalid [54,82], the presented FP equation approach also shows an agreement with the stochastic LLG equation results for predicting WER.

Next, we show WER for greater currents for different sizes and temperatures. Figure 5.5 shows WER for $I = 21$μA for $D = 20$nm, and $I = 45$μA for $D = 80$nm for $T = 100$K and $T = 300$K, respectively. For these currents, both sizes have 3 active modes. We show the FP equation WER results using 1 mode and all active modes. For $D = 20$nm, we see that although FP equation results with all active modes slightly underestimate the WER, the use of FP solutions for multiple eigenstates results in a much better approximation with a better agreement with the stochastic LLG equation results.

5.4 Summary

In summary, we presented a FP approach based on the eigenstate expansion of the solutions of the linearized LLG equation, which allows studying WER of STT MRAM due to the thermal noise. We found eigenstates and corresponding eigenfrequencies of the structure, accounting for all effective magnetic field including spin transfer torque. We developed a framework that represents the magnetization dynamics of the L-LLG equation in terms of the eigen modes and corresponding time dependent coefficients. We then formulated a FP equation related to the magnitude and phase of the complex time dependent modal coefficients. Solving the FP equation gives the PDF as a function of time, which can be related to the magnetization and used to calculate

the WER. Compared to the generally used stochastic LLG equation simulations in the time domain, the presented approach directly obtains the WER by solving FP equation only once, and it is scalable to large cases where non-uniform dynamics occurs.

Acknowledgements

CHAPTER 6

Linearized frequency domain Landau-Lifshitz-Gilbert Equation Solver

LLG equation (1.4) is a time dependent non-linear equation, and it describes the magnetization dynamics in both linear and non-linear regimes. Solving LLG equation can be computationally expensive as it requires obtaining solutions at many time steps and it is often numerically stiff, which may require either small time steps or assisting linear solvers. Under weak dynamics excitations, however, the magnetization dynamic response may be linear. Examples of such systems are spin wave excitations under weak time-dependent applied fields or the initial dynamics under spin torque excitations [15,63]. In such cases, LLG equation can be linearized in terms of a weak magnetization deviation around the equilibrium state. Such linearization has been used to obtain solutions in terms of the eigenstate representations [82] and it can be used to obtain solutions even for non-linear problems [83–85]. For a linearized LLG equation, we can find solutions as a response to a harmonic excitation, i.e., an excitation at a given frequency.

In this Chapter, we present a linear frequency domain LLG (FD-LLG) equation solver. The FD-LLG equation solver provides a linearized magnetization solution as a response to a dynamic excitation, e.g., the applied field, which is a characterized by a given frequency. Considering a given frequency allows formulating a time independent linear equation for a complex magnetization amplitude, which can, then, be used to provide linear time domain solutions. The FD-LLG equation solver is developed based on the finite element based micromagnetic simulator FastMag. The linear system is solved effectively with an iterative solver. The number of iterations

is significantly reduced using a linear preconditioner. Solving the FD-LLG equation is much more efficient and provides a more physically insight than solving the original LLG equation.

6.1 Linearized Landau-Lifshitz-Gilbert Equation

We start by introducing the LLG equation linearized equation, including a static and dynamic applied magnetic field. The linearization derivation and the equation parameter definitions are similar to those given in Chapter 3. We repeat some of the definition for completeness for the case considered in this Chapter.

The magnetization dynamics is described by the LLG equation, which is, in its implicit form, is written as

$$\frac{\partial \mathbf{m}}{\partial t} = -\gamma \mathbf{m} \times \mathbf{H}_{eff} + \alpha \mathbf{m} \times \frac{\partial \mathbf{m}}{\partial t}, \tag{6.1}$$

where, similar to Chapter 3, $\mathbf{m}$ is the normalized magnetization, γ is the gyromagnetic ratio, α is the damping constant, and $\mathbf{H}_{eff}$ is the effective field. The effective field is a function of $\mathbf{m}$, and it is composed of several components, including the magnetostatic field $\mathbf{H}_{ms}$, exchange field $\mathbf{H}_{ex}$, anisotropy field (assumed uniaxial) $\mathbf{H}_{an}$, and an applied Zeeman field $\mathbf{H}_{a}$:

$$\mathbf{H}_{eff} = \mathbf{H}_{ms} + \mathbf{H}_{ex} + \mathbf{H}_{an} + \mathbf{H}_{a} \equiv C\mathbf{m} + \mathbf{H}_{a},$$

$$\mathbf{H}_{ms} = M_{s}\nabla \int \frac{\nabla \cdot \mathbf{m}}{|\mathbf{r} - \mathbf{r}'|} d\mathbf{r}',$$

$$\mathbf{H}_{ex} = \frac{2A}{M_{s}}\nabla^{2}\mathbf{m},$$

$$\mathbf{H}_{an} = H_{K}(\hat{\mathbf{k}} \cdot \mathbf{m})\hat{\mathbf{k}}, \tag{6.2}$$

where the applied field can be expressed as a time independent DC part $\mathbf{H}_{a,0}$, and a time dependent AC part $\mathbf{h}_{a}(t)$:

$$\mathbf{H}_{a} = \mathbf{H}_{a,0} + \mathbf{h}_{a}(t) \tag{6.3}$$

The LLG equation (6.1) is non-linear in $\mathbf{m}$ due to the presence of the cross products and it describes the magnetization dynamics in a broad range of situations, including linear and non-linear effects. In various cases, however, the general LLG equation can be linearized. Such a linearization is allowed when the magnetization varies insignificantly around its equilibrium state. Weak magnetization variations can be due to weak excitations, e.g., by weak applied fields or by spin transfer torque (STT). Even in the general non-linear cases, the initial dynamics that contains important information about the system behavior can be characterized by the linearization [82,83].

We present a framework that uses a L-LLG equation to study the magnetization dynamics. We first present a linearized time domain LLG equation. Then, we construct a FD-LLG equation to study small oscillations around the equilibrium state driven by time-harmonic excitations. We seek a solution for small magnetization deviation $\mathbf{v}$ around the equilibrium state such that

$$\mathbf{m} = \mathbf{m}_0 + \mathbf{v} \,, \tag{6.4}$$

here $\mathbf{m}_0$ is the equilibrium magnetization state for the system without a dynamic excitation. which is given by the Brown condition [1]

$$\mathbf{m}_0 \times \mathbf{H}_{eff}(\mathbf{m}_0) = 0 \,, \tag{6.5}$$

which corresponds to $\partial \mathbf{m}_0 / \partial t = 0$ in the LLG equation.

The magnetization deviation $\mathbf{v}$ is normal to $\mathbf{m}_0$, so that the normalization of $\mathbf{m}$ is preserved. Because of the linearity of $\mathbf{H}_{eff}(\mathbf{m})$ in terms of $\mathbf{m}$, we can write $\mathbf{H}_{eff}(\mathbf{m}) = \mathbf{H}_0 + C\mathbf{v}$, where $\mathbf{H}_0 = \mathbf{H}_{eff}(\mathbf{m}_0) + \mathbf{H}_{a,0}$. Considering the week dynamic applied field $\mathbf{h}_a(t)$, inserting representation (6.5) into LLG equation (6.1), and linearizing the equation by keeping only the terms linear in $\mathbf{v}$, α and $\mathbf{h}_a$, we can write a linearized LLG equation for $\mathbf{v}$:

$$\frac{\partial \mathbf{v}}{\partial t} = -\gamma (\mathbf{v} \times \mathbf{H}_0 + \mathbf{m}_0 \times \mathbf{h} + \mathbf{m}_0 \times \mathbf{h}_a) + \alpha \mathbf{m}_0 \times \frac{\partial \mathbf{v}}{\partial t} , \tag{6.6}$$

where $\mathbf{h} = C\mathbf{v}$ is the effective field corresponding to $\mathbf{v}$. Denoting the cross operator as $\Lambda(\mathbf{u})\mathbf{v} = \mathbf{u} \times \mathbf{v}$, we can reformat (6.6) in matrix format

$$\frac{\partial \mathbf{v}}{\partial t} = -\gamma \left(\Lambda(\mathbf{H}_0)\mathbf{v} + \Lambda(\mathbf{m}_0)\mathbf{h} + \Lambda(\mathbf{m}_0)\mathbf{h}_a \right) + \alpha \Lambda(\mathbf{m}_0) \frac{\partial \mathbf{v}}{\partial t} . \tag{6.7}$$

Since $\mathbf{v}$ is normal to $\mathbf{m}_0$, we can project every vector and operator into the tangent space $TM(\mathbf{m}_0)$ of $\mathbf{m}_0$, by using the projection operator [59]

$$P_{\mathbf{m}_0} = (I - \mathbf{m}_0 \otimes \mathbf{m}_0) , \tag{6.8}$$

where $\otimes$ denotes the dyadic Kronecker tensor product, I denotes the identity matrix. It can be shown that when restricted to vector fields in $TM(\mathbf{m}_0)$, the operator $\Lambda(\mathbf{m}_0)$ is linear and anti-symmetric and it is also invertible [59], i.e.,

$$\Lambda(\mathbf{m}_0)\Lambda(\mathbf{m}_0) = -I . \tag{6.9}$$

With (6.8) and (6.9), we can simplify (6.7) by multiplying $\Lambda(\mathbf{m}_0)$ at both sides:

$$B_\perp \frac{\partial \mathbf{v}}{\partial t} + \gamma A_\perp \mathbf{v} = \gamma \mathbf{h}_a , \tag{6.10}$$

where

$$\begin{aligned} A_\perp &= P_{\mathbf{m}_0} \left((\mathbf{H}_0 \cdot \mathbf{m}_0)I - C \right) \\ B_\perp &= P_{\mathbf{m}_0} \left(\Lambda(\mathbf{m}_0) + \alpha I \right) \end{aligned} . \tag{6.11}$$

6.2 Linear solver

Assuming a time harmonic excitation at a circular frequency ω, the applied field can be written as

$$\mathbf{h}_a = \mathrm{Re}\left\{ \sum_n \tilde{\mathbf{h}}_a(\mathbf{r}) e^{jn\omega t} \right\}, \tag{6.12}$$

where $\tilde{\mathbf{h}}_a$ is the complex amplitude of the exciting magnetic field, which represents its magnitude and phase. Assuming the linearity of the response, the small deviation $\mathbf{v}$ can be expressed as

$$\mathbf{v} = \mathrm{Re}\left\{ \sum_n \tilde{\mathbf{v}}(\mathbf{r}) e^{jn\omega t} \right\}, \tag{6.13}$$

where $\tilde{\mathbf{v}}$ is the complex amplitude of the magnetization deviation. Inserting (6.13) into (6.11), we obtain the FD-LLG equation

$$(j\omega B_\perp + \gamma A_\perp)\tilde{\mathbf{v}} = \gamma \tilde{\mathbf{h}}_a . \tag{6.14}$$

Here, $\tilde{\mathbf{h}}_a$ in the right-hand side is a known function of spatial coordinates and $\tilde{\mathbf{v}}$ is an unknown, which is found by solving the linear system of equations.

The linear system matrix of (6.14) is dense due to the presence of the magnetostatic field operator $\mathbf{H}_{ms}$. Therefore, to enable solving large problems, iterative methods, such as the conjugated gradient (CG) or generalized minimal residual method (GMRES) [86], typically should be used. Micromagnetic problems often are stiff, which results in a badly conditioned matrix and many linear iterations required for the solution. Reducing the number of iterations can be achieved by developing a proper preconditioner. It has been shown that the high condition number for micromagnetic systems is a result of the effects of the exchange field linear operator [87]. To alleviate this problem, we use the projected sparse matrix $C_{ex\perp} = P_{\mathbf{m}_0} C_{ex}$ of the exchange field operator C_{ex}, which represents the discretization of the $(2A/M_s)\nabla^2$ operator in, to construct a sparse preconditioner matrix

$$P = (j\omega B_\perp + \gamma H_{ex\perp}), \tag{6.15}$$

The inverse matrix of preconditioner P^{-1} can be approximately calculated by the incomplete LU decomposition (ILU) [86] or using the block-inverse preconditioner [87]. Multiplying by P^{-1} in both sides of the (6.14), we obtain a preconditioned linear problem

$$P^{-1}(j\omega B_\perp + \gamma A_\perp)\tilde{\mathbf{v}} = \gamma P^{-1}\tilde{\mathbf{h}}_a.$$

(6.16)

The preconditioned linear system of (6.16) has a significantly reduced condition number and can be solved in a much smaller number of iterations than the original problem of (6.14).
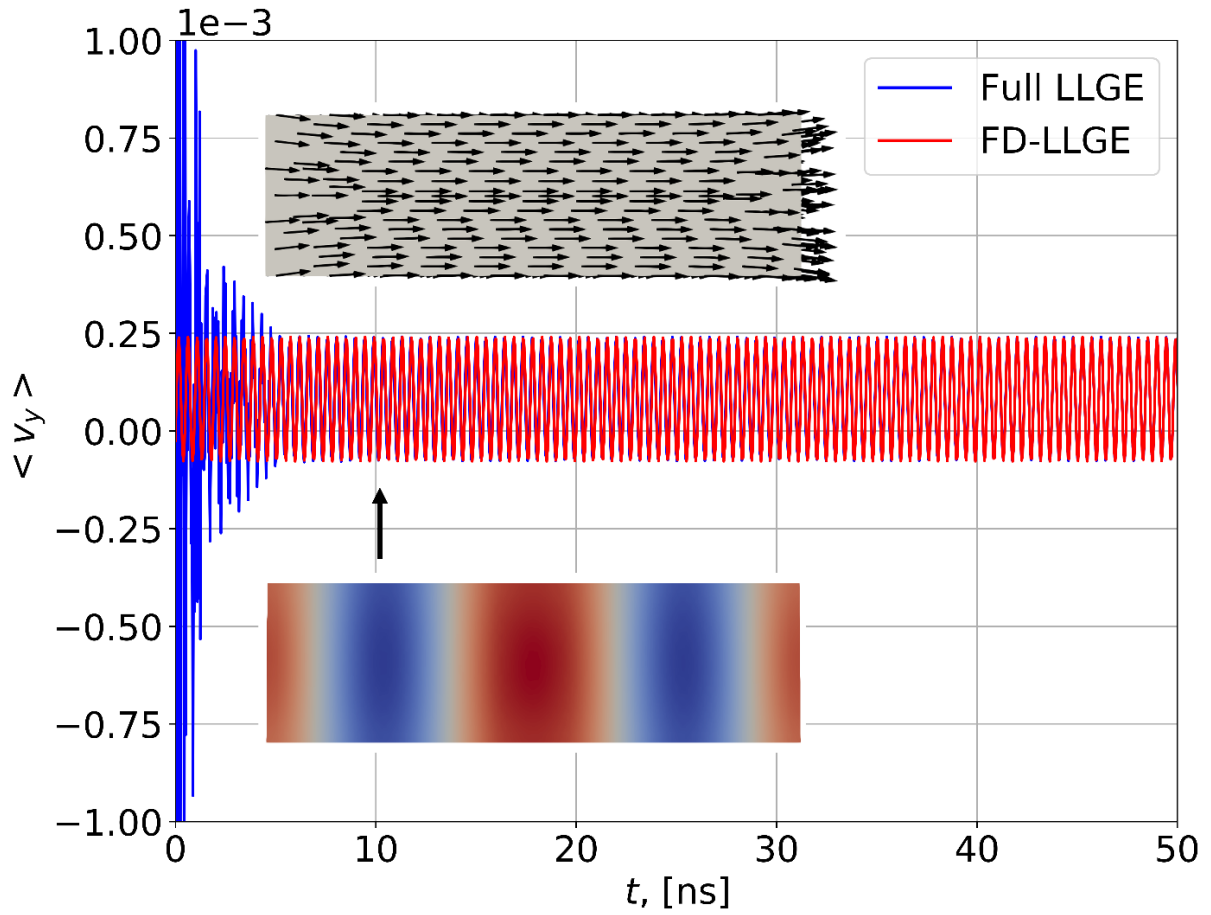

Figure 6.1: Time dynamics of the average magnetization obtained via the full LLG equation and FD-LLG equation solvers for $L = 100\,\text{nm}$, $\alpha = 0.01$. The top inset shows the strip with its magnetization equilibrium state. The bottom inset shows a snapshot of v_y at $t = 10\,\text{ns}$.

6.3 Linear solver results

We implemented the FD-LLG equation solver as a part of the FEM based micromagnetic simulator FastMag with tetrahedral elements [19]. The effective fields are computed as for the general LLG equation. The linear system of equations (6.16) is solved using the GMRES algorithm with the relative error of 10^{-8}. The preconditioner is based on the ILU0 and ILUk flavors of the ILU preconditioner using the sparse matrix P of (6.15) [86]. The results are shown for a magnetic strip of width $w = 30\,\text{nm}$, thickness $h = 1\,\text{nm}$, and length $L > w$ ranging from $100\,\text{nm}$ to $10\,\mu\text{m}$. The material parameters are $M_s = 800\,\text{emu/cm}^3$, $A_{ex} = 1\,\mu\text{erg/cm}$, and α ranges from 0.01 to 0.0001. The maximal mesh edge length was chosen as 2 nm to be sufficiently smaller than the exchange length of $\sqrt{A}/M_s = 12.5\,\text{nm}$. The equilibrium magnetization is along the longest direction (see the top inset in Figure 6.1). The magnetization dynamics is excited by a weak applied magnetic field of $\tilde{\mathbf{h}}_a = 50\,\text{Oe}$ confined to the region of $10\,\text{nm}$ near the center of the strip at frequency $f = \omega/(2\pi) = 20\,\text{GHz}$. The results were obtained on an Intel Core i9-9900K CPU.

Figure 6.1 demonstrates the validity of the solver by comparing the results obtained via the FD-LLG equation (6.16) and via the original LLG equation (6.1). The figure shows the space averaged y-component of $\mathbf{v}$ for $L = 100\,\text{nm}$. The number of mesh vertices for this case was 3,927. The number of iterations based on the ILU0 preconditioner for the FD-LLG equation solver was 57 and the computational time was 3 seconds. The initial, i.e., early time dynamics, is different, which is because for the non-linear solver there are initial non-linear effects. The later time dynamics is described by the FD-LLG equation solver accurately. A snapshot of v_y at $t = 10\,\text{ns}$ shown in the bottom inset of Figure 6.1 demonstrates a standing spin wave pattern.
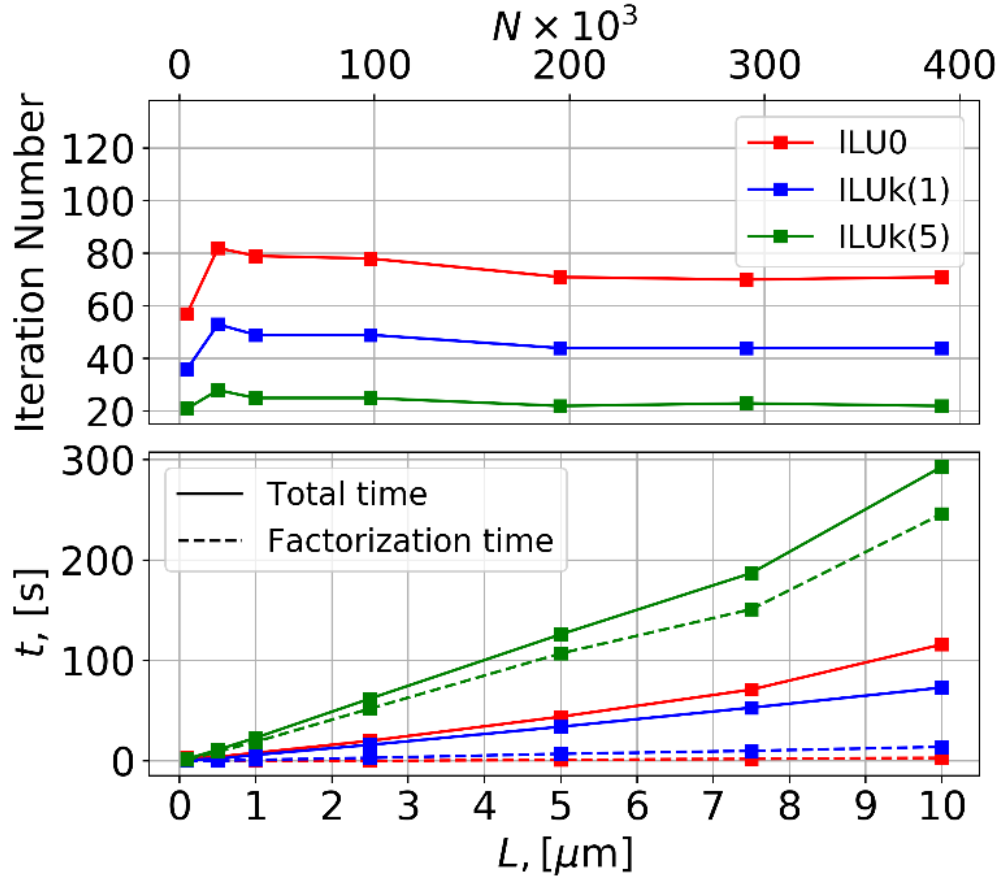
Figure 6.2: Size dependence of the linear solver iteration number and computational time when using different preconditioners for $\alpha = 0.01$.

Figure 6.2 demonstrates the computational performance of the FD-LLG equation solver by showing the number of iterations and computational time as a function of the strip length L and the corresponding number of tetrahedral mesh vertices N. The results are shown for the preconditioned formulation of (6.16). It is evident that the non-preconditioned solver requires many iterations, whereas using preconditioners leads to a significant reduction of the number of iterations. The ILUk preconditioners perform better than ILU0 in terms of having a smaller number of iterations, but they have a higher cost per iterations. Overall, we find that ILUk with $k = 1$ has the best performance in terms of the computational time. Overall, the solver performance is good, and it allows addressing large scale computational problems. We note that the solving the linear

system without using a preconditioner, i.e., (6.14), requires a large number of iterations, e.g., 1,952 iterations for the $L=100\,\text{nm}$ case, which makes such a solver impractical. Therefore, using the preconditioned system of (6.16) is critical.
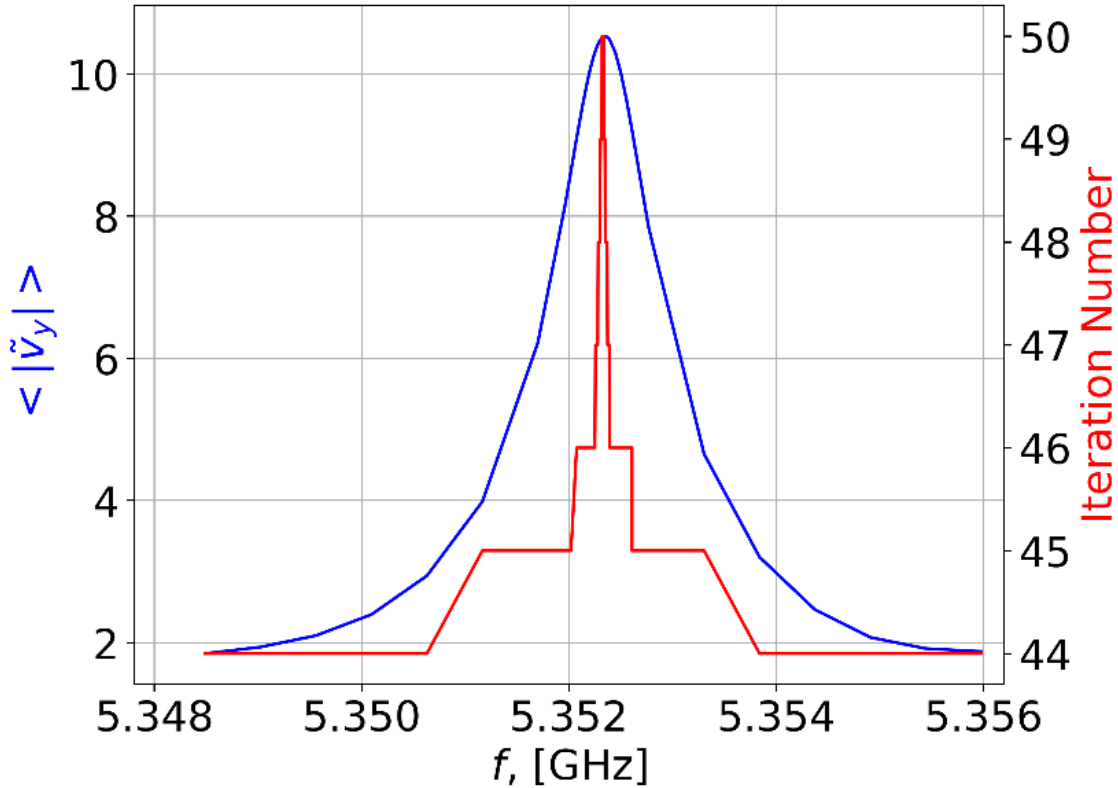
Figure 6.3: Frequency dependence of the magnetization deviation magnitude for $L=100\,\text{nm}$ and $\alpha=0.0001$.

Finally, Fig. 6.3 shows the space averaged magnitude $<|\tilde{v}_y|>$ as a function of frequency f. One can see that the solution $<|\tilde{v}_y|>$ exhibits a strong resonance response, with the resonant frequency related to the resonant standing spin wave excitation. The figure also shows the number of iterations with ILUk with $k=1$ preconditioner. The number of iterations increases at the resonant frequency, but this increase is modest, which demonstrates a good performance even when the excitation frequency is close to the resonant frequency.

6.4 Summary

In summary, we present a FD-LLG equation solver that allows obtaining the magnetization dynamics solutions driven by weak time harmonic excitations. The formulation is based on linearizing the original non-linear time domain LLG equation and assuming a single frequency excitation and solution, which results in a single linear system of equations for the complex magnetization deviation around the magnetization equilibrium state. The linear system is preconditioned by a sparse preconditioner that allows significantly reducing the number of iterations and computational time required for its solution. We note that once the solutions for $\tilde{\mathbf{v}}$ is obtained, the time domain solution $\mathbf{v}$ is found for all time via (6.13).

Assuming a small number of linear iterations for solving (6.16), the FD-LLG equation solver provides a much more efficient approach than solving the original non-linear LLG equation for finding solutions in the linear regime. If the excitation is given by multiple frequencies, e.g., by a pulse, then multiple frequency domain solutions can be combined via the Fourier transform. The results are shown for real-valued frequencies, but solutions can also be obtained for complex-valued frequencies, which can provide insights into the magnetization dynamics behavior. The FD-LLG equation solver is implemented in the FEM framework, and it can also be extended to finite difference implementations.

Acknowledgements

Chapter 7

Harmonic balance solver

In the linear FD-LLG equation formulation of Chapter 6, we only keep the first order terms in the linearized LLG equation to linearize it. Linear response is obtained when the excitation is by a weak time-harmonic field. When the time-harmonic excitation is stronger, non-linear effects become important. For example, an excitation of a given frequency may result in a generation of higher order harmonics. Non-linear effects are accounted for in the general non-linear LLG equation (1.4), but using the LLG equation may be not efficient numerically and may make understanding physical mechanisms complicated. In this section, we consider the magnetization response to a time-harmonic excitation in the regime of "weak" non-linearities, in which the magnetization can be represented in terms of an expansion over a series of higher-order harmonics accounting for higher-harmonic generation phenomena. We refer to the method described next as to Harmonic balance method (HBM). The HBM is related to techniques used to solver for non-linear dynamic excitation in various systems, such as circuit solvers [88].

7.1 Harmonic balance solver

The derivation of HBM starts similarly to the derivation of the linearized LLG equation in Chapter 6 with several important updates. When inserting the expansion of (6.4) in LLG equation (6.1), we keep not only the first-order terms, but also the higher order terms, which gives:

$$\frac{\partial \mathbf{v}}{\partial t} + \gamma(-\Lambda(\mathbf{H}_0)\mathbf{v} + \Lambda(\mathbf{m}_0)\mathbf{h}) - \alpha\Lambda(\mathbf{m}_0)\frac{\partial \mathbf{v}}{\partial t} = -\gamma(\mathbf{v}\times\mathbf{h} + \mathbf{v}\times\mathbf{h}_a + \Lambda(\mathbf{m}_0)\mathbf{h}_a) + \alpha\mathbf{v}\times\frac{\partial \mathbf{v}}{\partial t}, \quad (7.1)$$

where we keep the first-order terms on the left-hand side and other terms on the right-hand side.

We assume an excitation by a time-harmonic driving term, e.g., applied magnetic field at frequency ω:

$$\tilde{\mathbf{h}}_a = h_a e^{j\omega t} + c.c. \tag{7.2}$$

where $c.c.$ denotes the complex conjugate of the first term of the right-hand side. Due to the time periodicity, the solution and the corresponding magnetic field can be expanded via an infinite number of harmonics

$$
\begin{aligned}
\mathbf{v} &= \sum_{n=0} v_n(\mathbf{r}, n\omega) e^{jn\omega t} + c.c. \\
\mathbf{h} &= \sum_{n=0} h_n(\mathbf{r}, n\omega) e^{jn\omega t} + c.c.
\end{aligned} \tag{7.3}
$$

Inserting (7.2) and (7.3) into (7.1) and re-arranging the terms results in the following non-linear equation:

$$
\begin{aligned}
&\sum_n j\omega_n v_n e^{j\omega_n t} + \gamma \left(-\Lambda(\mathbf{H}_0) \sum_n v_n e^{j\omega_n t} + \Lambda(\mathbf{m}_0) \sum_n h_n e^{j\omega_n t} \right) - \alpha\Lambda(\mathbf{m}_0) \sum_n j\omega_n v_n e^{j\omega_n t} = \\
&-\gamma\Lambda(\mathbf{m}_0) h_a e^{j\omega_1 t} \\
&-\gamma \left(\sum_n v_n e^{j\omega_n t} \times \sum_m h_m e^{j\omega_m t} + \sum_n v_n e^{j\omega_n t} \times h_a e^{j\omega_1 t} + \sum_n v_n e^{j\omega_n t} \times h_a^{-1} e^{j\omega_1 t} \right) \\
&+\alpha \sum_n v_n e^{j\omega_n t} \times \sum_m j\omega_m v_m e^{j\omega_m t}.
\end{aligned} \tag{7.4}
$$

From here, we can re-arrange the terms and obtain equations for the coefficients of each n-th order harmonic component, i.e., each exponent with the power of $\omega_n = n\omega$:

$$
\begin{aligned}
&j\omega_n v_n + \gamma \left(\Lambda(\mathbf{H}_0) v_n + \Lambda(\mathbf{m}_0) h_n \right) - \alpha\Lambda(\mathbf{m}_0) j\omega_n v_n = \\
&-\gamma\Lambda(\mathbf{m}_0) h_a \delta_{n1} \\
&-\gamma \left(\sum_m (v_{n-m} \times h_m) + v_{n-1} \times h_a + v_{n+1} \times h_{-a} \right) \\
&+\alpha \sum_m v_{n-m} \times j\omega_m v_m
\end{aligned} \tag{7.5}
$$

This equation can be further multiplied by $P_{\mathbf{m}_0}$ and $\Lambda(\mathbf{m}_0)$ at both sides resulting in

$$(j\omega B_\perp + \gamma A_\perp)v_n =$$
$$\gamma h_a \delta_{n1} + B_\perp \left[-\gamma \left(\sum_m v_{n-m} \times h_m + v_{n-1} \times h_a (1-\delta_{n1}) \right) + \alpha \sum_m v_{n-m} \times j\omega_m v_m \right]. \tag{7.6}$$

Note that the left-hand side operator here is the same as the left-hand side of the linearized LLG equation (6.10), whereas the right-hand side contains the non-linear coupling between the coefficients of all harmonics. Under weak excitations the non-linear coupling can be neglected, which results in a linear equation only for v_1 identical to (6.10), and no higher-order harmonics generation. For stronger excitations, the non-linear coupling becomes important. This understanding indicates that the non-linear system of (7.6) can be solved iteratively.

Let us denote the iteration number as i and the variable v_n^i for n-th order at i-th iteration. We can initialize the iterations by assigning $v_n^0 = 0$ for all n. We, then, proceed with the iterations via

$$(j\omega B_\perp + \gamma A_\perp)v_n^{i+1} =$$
$$\gamma h_a \delta_{n1} + B_\perp \left[-\gamma \left(\sum_m v_{n-m}^i \times h_m^i + v_{n-1}^i \times h_a (1-\delta_{n1}) \right) + \alpha \sum_m v_{n-m}^i \times j\omega_m v_m^i \right], \tag{7.7}$$

where, at each iteration $i+1$, we solve a set of linear equations for v_n^{i+1}. In each such equation, we have a linear operator in the left-hand side that is similar to the linear operator in (6.10) but it is defined for the frequency ω_n. The right-hand side for each linear problem of (7.7) is known based on the previous iteration. The solution proceeds similar to that of the linearized LLG equation in Chapter 6, including the use of the same preconditioner.

7.2 Two harmonics case

The HBM in general includes an infinite number of harmonics. Often, however, only a finite number of such harmonics are strongly excited. In this section we show a special case with only

two harmonics $n = 1$ and $n = 2$, which exemplifies the procedure of HBM. We start the iteration

process with $i = 0$, where

$$\begin{cases} v_1^0 = 0 \\ v_2^0 = 0 \end{cases}.$$ (7.8)

At $i = 1$, from (7.7) we have

$$\begin{cases} (j\omega B_\perp + \gamma A_\perp)v_1^1 = \gamma h_a \\ (j\omega B_\perp + \gamma A_\perp)v_2^1 = 0 \end{cases}.$$ (7.9)

Note that in (7.9), the first equation is identical to the linear solver equation (6.14), and the second

equation has a trivial solution of $v_2^1 = 0$. Consequently, at $i = 1$, only v_1 has an update, which has

a meaning of a solution that would be obtained if the linearization assumption of Chapter 6 is met.

Next at $i = 2$, noting that $v_2^1 = 0$, we have

$$\begin{cases} (j\omega B_\perp + \gamma A_\perp)v_1^2 = \gamma h_a \\ (j\omega B_\perp + \gamma A_\perp)v_2^2 = B_\perp \left[(v_1^1 \times h_1^1 + v_1^1 \times h_a) + j\alpha(v_1^1 \times \omega_1 v_1^1) \right] \end{cases}.$$ (7.10)

Note that the first equation in (7.10) is identical to the first equation in (7.9), which indicates that

$v_1^1 = v_1^2$ and only v_2 at $i = 2$ has an update. Continuing this procedure, one can find that at odd i

iterations, only v_1 has an update, and at even i iterations, only v_2 has an update. This process can

be done iteratively until both harmonics converge with a tolerance ε:

$$\frac{|< v_n^i - v_n^{i-1} >|}{|< v_n^{i-1} >|} < \varepsilon, \ n = 1, 2.$$ (7.11)

7.3 Harmonic balance solver results

In this section, we show results of the HBM solver for several cases, including a single domain

model and a magnetic dis with a more complicated dynamics. The HBM solver used to obtain

the results is based on the two-order case discussed in Chapter 6.4.2.

7.3.1 Single-spin model results

We first consider a macro spin model, where only a uniaxial anisotropy field in the z-direction is present. The equilibrium state is aligned in the z-direction. To obtain an excitation with an in-plane applied harmonic field, we need to break the symmetry by a small tilt of the equilibrium state. We use an equilibrium state $\mathbf{m}_0$ to have a $1°$ angle with respect to the z-axis. We run LLG equation and HBM solvers, with the following magnetic parameters: $K_U = 0.611 \mathrm{Merg/cm}^3, M_s = 2000 \, \mathrm{emu/cm}^3$, and $\alpha = 10^{-5}$. The applied field is in the x-direction, has a magnitude of 50 Oe, and it is a sine function of time with frequency of $\omega_{eig}^r / 2$, where $\omega_{eig}^r = 2\gamma K_U / M_s(1+\alpha^2)$ is the real part of the eigenfrequency, i.e., the ferromagnetic resonance frequency. The LLG equation simulation is carried out for 10,000 ns. The results for the HBM solver are obtained by solving (7.7) iteratively and using (7.3) to find the time dependence of the magnetization deviation at the same time steps as for the LLG equation solver.
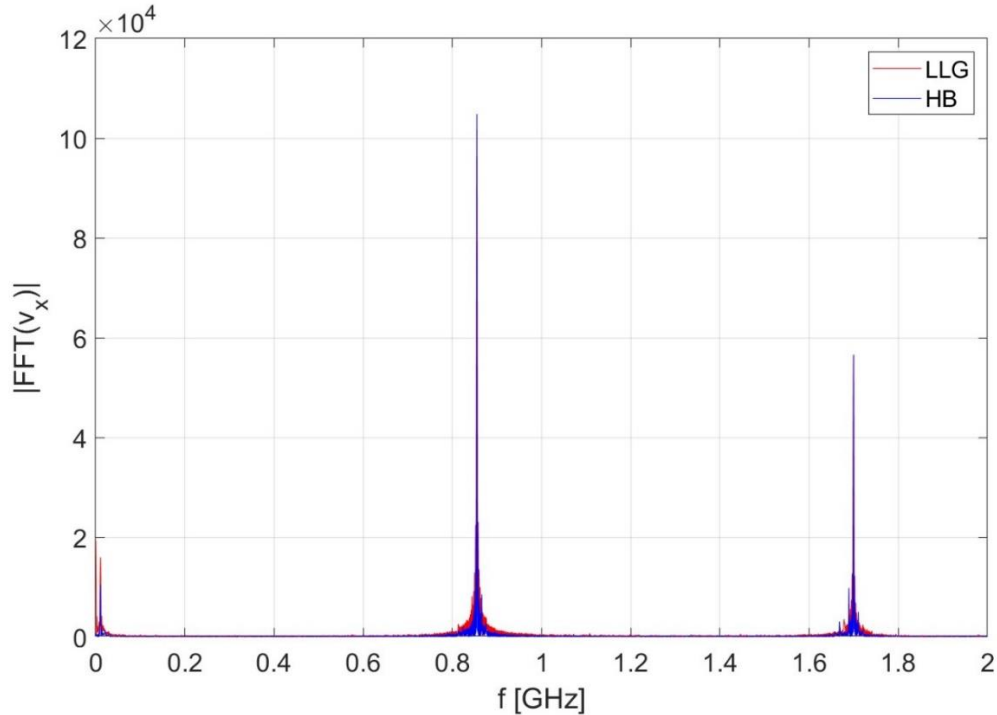

Figure 7.1: Fourier transform spectrum of LLG simulation and HBM results for macro spin model.

Figure 7.1 shows the Fourier transform spectrum for both LLG equation and HBM solver results. We can see that both harmonics at $\omega_1 = \omega_{eig}^r / 2$ and $\omega_2 = \omega_{eig}^r$ are excited. Since ω_2 is near the complex eigenfrequency ω_{eig}, the second harmonic is excited strongly. Also, the results in Figure 7.1 show a good agreement between the LLG equation and HBM solver results. The HBM solver required 3 non-linear iterations for 10^{-16} error tolerance.
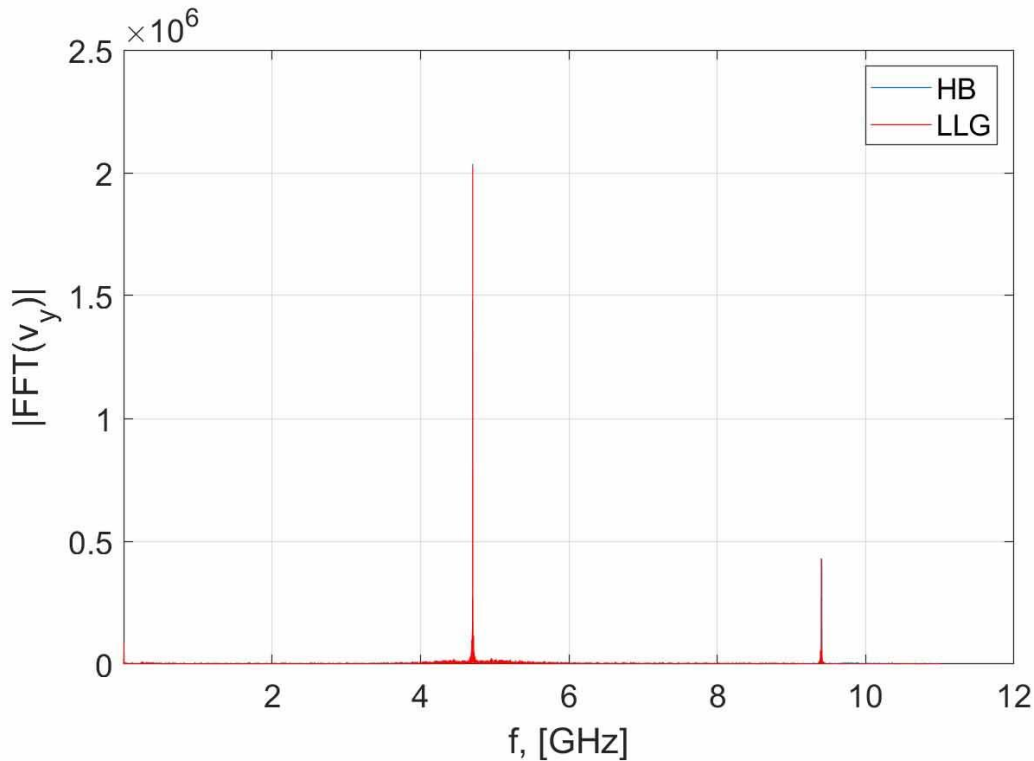
Figure 7.2: Fourier transform spectrum of HBM solutions and LLG results.

7.3.2 Micromagnetic results for a magnetic disk

Now, we show the operation of the HBM solver for a magnetic disk with perpendicular anisotropy of $K_U = 6.11\,\mathrm{Merg/cm}^3$, with a small tilted 5 degree easy axis to perpendicular direction, magnetization saturation $M_s = 960\,\mathrm{emu/cm}^3$, diameter $D = 20\,\mathrm{nm}$, thickness $h = 1\,\mathrm{nm}$, and damping factor $\alpha = 8 \times 10^{-5}$. We use an in-plane time-harmonic applied field in the x-direction,

which has a magnitude of 5 Oe and frequency of $\omega = \omega_1' / 2$, where $\omega_1' = 2\pi f_1'$ and $f_1' = 9.41 \text{GHz}$ is the real part of first eigenfrequency.

We run the LLG equation simulations for 6000 ns and calculate the deviation **v** from harmonic balance solver for both LLG equation simulation and HBM solver. Figure 7.2 shows the Fourier transform of the HBM and LLG equation solutions using the time series from 5000 to 6000 ns. We find that the second harmonics is again excited and the HBM and LLG results have a great agreement. The HBM results required 3 iterations for a 10^{-9} convergence tolerance, which was 13 times faster than running the LLG simulations.

7.4 Summary

In summary, we introduced a HBM for solving the LLG equation under the assumptions of weak non-linearities to study the non-linear magnetization dynamics driven by a time-harmonic excitation. In HBM, the magnetization is represented in terms of a series of harmonic components, which correspond to powers of the driving field frequency. The LLG equation is reduced into a set of coupled equations for the coefficients of these harmonics. The equation can then be solved the iteratively with a small number of iterations. Numerical results demonstrate that the HBM gives accurate solutions, which match the direct LLG solution. Obtaining solutions via the HBM is much faster than using direct LLG equation solvers.

Acknowledgements

CHAPTER 8

Conclusion

This dissertation introduced algorithms to study the micromagnetic systems based on the L-LLG equation, including cases driven by applied fields and ST. We constructed an eigenvalue framework to study the switching behavior of ST-driven devices, which can be used to predict the switching current density and switching time of STT-MRAM as well as solve the L-LLG equation based on the eigen solutions of the system. This method is extended to optimize the current density spatial distribution and thus reduce the total critical current in MRAM elements. We found that the optimized current density spatial distribution can significantly increase the efficiency, viz., the ratio between energy barrier and critical current, especially for larger MRAM cells. The eigenvalue framework facilitates the design of new MRAM devices, provides important insights into dynamics in such systems, and allows solving several difficulties in their modeling, such as extracting the switching current in MRAM and understanding switching mechanisms. We also used the eigenvalue framework to construct a FP equation, which can be used to study WERs in MRAM. This approach can be generalized to account for the micromagnetic interactions and STT, which is useful for practical applications.

The dissertation also introduced an FEM-based FD-LLG equation solver, which allows solving for the magnetization dynamics in the linear regime driven by time harmonic applied fields. The solver is based on using the L-LLG under the assumption of a single frequency excitation and magnetization dynamic behavior. The FD-LLG solver is based on solving a linear system for the complex magnetization amplitude. The linear equation is solved by an iterative solver, and we constructed an efficient preconditioner to result in a small number of iterations. In

the linear regime, using the developed FD-LLG solver is much more efficient than using the original time-domain LLG.

We, then, introduced a HBM solver, which formulates a system of equations for finding the excitation coefficients of an infinite number of harmonics of different orders, which correspond to higher-order frequencies of the driving frequency. The solution is obtained via a rapidly convergent iterative procedure, in which a set of linear solutions are obtained at each iteration step. In the linear or weakly non-linear regimes, the introduced linear or HBM solvers allows obtaining the solutions much faster and with more physical insights than the original non-linear time dependent LLG equation solvers.

REFERENCES

[1]   W. F. Brown, *Micromagnetics* (interscience publishers, 1963).

[2]   L. Landau and E. Lifshitz, *On the Theory of the Dispersion of Magnetic Permeability in Ferromagnetic Bodies*, in *Perspectives in Theoretical Physics* (Elsevier, 1992).

[3]   T. L. Gilbert, *Classics in Magnetics A Phenomenological Theory of Damping in Ferromagnetic Materials*, IEEE Trans. Magn. **40**, 3443 (2004).

[4]   S. Sachdev, *Handbook of Magnetism and Advanced Magnetic Materials* (Citeseer, 2006).

[5]   J. D. Jackson and R. F. Fox, *Classical Electrodynamics* (Wiley, New York, 1999).

[6]   Shaojing Li, B. Livshitz, and V. Lomakin, *Graphics Processing Unit Accelerated O(N) Micromagnetic Solver*, IEEE Trans. Magn. **46**, 2373 (2010).

[7]   M. Sato and Y. Ishii, *Simple and Approximate Expressions of Demagnetizing Factors of Uniformly Magnetized Rectangular Rod and Cylinder*, J. Appl. Phys. **66**, 983 (1989).

[8]   K. M. Krishnan, *Fundamentals and Applications of Magnetic Materials* (Oxford University Press, 2016).

[9]   J. E. Miltat and M. J. Donahue, *Handbook of Magnetism and Advanced Magnetic Materials, Volume Micromagnetism* (Wiley London, 2007).

[10]   I. Volvach, *Micromagnetic Modeling and Analysis of Magnetic Tunnel Junctions for Spintronics Applications*, PhD thesis, University of California, San Diego, 2021.

[11]   M. d'Aquino, *Nonlinear Magnetization Dynamics in Thin-Films and Nanoparticles*, PhD thesis, Universit`a degli studi di Napoli Federico II, Italy, 2004.

[12]   M. A. Ruderman and C. Kittel, *Indirect Exchange Coupling of Nuclear Magnetic Moments by Conduction Electrons*, Phys. Rev. **96**, 99 (1954).

[13]   D. V. Berkov and N. L. Gorn, *Stochastic Dynamic Simulations of Fast Remagnetization Processes: Recent Advances and Applications*, J. Magn. Magn. Mater. **290**–**291**, 442 (2005).

[14]   D. A. Garanin, *Fokker-Planck and Landau-Lifshitz-Bloch Equations for Classical Ferromagnets*, Phys. Rev. B **55**, 3050 (1997).

[15]   A. V Khvalkovskiy, D. Apalkov, S. Watts, R. Chepulskii, R. S. Beach, A. Ong, X. Tang, A. Driskill-Smith, W. H. Butler, P. B. Visscher, D. Lottis, E. Chen, V. Nikitin, and M. Krounbi, *Basic Principles of STT-MRAM Cell Operation in Memory Arrays*, J. Phys. D.

Appl. Phys. **46**, 74001 (2013).

[16]   G. Henkelman, B. P. Uberuaga, and H. Jónsson, *A Climbing Image Nudged Elastic Band Method for Finding Saddle Points and Minimum Energy Paths*, J. Chem. Phys. **113**, 9901 (2000).

[17]   P. Maragakis, S. A. Andreev, Y. Brumer, D. R. Reichman, and E. Kaxiras, *Adaptive Nudged Elastic Band Approach for Transition State Calculation*, J. Chem. Phys. **117**, 4651 (2002).

[18]   R. Dittrich, T. Schrefl, A. Thiaville, J. Miltat, V. Tsiantos, and J. Fidler, *Comparison of Langevin Dynamics and Direct Energy Barrier Computation*, J. Magn. Magn. Mater. **272– 276**, 747 (2004).

[19]   R. Chang, S. Li, M. V. Lubarda, B. Livshitz, and V. Lomakin, *FastMag: Fast Micromagnetic Simulator for Complex Magnetic Structures (Invited)*, J. Appl. Phys. **109**, 1 (2011).

[20]   M. V. Lubarda, *Micromagnetic Modeling and Analysis for Memory and Processing Applications*, PhD thesis, University of California, San Diego, 2012.

[21]   M. G. Larson and F. Bengzon, *The Finite ElementMethod: Theory, Implementation, and Applications* (Springer, 2013).

[22]   G. Binasch, P. Grünberg, F. Saurenbach, and W. Zinn, *Enhanced Magnetoresistance in Layered Magnetic Structures with Antiferromagnetic Interlayer Exchange*, Phys. Rev. B **39**, 4828 (1989).

[23]   A. Fert, *Nobel Lecture: Origin, Development, and Future of Spintronics*, Rev. Mod. Phys. **80**, 1517 (2008).

[24]   J. C. Slonczewski, *Current-Driven Excitation of Magnetic Multilayers*, J. Magn. Magn. Mater. **159**, L1 (1996).

[25]   L. Berger, *Emission of Spin Waves by a Magnetic Multilayer Traversed by a Current*, Phys. Rev. B **54**, 9353 (1996).

[26]   J. Xiao, A. Zangwill, and M. D. Stiles, *Macrospin Models of Spin Transfer Dynamics*, Phys. Rev. B **72**, 1 (2005).

[27]   J. E. Hirsch, *Spin Hall Effect*, Phys. Rev. Lett. **83**, 1834 (1999).

[28]   Y. A. Bychkov and É. I. Rashba, *Properties of a 2D Electron Gas with Lifted Spectral Degeneracy*, JETP Lett. **39**, 78 (1984).

[29]   P. M. Haney, H. W. Lee, K. J. Lee, A. Manchon, and M. D. Stiles, *Current Induced Torques and Interfacial Spin-Orbit Coupling: Semiclassical Modeling*, Phys. Rev. B **87**, 1 (2013).

[30] L. Liu, O. J. Lee, T. J. Gudmundsen, D. C. Ralph, and R. A. Buhrman, *Current-Induced Switching of Perpendicularly Magnetized Magnetic Layers Using Spin Torque from the Spin Hall Effect*, Phys. Rev. Lett. **109**, 1 (2012).

[31] N. Perez, L. Torres, and E. Martinez-Vecino, *Micromagnetic Modeling of Dzyaloshinskii-Moriya Interaction in Spin Hall Effect Switching*, IEEE Trans. Magn. **50**, 2 (2014).

[32] A. V. Khvalkovskiy, D. Apalkov, S. Watts, R. Chepulskii, R. S. Beach, A. Ong, X. Tang, A. Driskill-Smith, W. H. Butler, P. B. Visscher, D. Lottis, E. Chen, V. Nikitin, and M. Krounbi, *Basic Principles of STT-MRAM Cell Operation in Memory Arrays*, J. Phys. D. Appl. Phys. **46**, 074001 (2013).

[33] M. Julliere, *Tunneling between Ferromagnetic Films*, Phys. Lett. A **54**, 225 (1975).

[34] T. Miyazaki and N. Tezuka, *Giant Magnetic Tunneling Effect in Fe/Al₂O₃/Fe Junction*, J. Magn. Magn. Mater. **139**, L231 (1995).

[35] W. H. Butler, X.-G. Zhang, T. C. Schulthess, and J. M. MacLaren, *Spin-Dependent Tunneling Conductance of Fe/MgO/Fe Sandwiches*, Phys. Rev. B **63**, 054416 (2001).

[36] S. S. P. Parkin, C. Kaiser, A. Panchula, P. M. Rice, B. Hughes, M. Samant, and S.-H. Yang, *Giant Tunnelling Magnetoresistance at Room Temperature with MgO (100) Tunnel Barriers*, Nat. Mater. **3**, 862 (2004).

[37] S. Yuasa, A. Fukushima, H. Kubota, Y. Suzuki, and K. Ando, *Giant Tunneling Magnetoresistance up to 410% at Room Temperature in Fully Epitaxial Co/MgO/Co Magnetic Tunnel Junctions with Bcc Co(001) Electrodes*, Appl. Phys. Lett. **89**, 042505 (2006).

[38] S. Bhatti, R. Sbiaa, A. Hirohata, H. Ohno, S. Fukami, and S. N. Piramanayagam, *Spintronics Based Random Access Memory: A Review*, Mater. Today **20**, 530 (2017).

[39] L. Schwee, *Proposal on Cross-Tie Wall and Bloch Line Propagation in Thin Magnetic Films*, IEEE Trans. Magn. **8**, 405 (1972).

[40] M. Hosomi, H. Yamagishi, T. Yamamoto, K. Bessho, Y. Higo, K. Yamane, H. Yamada, M. Shoji, H. Hachino, C. Fukumoto, H. Nagao, and H. Kano, *A Novel Nonvolatile Memory with Spin Torque Transfer Magnetization Switching: Spin-Ram*, in *IEEE InternationalElectron Devices Meeting, 2005. IEDM Technical Digest.*

[41] R. Takemura, T. Kawahara, K. Miura, J. Hayakawa, S. Ikeda, Y. M. Lee, R. Sasaki, Y. Goto, K. Ito, T. Meguro, F. Matsukura, H. Takahashi, H. Matsuoka, and H. Ohno, *2Mb SPRAM Design: Bi-Directional Current Write and Parallelizing-Direction Current Read Schemes Based on Spin-Transfer Torque Switching*, in *2007 IEEE International Conference on Integrated Circuit Design and Technology*.

[42] J. M. Slaughter, N. D. Rizzo, J. Janesky, R. Whig, F. B. Mancoff, D. Houssameddine, J. J. Sun, S. Aggarwal, K. Nagel, S. Deshpande, S. M. Alam, T. Andre, and P. LoPresti, *High Density ST-MRAM Technology (Invited)*, in *2012 International Electron Devices Meeting*.

[43] J. J. Sun, M. DeHerrera, B. Hughes, S. Ikegawa, H. K. Lee, F. B. Mancoff, K. Nagel, G. Shimon, S. M. Alam, D. Houssameddine, and S. Aggarwal, *Commercialization of 1Gb Standalone Spin-Transfer Torque MRAM*, in *2021 IEEE International Memory Workshop*.

[44] I. M. Miron, K. Garello, G. Gaudin, P. J. Zermatten, M. V. Costache, S. Auffret, S. Bandiera, B. Rodmacq, A. Schuhl, and P. Gambardella, *Perpendicular Switching of a Single Ferromagnetic Layer Induced by In-Plane Current Injection*, Nature **476**, 189 (2011).

[45] K. Garello, F. Yasin, S. Couet, L. Souriau, J. Swerts, S. Rao, S. Van Beek, W. Kim, E. Liu, S. Kundu, D. Tsvetanova, K. Croes, N. Jossart, E. Grimaldi, M. Baumgartner, D. Crotti, A. Fumemont, P. Gambardella, and G. S. Kar, *SOT-MRAM 300MM Integration for Low Power and Ultrafast Embedded Memories*, in *2018 IEEE Symposium on VLSI Circuits*.

[46] N. Sato, G. A. Allen, W. P. Benson, B. Buford, A. Chakraborty, M. Christenson, T. A. Gosavi, P. E. Heil, N. A. Kabir, B. J. Krist, K. P. O'Brien, K. Oguz, R. R. Patil, J. Pellegren, A. K. Smith, E. S. Walker, P. J. Hentges, M. V. Metz, M. Seth, B. Turkot, C. J. Wiegand, H. J. Yoo, and I. A. Young, *CMOS Compatible Process Integration of SOT-MRAM with Heavy-Metal Bi-Layer Bottom Electrode and 10ns Field-Free SOT Switching with STT Assist*, in *2020 IEEE Symposium on VLSI Technology*.

[47] Online materials: *https:// www.mram-info.com/isi-ships-its-first-sot-mram-tester-system*.

[48] S. Ikeda, K. Miura, H. Yamamoto, K. Mizunuma, H. D. Gan, M. Endo, S. Kanai, J. Hayakawa, F. Matsukura, and H. Ohno, *A Perpendicular-Anisotropy CoFeB–MgO Magnetic Tunnel Junction*, Nat. Mater. **9**, 721 (2010).

[49] R. Sbiaa, S. Y. H. Lua, R. Law, H. Meng, R. Lye, and H. K. Tan, *Reduction of Switching Current by Spin Transfer Torque Effect in Perpendicular Anisotropy Magnetoresistive Devices (Invited)*, J. Appl. Phys. **109**, 07C707 (2011).

[50] D. Apalkov, S. Watts, A. Driskill-Smith, E. Chen, Z. Diao, and V. Nikitin, *Comparison of Scaling of In-Plane and Perpendicular Spin Transfer Switching Technologies by Micromagnetic Simulation*, IEEE Trans. Magn. **46**, 2240 (2010).

[51] D. Apalkov, B. Dieny, and J. M. Slaughter, *Magnetoresistive Random Access Memory*, Proc. IEEE **104**, 1796 (2016).

[52] G. D. Chaves-O'Flynn, G. Wolf, J. Z. Sun, and A. D. Kent, *Thermal Stability of Magnetic States in Circular Thin-Film Nanomagnets with Large Perpendicular Magnetic Anisotropy*, Phys. Rev. Appl. **4**, 24010 (2015).

[53] T. Devolder, A. Le Goff, and V. Nikitin, *Size Dependence of Nanosecond-Scale Spin-*

Torque Switching in Perpendicularly Magnetized Tunnel Junctions, Phys. Rev. B **93**, 1 (2016).

[54] I. Volvach, J. G. Alzate, Y.-J. Chen, A. J. Smith, D. L. Kencke, and V. Lomakin, *Thermal Stability and Magnetization Switching in Perpendicular Magnetic Tunnel Junctions*, Appl. Phys. Lett. **116**, 192408 (2020).

[55] W. H. Butler, T. Mewes, C. K. A. Mewes, P. B. Visscher, W. H. Rippard, S. E. Russek, and R. Heindl, *Advances in Magnetics Switching Distributions for Perpendicular Spin-Torque Devices Within the Macrospin Approximation*, IEEE Trans. Magn. **48**, 4684 (2012).

[56] Y. Xie, B. Behin-Aein, and A. W. Ghosh, *Fokker-Planck Study of Parameter Dependence on Write Error Slope in Spin-Torque Switching*, IEEE Trans. Electron Devices **64**, 319 (2017).

[57] L. R. Walker, *Magnetostatic Modes in Ferromagnetic Resonance*, Phys. Rev. **105**, 390 (1957).

[58] A. Aharoni, *Exchange Resonance Modes in a Ferromagnetic Sphere*, J. Appl. Phys. **69**, 7762 (1991).

[59] M. d'Aquino, C. Serpico, G. Miano, and C. Forestiere, *A Novel Formulation for the Numerical Computation of Magnetization Modes in Complex Micromagnetic Systems*, J. Comput. Phys. **228**, 6130 (2009).

[60] M. d'Aquino, *Computation of Magnetization Normal Oscillation Modes in Complex Micromagnetic Systems*, IFAC Proc. Vol. **45**, 2 (2012).

[61] F. Bruckner, M. d'Aquino, C. Serpico, C. Abert, C. Vogler, and D. Suess, *Large Scale Finite-Element Simulation of Micromagnetic Thermal Noise*, J. Magn. Magn. Mater. **475**, 408 (2019).

[62] A. Baker, M. Beg, G. Ashton, M. Albert, D. Chernyshenko, W. Wang, S. Zhang, M. A. Bisotti, M. Franchin, C. L. Hu, R. Stamps, T. Hesjedal, and H. Fangohr, *Proposal of a Micromagnetic Standard Problem for Ferromagnetic Resonance Simulations*, J. Magn. Magn. Mater. **421**, 428 (2017).

[63] Z. Lin and M. Kostylev, *A Rigorous Two-Dimensional Model for the Stripline Ferromagnetic Resonance Response of Metallic Ferromagnetic Films*, J. Appl. Phys. **117**, (2015).

[64] P. Abdipour, A. N. Askarpour, and A. Alu, *Efficient Analysis of Wave Propagation in Metasurface Arrays Based on Eigenvalue Perturbation*, IEEE Trans. Antennas Propag. **69**, 2706 (2021).

[65] K. Munira and P. B. Visscher, *Calculation of Energy-Barrier Lowering by Incoherent*

Switching in Spin-Transfer Torque Magnetoresistive Random-Access Memory, J. Appl. Phys. **117**, (2015).

[66] E. S. Levitin and B. T. Polyak, *Constrained Minimization Methods*, USSR Comput. Math. Math. Phys. **6**, 1 (1966).

[67] R. B. Lehoucq, D. C. Sorensen, and C. Yang, *ARPACK Users' Guide: Solution of Large-Scale Eigenvalue Problems with Implicitly Restarted Arnoldi Methods* (SIAM, 1998).

[68] C. F. Curtiss and J. O. Hirschfelder, *Integration of Stiff Equations*, Proc. Natl. Acad. Sci. **38**, 235 (1952).

[69] P. Henrici, *Discrete Variable Methods in Ordinary Differential Equations* (Wiely, New York, 1962).

[70] S. Ikeda, H. Sato, H. Honjo, E. C. I. Enobio, S. Ishikawa, M. Yamanouchi, S. Fukami, S. Kanai, F. Matsukura, T. Endoh, and H. Ohno, *Perpendicular-Anisotropy CoFeB-MgO Based Magnetic Tunnel Junctions Scaling down to 1X Nm*, in *2014 IEEE International Electron Devices Meeting*.

[71] X. Zhao, Y. Liu, D. Zhu, M. Sall, X. Zhang, H. Ma, J. Langer, B. Ocker, S. Jaiswal, G. Jakob, M. Kläui, W. Zhao, and D. Ravelosona, *Spin–Orbit Torque Driven Multi-Level Switching in He + Irradiated W–CoFeB–MgO Hall Bars with Perpendicular Anisotropy*, Appl. Phys. Lett. **116**, 242401 (2020).

[72] Gary Matthew Wysin, *Magnetic Excitations and Geometric Confinement: Theory and Simulationsle* (IOP Publishing, 2015).

[73] U. Roy, D. L. Kenckeb, T. Pramanik, L. F. Registera, and S. K. Banerjee, *Write Error Rate in Spin-Transfer-Torque Random Access Memory Including Micromagnetic Effects,* in *2015 73rd Annual Device Research Conference*.

[74] W. H. Butler, T. Mewes, C. K. A. Mewes, P. B. Visscher, W. H. Rippard, S. E. Russek, and R. Heindl, *Switching Distributions for Perpendicular Spin-Torque Devices within the Macrospin Approximation*, IEEE Trans. Magn. **48**, 4684 (2012).

[75] J. Z. Sun, T. S. Kuan, J. A. Katine, and R. H. Koch, *Spin Angular Momentum Transfer in a Current-Perpendicular Spin-Valve Nanomagnet*, Quantum Sensing Nanophotonic Devices **5359**, 445 (2004).

[76] V. Lomakin, X. Wang, M. Kuteifan, I. Volvach, and M. Menarini, *Fast Codes for Modeling the Magnetization Dynamics in Magnetic Nanostructures*, in *2018 International Conference on Electromagnetics in Advanced Applications*.

[77] U. Roy, T. Pramanik, L. F. Register, and S. K. Banerjee, *Write Error Rate of Spin-Transfer-Torque Random Access Memory Including Micromagnetic Effects Using Rare Event*

Enhancement, IEEE Trans. Magn. **52**, (2016).

[78] U. Roy, T. Pramanik, S. Roy, A. Chatterjee, L. F. Register, and S. K. Banerjee, *Machine Learning for Statistical Modeling: The Case of Perpendicular Spin-Transfer-Torque Random Access Memory*, ACM Trans. Des. Autom. Electron. Syst. **26**, 1 (2021).

[79] M. R. R. Tabar, *Kramers–Moyal Expansion and Fokker–Planck Equation*, Underst. Complex Syst. **19**, 1 (2019).

[80] M. Loeve, *Probability Theory* (Courier Dover Publications, 2017).

[81] H. P. Langtangen and A. Logg, *Solving PDEs in Python: The FEniCS Tutorial*, Vol. I (Springer, 2017).

[82] Z. Lin, I. Volvach, X. Wang, and V. Lomakin, *Eigenvalue-Based Micromagnetic Analysis of Switching in Spin-Torque-Driven Structures*, Phys. Rev. Appl. **17**, 34016 (2022).

[83] J. Fischbacher, A. Kovacs, H. Oezelt, T. Schrefl, L. Exl, J. Fidler, D. Suess, N. Sakuma, M. Yano, A. Kato, T. Shoji, and A. Manabe, *Nonlinear Conjugate Gradient Methods in Micromagnetics*, AIP Adv. **7**, 1 (2017).

[84] M. D'Aquino, C. Serpico, G. Bertotti, T. Schrefl, and I. D. Mayergoyz, *Spectral Micromagnetic Analysis of Switching Processes*, J. Appl. Phys. **105**, 07D540 (2009).

[85] S. Perna, F. Bruckner, C. Serpico, D. Suess, and M. d'Aquino, *Computational Micromagnetics Based on Normal Modes: Bridging the Gap between Macrospin and Full Spatial Discretization*, J. Magn. Magn. Mater. **546**, 168683 (2022).

[86] Y. Saad, *Iterative Methods for Sparse Linear Systems* (SIAM, 2003).

[87] S. Fu, R. Chang, I. Volvach, M. Kuteifan, M. Menarini, and V. Lomakin, *Block Inverse Preconditioner for Implicit Time Integration in Finite Element Micromagnetic Solvers*, IEEE Trans. Magn. **55**, 1 (2019).

[88] R. J. Gilmore and M. B. Steer, *Nonlinear Circuit Analysis Using the Method of Harmonic Balance—A Review of the Art. Part I. Introductory Concepts*, *International Journal of Microwave and Millimeter-Wave Computer-Aided Engineering*, **1**, 22 (1991).